Bjørn Wilhelm Jæger

Numerical Study on Offshore Wind Turbine Blade Installation by Utilizing a Floating Vessel

Master's thesis in Marine Tecknology
Supervisor: Zhen Gao
Co-supervisor: Amrit Shankar Verma

June 2021

Master's thesis

NTNU
Kunnskap for en bedre verden

Bjørn Wilhelm Jæger

Numerical Study on Offshore Wind Turbine Blade Installation by Utilizing a Floating Vessel

NTNU
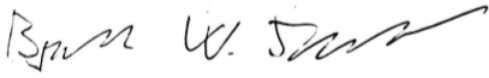Norwegian University of
Science and Technology

Preface

This thesis concludes the Master of Science degree in Marine Technology with a specialization within Marine Structures at the Norwegian University of Science and Technology (NTNU). The study was conducted in the spring of 2021 and continues the Project Thesis work from fall 2021.

The topic of the thesis is blade installation by utilization of a floating vessel. It was chosen based on the author's interest in TMR4215 Sea Loads and TMR4182 Marine Dynamics, along with the opportunity to study the fast-maturing technology of offshore wind turbines.

This thesis assumes that the reader has a basic understanding of engineering, and marine technology.

Bjørn Wilhelm Jæger 10.06.2021

Acknowledgments

I would like to express my gratitude to my project supervisor Professor Zhen Gao for helpful guidance during the fall and spring. Our meetings every second week have given me a good insight into the field of offshore wind turbine blade installation. I also appreciate the time spent going through my paper and providing me with detailed feedback.

I would also like to extend my kindest regards to my co-supervisor, Dr. Amrit Verma, to improve my understanding of blade installations and provide me with detailed recommendations.

I would also like to thank Dr. Yuna Zhao for providing the numerical model and helping me with issues regarding the model.

At last, I would like to show appreciation towards my fellow students, which have encouraged and enlightened my days at Tyholt. Especially thanks to my office mates for providing me with a great working environment where we were able to balance joy and studies.

Abstract

As offshore wind turbine installations move towards deeper water, it becomes more challenging for the conventional jack-up vessel to perform the installations. Floating vessels can perform operations regardless of depth but are more sensitive to wave-induced motions. Wind turbine blade installation is highly sensitive to dynamic motion responses, and low motions of the installation system are accepted. Therefore, floating vessels have not been utilized for this type of operation yet. However, in recent years, numerical models have been introduced to study the feasibility of using floating vessels for installation.

The motions of the installation system were further investigated by global response analysis, where several time-domain simulations were performed for different environmental conditions. The study utilized a fully coupled SIMO-RIFLEX-Aero code developed by Yuna Zhao of a monohull vessel with its corresponding crane, blade, and lifting assembly. The installation system remained stationary throughout the investigation, with the blade at its final position before mating with the hub. This thesis emphasizes the study of blade motion. When there is both wind- and wave-induced motions, it is essential to identify the behavior of the blade. The natural periods and critical responses of the blade and other components of the numerical model were determined using spectral analysis. Blade pendulum roll- and yaw resonance were found to dictate the responses of the blade.

This study employed the response-based criteria introduced by Amrit Verma to assess the limiting motions of the installation in stochastic winds and waves. He defined the criteria as in-line and transverse blade root velocities relative to the hub. The maximum velocities of 20 simulations were fitted to an extreme value distribution to derive the velocities corresponding to a 10^{-4} safety level. The probabilistic model of the blade velocities was tested and monitored, and determined to be adequate. Furthermore, the operational limits were formed for head and bow sea. Head sea was concluded to be the most favorable heading; however, even for this heading, it was a restrictive amount of environmental conditions satisfying the response-based criteria. The operational limits were compared to 10 years of historical Metocean data for the summer months, and only 14.4% of the environmental conditions were acceptable. Therefore, the approach was not found to be economically feasible.

Sammendrag

Når vindturbininstallasjoner til havs beveger seg mot dypere vann, blir det mer utfordrende for det konvensjonelle oppjekkningsfartøyet å utføre installasjonene. Flytende fartøy kan utføre operasjoner uavhengig av dybde, men er mer følsomme for bølgeinduserte bevegelser. Installasjon av vindturbinblad er svært følsom for dynamiske bevegelsesresponser, hvor lave bevegelser fra installasjonssystemet kan aksepteres. Derfor har ikke flytende fartøy blitt benyttet for denne typen operasjoner enda. De siste årene har numeriske modeller blitt introdusert for å undersøke muligheten for å bruke flytende fartøy til installasjonen.

Bevegelsene til installasjonssystemet ble videre undersøkt av global responsanalyse, der det ble utført flere simuleringer i tidsdomenet for forskjellige værforhold. Studien benyttet en fullkoblet SIMO-RIFLEX-Aero-kode utviklet av Yuna Zhao av et monohullfartøy med tilhørende kran, blad og løfteinnretning. Installasjonssystemet er antatt stasjonær under hele studiet, med bladet posisjonert i sin endelige posisjon like før det guides inn i navet. Denne oppgaven legger vekt på bevegelse av turbinbladet. Når det er både vind- og bølgeinduserte bevegelser, er det viktig å identifisere bladets bevegelsesmønster. De naturlige periodene og kritiske responsene til bladet og andre komponenter i den numeriske modellen ble bestemt ved hjelp av spektralanalyse. Bladpendelrull- og resonans i jag viste seg å dominere bladresponsen.

Denne studien benyttet responsbaserte kriterier introdusert av Amrit Verma for å vurdere de begrensende bevegelsene til installasjonen i stokastisk vind og bølger. Han definerte kriteriene som radiale og og tverrgående bladrothastigheter i forhold til navet. De maksimale hastighetene fra 20 simuleringer ble tilpasset til en ekstrem verdifordeling for å utlede hastighetene som tilsvarer et 10^{-4} sikkerhetsnivå. Sannsynlighetsmodellen av bladhastighetene ble testet og overvåket og bestemt til å være tilstrekkelig. Videre ble operasjonelle grenser dannet for møtene- og baugsjø. Møtene sjø ble konkludert med å være den mest gunstige kursen; selv for denne kursen var det imidlertid en begrensende mengde værforhold som tilfredsstilte de responsbaserte kriteriene. Driftsgrensene ble sammenlignet med 10 års historisk Metocean-data for sommermånedene, og bare 14,4 % av værforholdene var akseptable. Derfor ble tilnærmingen ikke funnet til å være økonomisk gjennomførbar.

Contents

List of Figures

List of Tables

List of Abbreviations

CDF Cumulative Distribution Function

COG Center of Gravity

DFT Discrete Fourier Transform

DLL Dynamic Link Library

DNV Det Norske Veritas

DOF Degree of Freedom

DP Dynamic Positioning

DTU technical University of Denmark

EC Environmental Case

FFT Fast Fourier Transform

FOW Floating Offshore Wind

HAWC2 Horizontal Axis Wind turbine simulation Code 2nd generation

IEA International Energy Association

JONSWAP Joint North Sea Wave Project

NREL Nationale Renewable Energy Association

OWT Offshore Wind Turbine

RAO Response Amplitude Operator

SDS Sustainable Development Scenario

STEPS Stated Policies Scenarios

TI Turbulence Intensity

Chapter 1

Introduction

1.1 Background

The Covid-19 pandemic has significantly lowered the global energy demand in the previous year. However, the energy demand expects growth in the coming decade [1]. At the same time, the world demands to use less non-renewable energy sources to reduce the environmental footprint. As a result, the use of renewable energy sources is predicted to rise.
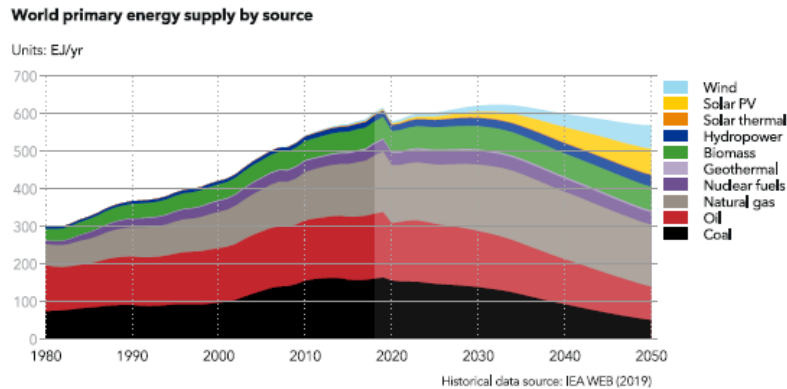
Figure 1.1: *World primary energy supply by source [2]*

DNV has provided an annual outlook for the energy transition. The historical data comes from IEA, and the projection is based on a model that simulates the interaction of energy consumers over time [2]. Covid-19 has influenced this report. DNV projected the worldwide energy demand to fall by 8% in 2020. In addition, Covid-19 impacts the forecasts for long-term effects, with total energy demand fluctuating 6-8% lower through until 2050. However, even without Covid-19, the total energy demand was set to peak in 2032. There are various reasons for the stagnation in energy consumption, but the bottom line is that energy will be used more efficiently in the future thanks to increasingly advanced and intelligent technologies.

1

World electricity generation by power station type

Units: PWh/yr
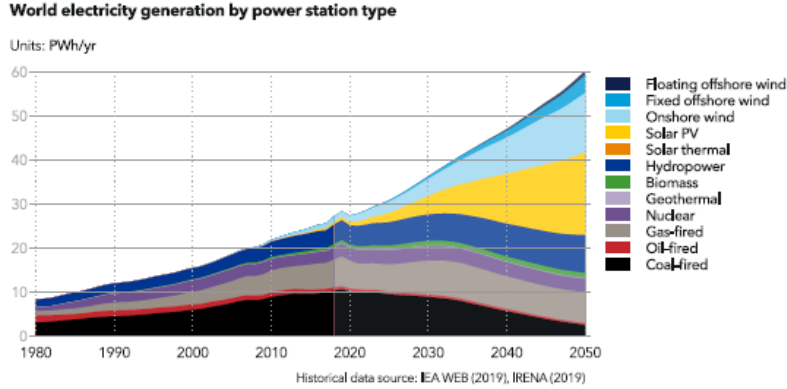
Figure 1.2: *World electricity generation by power station type [2]*

Figure 1.2 shows that wind energy will grow dramatically until 2050, although total energy demand will drop. Given DNV's best estimates, the total capacity of bottom-fixed offshore wind will be about 1 TW in total, and 260 GW for floating wind in 2050 [2]. This estimate is highly sensitive to individual assumptions on wind, and solar photovoltaic (PV) cost learning rates as wind and solar power will compete against each other [2]. Given that the total capacity at the end of 2019 was 22,072 MW, increasing with 3,627 MW [3], a rough estimate of the total capacity at this instance is 28,000 MW. Hence, another 1,232 GW is estimated to be installed within 2050. Consequently, an average of 41.1 GW has to be installed every year, which is 11.3 times higher than the installations performed in 2019. In terms of 8 GW offshore wind turbines (OWTs), this timeframe expects to see the installation of 154,250 OWTs. This estimate ignores the fact that an OWT has a 20-year lifespan, implying that all OWTs installed before 2030 must be replaced. Furthermore, maintenance and blade replacement is not included in these numbers. Therefore, the amount of work on the OWTs is likely to be substantially higher than the projected installation of 154,250 OWTs.

1.2 Market

The global renewable energy market has developed significantly for many years. The market is projected to further thrive as the use of fossil fuel become less popular due to lack of resources and the increased environmental awareness. Investments in energy sectors have been reported and further predicted by IEA [4]. From 2019 to 2020, the investments have decreased for renewable energy and fossil fuels, which the ongoing pandemic can explain. These results have been compared to two of IEA's future scenarios; STEPS, which is according to stated policies, and SDS, which is according to what IEA believes is sustainable development, fully aligned with the Paris Agreement. In both scenarios, investments in fossil fuels will decrease while renewable energy investments will increase significantly.

Along with investments in renewable energy sources rising, the investments for off-shore wind turbines are increasing. One would think that Covid-19 would disturb the growth of offshore wind turbines. On the contrary, the total investments in the first half of 2020 exceeded the total amount of investments in OWTs for the entire 2019 [5].

Currently, bottom fixed wind turbines are dominating the market which is indicated in figure 1.5 in section 1.3.3. The development of floating offshore wind (FOW) is still in its early stages, but it is a fast-maturing technology. The industry made a big step forward in 2017 when Equinor commissioned the world's first multiline grid of FOW. Equinor's initiative has inspired more companies. As of 2018, there are 50+ floating offshore wind projects at different stages of development, where three-quarters of them are in Europe [6]. The fast-maturing technology of FOW challenges bottom-fixed OWTs when approaching deeper waters; therefore, the technology around bottom-fixed OWTs has to develop further to maintain being the favorable option.
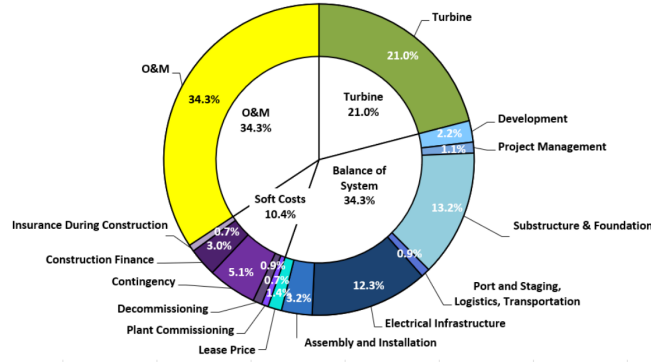
Figure 1.3: *Component-level levelized cost of energy contribution for the 2019 fixed-bottom offshore wind reference project [7]*

The installation phase is an essential part of the scope of a wind farm project. First of all, it is essential to make sure the operation process safely with no harm or damage to personnel nor equipment. If the blade gets damaged and needs replacement, it might result in high manufacturing costs and additional installation time. The day rates of most installation vessels utilized for OWT installation are several hundreds of thousands of US dollars. As a result, by reducing the installation time, the expenses can be significantly decreased. Consequently, the firms urge to minimize the vessel time, which can be achieved by implementing more effective installation methods. Then, the overall costs of the wind farm project can be reduced. According to a reference study by NREL, the installation and assembly phase embody 5 percent off the overall cost of the project [7]. Considering wind farms with prices in the range of billions of dollars, companies would gain great profit by bringing down the installation duration.

1.3 Offshore Wind Turbine Development

1.3.1 Water Depth
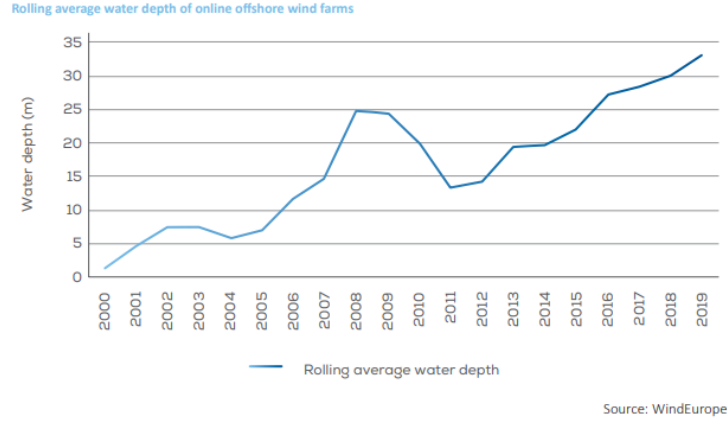
Figure 1.4: *Average depth of OWTs [3]*

A result of the increasing amount of OWTs, is that the available space for new wind fields decreases. Therefore, companies start looking towards deeper water further away from shore. The average depth of offshore wind turbines has risen in recent years and is expected to continue to rise in the future. Conventionally, jack-up vessels are utilized for the installation task. However, the performance of these installation vessels degrades as they travel towards deeper waters. Because their legs are not long enough for deep water, certain jack-up vessels will not be able to perform the installation. In addition, the jack-up time increases for deeper waters, which is one of the most delicate aspects of the procedure. When the water depth exceeds 60-70 meters, jack-up vessels will be unable to fix their legs to the ground, necessitating the use of a floating vessel.

1.3.2 Top-Side

The top side of the OWT consists of a transition piece, tower, nacelle, hub, and blades. These are usually installed in a single operation, with the tower being placed on top of the foundation. Then, the nacelle with hub is installed on top of the tower. At last, the blades are guided in the hub in three pieces. It is essential to know the weight and dimensions of the installed modules to ensure a safe operation. The dimensions of three reference wind turbines are listed in table 1.1. NREL defined the 5MW turbine, DTU characterized the 10MW turbine, and the last one is defined by IEA [8][9][10].

Table 1.1: *Reference OWT dimensions [8][9][10]*

Rating [MW]	5	10	15
Rotor Diameter [m]	126	178.3	240
Hub Diameter [m]	3	5.6	7.94
Hub Height [m]	90	119	150
Rotor Mass [t]	110	227.9	371.6
Nacelle Mass [t]	240	446.0	645.4
Tower Mass [t]	347.5	628.4	860

The rapidly increasing wind turbine sizes provide many challenges that must be addressed. The increasing dimensions require more available deck space, which also often result in the vessel being able to carry fewer OWTs simultaneously. Also, the dimensions are problematic considering the crane height. The blades are installed at the top of the tower, and the crane tip must be able to be moved to this height. Therefore, OWT installation requires taller cranes for increasing turbine size. Also, for increasing lift height, the blade gets more sensitive to vessel roll and pitch motion when located high above the sea surface. The cranes must also have enough capacity to carry heavy nacelles and towers. The increasing masses increase the impact energy of the lifted objects. In case of impact with any surrounding objects, the severity of the impact rises for increasing mass.

1.3.3   Foundation
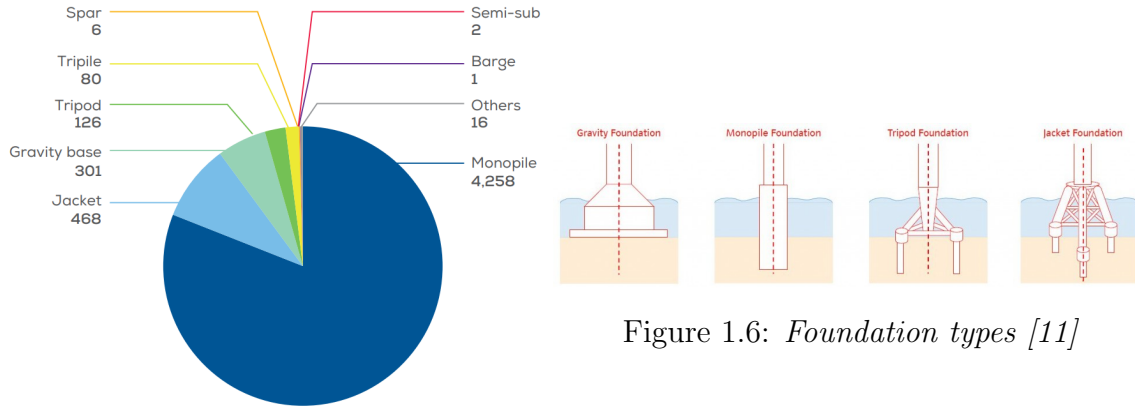
Figure 1.6: *Foundation types [11]*

Figure 1.5: *Foundation distribution [3]*

The most popular choice of foundation is by far monopile, where about 70% of the foundations installed in 2019 were monopiles due to its low installation cost [3]. However, the percentage of monopile foundations reported in 2018 was 81%, which indicates that other foundations are becoming more competitive in comparison to the monopile structure[3]. Figure 1.5 exhibits the distribution of different types of foundations in 2019.

1.4 Installation Vessels

The conventional vessels used for OWT installation are jack-up vessels. Most of these vessels have 4 to 6 jack-up legs, which they hammer into the ground. Their fixed legs give small wave-induced motions, which is essential for OWT installation. Along with the increasing demand and size of OWTs, the vessels have improved in many areas. New vessels have been tailored for OWT installation, and newer concepts out-competes older vessels. Pacific Osprey is a vessel delivered in 2012 and has been actively installing OWT components during its lifetime. However, due to the increase in wind turbine size, it has not been able to deliver next-generation OWTs. Consequently, it installed a new crane boom which allows for the installation of OWTs up to 12MW. Below is a list of its updated technical specifications.

Table 1.2: *Technical specifications of Pacific Osprey [12]*

Delivery Year	2012
Main Deck Area [m^2]	4300
Max Water Depth [m]	70
Max Speed [kn]	13
Main Hoist SWL in Tandem [t]	1425
Main Hook Height Above Deck[m]	132

Figure 1.7: *Pacific Osprey [13]*

Figure 1.8: *Ulstein J103 concept [14]*

Pacific Osprey's need for a bigger crane after only eight years in operation indicates the significant increase in wind turbine size. New concept designs have to take the rapidly increasing OWT sizes into account when being developed. For example, Ulstein J103 is a new concept that should be able to install seven 17 MW wind

turbines per journey. Even though OWTs of this size is yet to be fabricated, the shipyards scale up their designs to be ready for the next-generation wind turbines.

Table 1.3: *Technical specifications of Ulstein j103 concept [14]*

Delivery Year	N/A
Main Deck Area [m^2]	9000
Max Water Depth [m]	65
Max Speed [kn]	11
Main Crane Capacity [t]	2500
Main Hook Height Above Deck[m]	160

(a) *[15]*   (b) *[16]*

Figure 1.9: *Aegir*

Compared to a floating vessel, jack-up vessels are more stable during the lifting phases and allows for rougher weather conditions. The blade installation does not allow large motions of the blade; therefore, it has not been found feasible for large-scale projects to use a floating vessel for this purpose. However, for deep waters, the industry has to look for other solutions than jack-up vessels. Hence, new concepts involving floating installation vessels have to be considered. Moreover, research is done on existing vessels to see if it is feasible to use floating vessels for different environmental conditions. Heerema's monohull vessel Aegir has already been used for offshore wind turbine installation where the turbine was assembled onshore and transported and fitted onto the monopile by Aegir [16]. The vessel has also been frequently used for foundation and offshore substation installation and is familiarized within the OWT industry.

Aegir was originally designed as a deepwater construction vessel, but it was transformed into an offshore heavy lift vessel in 2020, making it more suitable for OWT installation. The vessel includes a J-lay pipe laying tower which may be decommissioned to increase the available deck space. Therefore, it is uncertain how much

available deck space it can utilize for OWTs. A limiting parameter for the vessel is
the crane height which is only 96 meters. Looking at the reference turbines in section
1.3.2, Aegir is only able to install the 5 MW reference turbine.

Table 1.4: *Technical specifications for Aegir [15][17]*

Delivery Year	2013
Length [m]	211.4
Max Speed [kn]	12
Main Crane Lift Capacity [t]	4000
Main Hook Height Above Deck [m]	96

Figure 1.10: *Balder [18]*

Monohull vessels are hydrodynamic efficient and can transit at high speed. Never-
theless, they are not always the preferable option when considering heavy lifts due
to significant rigid body motions. On the other hand, semi-submersibles are known
to be more stable and allow for installations in rougher weather conditions. In ad-
dition, they utilize ballast water to increase their drafts to improve stability during
lifts. Another vessel operated by Heerema, which is acquainted within OWT instal-
lation, is Balder. It is capable of lifting 4500t in tandem lift and 3000t if using the
larger crane at 116 meters height and has a large deck area.

Table 1.5: *Technical specifications of Balder [18]*

Delivery Year	1978
Max Transit Speed [kn]	6.5
3000 Main Crane Lift Capacity [t]	3000
3000 Main Crane Lift Height [m]	116

Jack-up- and floating vessels both have their up-and-downsides when considering
installation. The decreased wave frequency motions due to fixed legs for jack-up
vessels are why these vessels are preferred. They allow relatively rough weather con-
ditions when performing the installation, reducing the potential risk of waiting on the

weather during a task. On the other hand, the jack-up phase introduces some complications. First of all, each vessel has a depth limitation. Secondly, they are dependent on stable soil conditions, and analysis of the soil has to be performed for each installation. Furthermore, the jacking-up phase of the operation is weather-limited and time-demanding. Much time can be saved during a project if jacking-up is avoided for each OWT installation. Floating vessels are not reliant on this phase and use either dynamic positioning (DP) or DP-assisted mooring lines for stationkeeping. These stationkeeping methods require less initiation time and are less complex than the jacking-up phase. However, the floating vessels have lower operational limits and are more exposed to different environmental conditions. Therefore, they are expected to spend more time waiting on the weather. Suppose the floating vessel blade installation approach is found feasible. In that case, the choice of installation vessel will depend on time consumption, and floating vessels may perform installations where jack-up vessels have typically been utilized. Regardless, given certain soil conditions or depths, floating vessels are the only possible option.

1.5   Review of Recent Numerical Studies

There has been a hand full of relevant studies towards offshore blade installation in recent years. Many of these have been cited in this paper to build on their work, and utilize their models and results.

Yuna Zhao has established a fully coupled method, SIMO-RIFLEX-AERO, for numerical modeling and analysis of offshore single blade installation by either jack-up or floating crane vessels [19]. The coupled method account for blade aerodynamics, structural dynamics, vessel hydrodynamics, and wire coupling mechanics. The jack-up crane vessel was modeled in detail. In contrast, a preliminary feasibility study of the floating crane vessels, a monohull vessel and a semi-submersible vessel, was conducted and compared with the performance of the jack-up crane vessel. The result indicated that both vessel types are feasible, but the semi-submersible is more feasible than the monohull vessel. Furthermore, Zhao derived the operational limits of wind and wave conditions by applying the response-based criteria. The fully coupled model for the monohull vessel is utilized in the study of this paper. The fully coupled model for the monohull vessel is utilized in the study of this paper.

Emphasization of response-based operational limits has been recurring in much of the recent work on OWT installation. Guachamin Acero has formed a generic and systematic approach that allows for the identification of critical events, limiting parameters, and assessment of response-based operational limits of marine operations [20]. The study involved the monopile hammering process, transition piece mating, and tower and rotor nacelle assembly performed by a heavy floating vessel.

The thesis for the degree of Philosophiae Doctor of Amrit Verma is concerned with impact loads and damages to the blade during installation [21]. Verma developed

numerical models for damage assessment where the emphasis was on efficient FE models. The response-based criteria were formed from the damage assessment, which has been applied in this study. Furthermore, probabilistic methods were utilized to estimate the operational limits for impact under normal and accidental loads for installation by a jack-up vessel.

1.6   Aim and Scope

- Jack-up vessels are the conventional vessel for the installation, but floating vessels would allow installation when moving into deeper waters. This study will utilize a numerical model of a monohull vessel, crane, and blade, which was provided by Zhao, to study blade installation [19].

- The thesis goes under the category marine operations, which means the rules and regulations within this field must be understood. DNV- standards, -regulations, and -recommendations are typically followed for operations in the North Sea. These form the basis for the choice of the safety level of the operation, which is set to 10^{-4}.

- This thesis emphasizes the study of blade motion. When there is both wind- and wave-induced motions, it is essential to identify the behavior of the blade. The blade is affected by the motions of the vessel, crane, tugger lines, and external forces, and it is vital to understand which components in the system are critical to the motions of the blade. The results from this part will support the development of mitigations that can be used for further work.

- Several time domain simulations are performed for each sea-state to develop a probabilistic distribution of the blade motions. From this, a satisfactory safety level can be obtained considering stochastic wind- and wave conditions and deterministic blade installation. The fitted probabilistic model of the blade motions is tested and monitored to study the uncertainties of the model.

- The relationship between blade velocity during installation and induced damage due to contact between blade root and hub was derived by Verma to form the response-based criteria [21]. In this thesis the focus was to obtain the blade root velocities and then use the response-based criteria to identify the limiting blade velocities, and obtain the limiting sea-states. In addition, historical Metocean data is sampled and compared to the operational limits to discuss the approach's feasibility.

1.7 Limitations and Assumptions

The limitations and assumptions of this thesis is presented in the following list:

- *The transient effects of the installation*
  The study assumes the process to be stationary, but in real life transient effects, such as lifting and moving around the blade, are present. However, these operations are carefully performed, and the rate of change in the blade, crane, and lift wire is very low. Therefore, the transient effects are minimal during the operation. Then it is important and practically possible to consider the blade steady-state dynamic responses at different locations during installation. However, this thesis only considers one representative blade position during installation.

- *Human errors during the operation*
  Human errors are difficult to avoid when performing many procedures repeatedly. This study assumes that the crane operator is able to hold the blade in a perfect position, and the only motions to the blade are those that are caused by environmental factors.

- *Structural motions of the blade*
  This thesis neglects the flexibility of the blade. The blade structural responses will be minimal during the blade installation when the blade rigid-body motions dominate; therefore, it should be safe to disregard these motions.

- *Structural motion of the monopile*
  The structural motion of the monopile is neglected. In general, the hub will displace, but this response is significantly smaller than the motions of the blade. However, for a more comprehensive study, this motion should be included.

- *Statistical uncertainty of the motions*
  There will always be some uncertainty to probabilistic models. This study contemplates the tail region, where there is a reduced amount of data, making the model sensitive to rare statistical events. The uncertainties can be reduced by running more simulations for each load case, but this will increase computational efforts.

- *Disregarding vertical motion for response-based criteria*
  Since the guide-pins are located at each side of the blade-root opening, the impact will most likely happen transversely. The vertical velocity will have some influence on the impact energy. However, most of the energy from this motion will not result in impact energy; hence, this effect is neglected for simplicity. Anyhow, Verma argued that the guide pin impact scenario is conservative due to it does not account for the impact energy of the bolts being dissipated [21].

Chapter 2

Installation Methodology, Critical Events, Velocity Criteria

2.1 Marine Operations

Traditionally, marine operations have been planned and executed based on experience and good seamanship. However, the maritime industry has increased the awareness of the safety of operations, which has resulted in stricter rules and regulations. Also, new operations where there is a lack of experience and statistical data have been introduced. DNV has provided different standards to ensure the operations to be safe. One of the planning principles of the operation is to design the operation to bring an object from one defined safe condition to another [22]. A safe condition is defined as a condition where the object is exposed to normal risk (i.e., similar risk as expected during in-place condition) for damage or loss [22]. The marine operation is either defined as weather unrestricted or weather restricted. Operations where the planned operation period is longer than 72 hours, are defined as weather unrestricted. These operations have to design the operation according to long-term statistical data of the operation site. Operations of a shorter period can be defined as weather-restricted, which means the operation can be planned and executed within the period of a reliable weather forecast. Consequently, the operation, in general, can be defined with lower design loads. The installation of an offshore wind turbine may take longer than 72 hours from start to end. However, the installation is usually divided into separate operations where the blade installation is considered as one operation. Therefore, the planning of blade installation can oblige to the regulations set by the weather-restricted criterion.
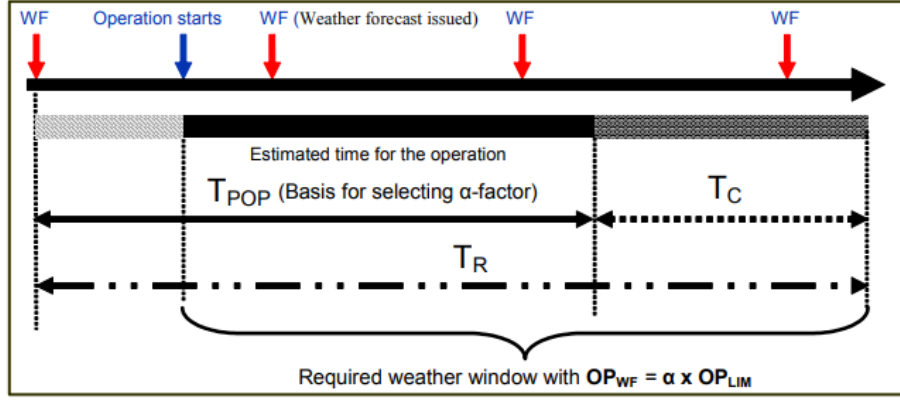
Figure 2.1: *Marine operation periods [22]*

Winds or waves usually define the operational limits. To ensure that the weather doesn't exceed the limits during the operation, a weather window has to be established. In many cases, the operation is divided into several sub-operations where a weather window is established for each sub-operation. A sub-operation has to be defined such that the object is able to return to a safe condition within the duration of the weather window. The sub-operations of blade installation are presented later in this section. The weather window is referred to as the reference period (T_r). This period consists of the planned operational time (T_{POP}) plus contingency time (T_c). The contingency plans shall consider redundancy, backup equipment, supporting personnel, emergency procedures, and other relevant preventive measures and actions [22].

After the reference period has been established, the $\alpha - factor$ has to be defined. This factor is introduced to account for uncertainties in the weather forecast. It is decided based on tables where design wave/wind and T_{POP} are given. Then, the operational criteria are calculated from:

$$OP_{WF} = \alpha \cdot OP_{lim} \tag{2.1}$$

where OP_{lim} is the operational limit based on the design load. According to DNV-OS-H101 the probability of occurrence of an accidental event should be no more than 10^{-4} [22]. Load-, safety and material factors are included to ensure that this probability is not exceeded; however, operational error may lead to higher probability of occurrence, which should be assessed by the as low as reasonable possible principle (ALARP). The design wave is established based on these principles

2.2 Blade Installation

This section will go through the conventional methodology developed by the industry of blade installation.
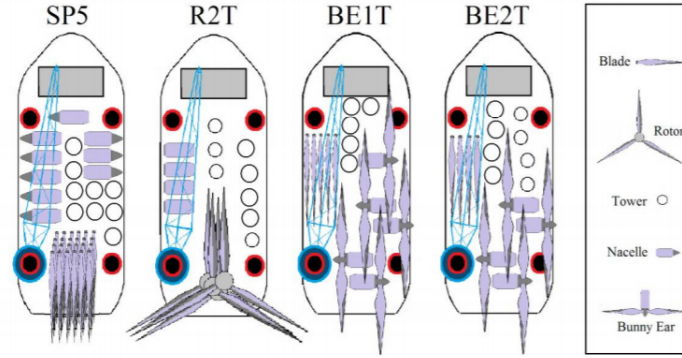
Figure 2.2: *Assembly configurations of the OWT's topside. From left: Five Pieces Separately, Pre-assembled Rotor, and "Bunny Ear" with tower in one and two pieces respectively [23]*

Figure 2.2 illustrate different proposed deck layouts. The installation in this thesis is based on the operation where the blades are installed separately and stacked upon each other on deck, which can be seen all the way to the left in the figure above. Hence, the procedure has to be repeated to install all of the three blades. Each blade installation consists of three sub-operations. *Sub-operation 1* consists of placing the crane tip in position and attaching the yoke to the blade. *Sub-operation 2* is the lift-off phase and aligning the blade to the hub. *Sub-operation 3* is the mating phase where the blade is connected to the hub.

A more detailed procedure for the installation of the blades is listed below and figures from real-time operations can be seen in figure 2.3. *Sup-operation 1* consists of items 1-5. *Sub-operation 2* considers step 5 and 6. The last sub-operation consists of step 7-9.

1. Asses the weather window and if operational criteria is fulfilled

2. Rotate the hub to horizontal position

3. Fasten the yoke to the crane hook and move it towards the blade

4. Fasten the yoke to the blade

5. Attach tugger lines

6. Lift the blade to the hub height

7. Align the blade with the hub

8. Asses if the operational criteria is fulfilled for safe mating of blade

9. If yes, mate the blade with the hub. If no, move the blade back in position on deck.

10. Replace the guide pins with bolts and pretension the bolts

11. Detach the yoke and move onto next blade

(a) *Lift-off from vessel deck*

(b) *Lift blade to hub-height*

(c) *Blade root approach the hub*
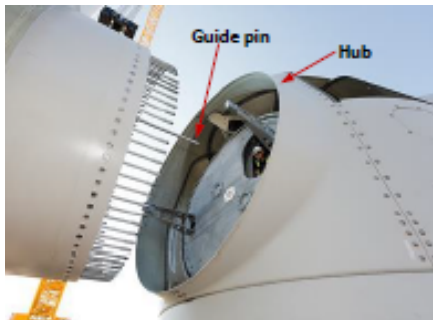
(d) *Monitoring blade-root motion*

(e) *Mating phase off blade-root and hub*

Figure 2.3: *Single blade installation [19]*

2.3   Installation System

The installation system consists of a vessel, crane, blade along with its lifting arrangement.

2.3.1   Vessel and Crane

The vessel utilized in this study is a 6 DOF floating monohull vessel. One can see its main properties in table 2.2. The vessel is assumed to utilize a DP system for stationkeeping, simplified as a linear spring system. The location of the crane is on the starboard side of the vessel. It is a pedestal crane, and the configuration is assumed to be stationary throughout the operation. It's main parameters are tabulated in table 4.1.

Table 2.1: *Main parameters of crane [19]*

Crane properties	
Booom length [m]	107.6
Crane boom angle [deg]	67.6
No. of eq. boom wires [-]	2
Eq. boom wire stiffness [kN/m]	9048
Eq. boom wire damping [kNs/m]	90.5
Crane tip height [m]	144.9
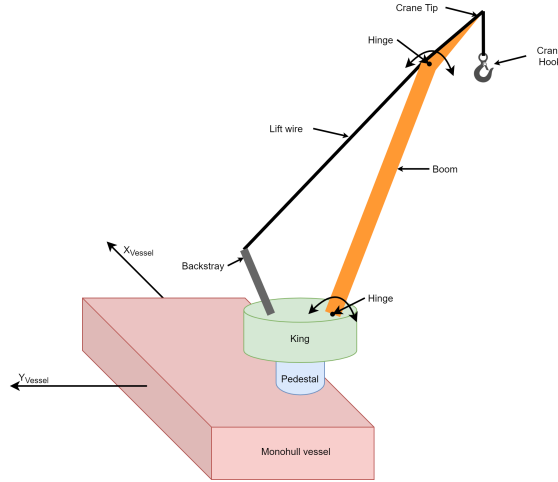
Figure 2.4: *Vessel and crane*

Table 2.2: *Main parameters of vessel [19]*

Vessel properties	
Length [m]	183
Breadth [m]	47
Operational draught [m]	12
Displacement [m^3]	61 900

2.3.2   Blade and Lifting Arrangement

The blade in this study is based on the DTU 10 MW wind turbine. The blade weighs about 42 tons and is 86.37 m long. A yoke weighing about 47 tons is connected to the blade during the installation. 4 lifting wires are connected to lift the assembly. To reduce the motions of the blade, two tugger lines are connected from the crane to the blade. These have a moment arm of 10 meters each and are pre-tensioned to 80 kN.
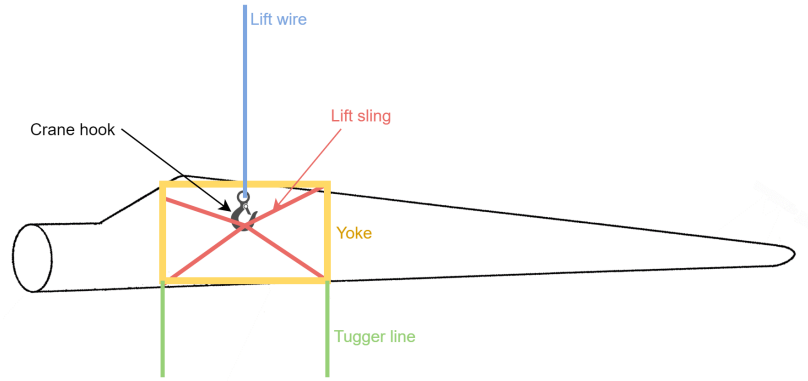
Figure 2.5: *Blade lifting arrangement*

2.4 Critical Events

The rest of this section is mostly based on the thesis for the degree of Philosophiae Doctor of Amrit Shankar Verma: *Modelling, Analysis and Response-based Operability Assessment of Offshore Wind Turbine Blade Installation with Emphasis on Impact damages* [21]. The vessel utilized in the assessment was a jack-up type. It is assumed that the critical scenarios of the installation can be regarded similarly for floating- and jack-up vessels. Furthermore, the impact assessment performed by Verma is used to define the threshold velocities of the blade and define the operability of the installation.
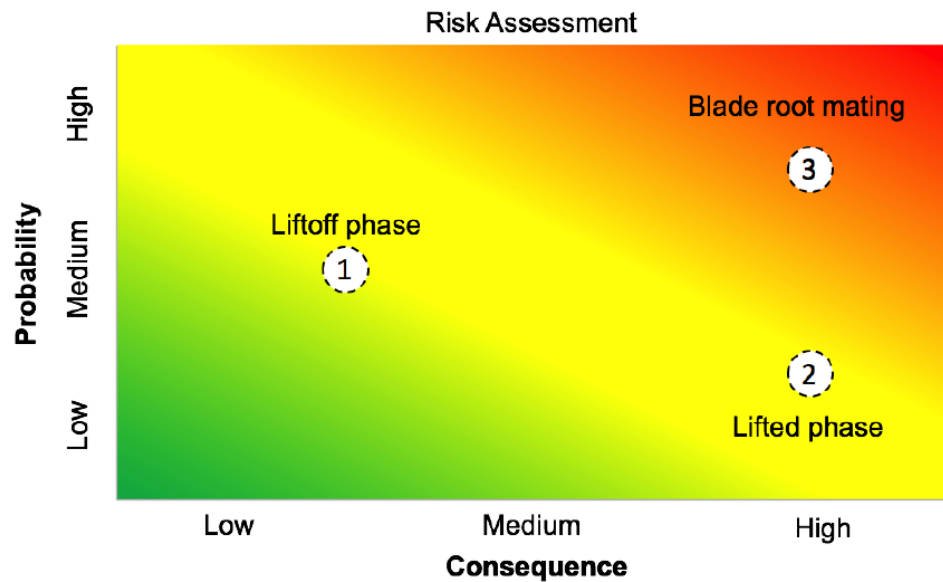
Figure 2.6: *Risk assessment of sub-operations [21]*

Verma performed a qualitative risk assessment to evaluate which sub-operations involved the most risk. This assessment was done for the use of jack-up vessels.

Since this scope considers floating vessels, the increased motions may affect one sub-operation more than another which may lead to different critical sub-operations. The results of the risk assessment are displayed in figure 2.6. *Sub-operation 1* was evaluated to have a medium occurrence rate due to the blades being stacked closely together; although, a low impact scenario due to the wind-induced motions at deck height being considerably low. *Sub-operation 2* has a low occurrence rate, argued by it not being frequently recorded in the industry. This scenario includes much impact energy; however, most of the energy is converted to rigid body translation and rotation. Then, the blade acts as a hazard towards personnel and surrounding structure, and the consequence of the event has to be considered high. *Sub-operation 3* has a high occurrence rate as the sub-operation is sensitive to small motions. The consequence of the event is high due to the result being damage to the blade. The damage can reduce the blade's lifetime, or the blade loses its ability to operate correctly.

Given that *sub-operation 3* is the most probable and consequential event, this sub-operation is regarded as the most critical event. Henceforth, this part of the operation will be investigated thoroughly. *Sub-operation 2* has to be considered as well, since the consequence of the blade hitting the surrounding structure may be significant towards the performance of the blade during operation. In addition, the risk of under-reporting the accident scenario means that the actual probability of occurrence is higher than the estimated one.

2.5   Response-Based Criteria

For the response-based approach, the operational limits are derived for actual parameters that limit the operations [20]. These limiting (response) parameters and their corresponding critical events and activities are identified by numerical simulation of the actual operations, and quantitative assessment of the dynamic responses [20]. The critical events were identified and further assessed by Verma to determine the allowable limits of the system. These limits will set the response-based criteria for this study.

In section 2.4 the lift-off phase and the mating process were determined as the critical events. The consequence of failure for these phases would be substantial damage to the blade. Substantial damage is defined as no damage and permanent absorbed energy obtained in the blade [21]. DNV has introduced a guidance note where accidental impact should lead to visible damage to impact the critical strength of the blade [24]. They also imply that impact damage during fabrication, transport, and installation should not reduce the design resistance strength below the design load [24]. High safety factors for the design have to be included to account for uncertainties in damage and impact loads because there is not a substantial amount of numerical models for the impact scenario [21]. The result is conservative approaches that do not allow for installation during rough weather conditions.

2.5.1   Sub-Operation 2

For *sub-Operation 2* there are many failure modes to consider. However, the scenarios of leading-edge impact with the turbine tower were decided as one of the most critical ones. Verma presented the results for two contact regions which he argued to be of importance. Contact in region A, located 11 m from the blade COG in the y-direction, lead to a fair amount of kinetic energy being transformed to internal energy. On the other hand, most energy in region B, located 34 m from the blade COG in the y-direction, is dissipated as rigid body motion of the blade. However, the structural integrity of this area is more fragile. Hence, a lower amount of energy is needed to damage the region. Verma exhibited that there was no damage in the blade for a contact velocity of 0.08 m/s. This velocity is minimal, and a velocity of this quantity may easily occur when using a monohull vessel that is sensitive to wave-induced motions. Therefore, it would not be feasible to set this value as a response-based criterion. Also, this scenario is an accidental impact scenario which means other regulations apply than for *sub-operation 3* where impact is inevitable. By successful risk management, one can avoid the impact scenario.

2.5.2   Sub-Operation 3
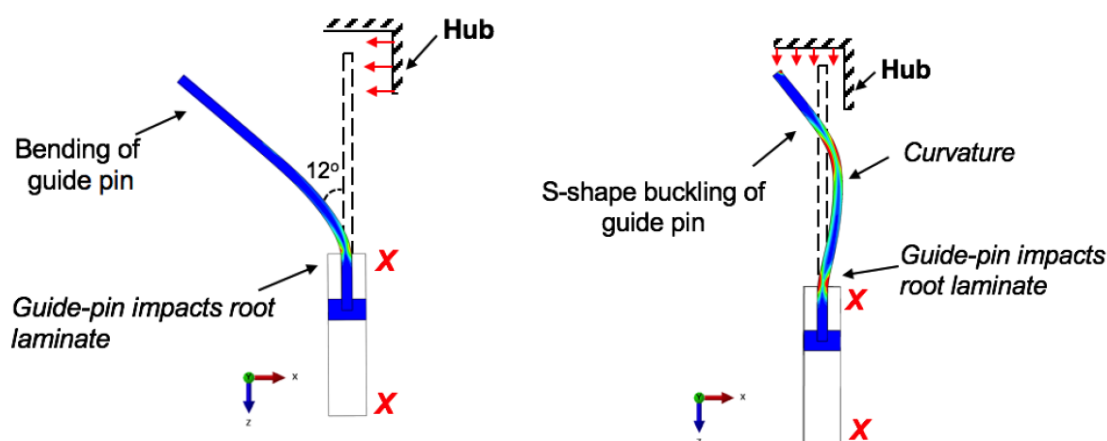
(a) *Bending due to in-line impact with hub*   (b) *Buckling due to transverse impact with hub*

Figure 2.7: *Failure modes of guide pins [21]*

For the mating phase, damage to the guide pins is of concern. The structural damage to the guide pins is not very agonizing since they can easily be replaced, leading to minor operational delays. However, when displaced significantly, they may affect the surrounding laminate structure. Verma has considered two different failure modes; bending of guide pin due to transverse motions (figure 2.7a), and buckling of guide pin due to in-line motions (figure 2.7b) [21]. These two failure modes have critical velocities perpendicular to each other and result in two different critical impact velocities. The maximum allowable velocity can then be analyzed separately as

transverse and in-line velocities. Only the x-component velocity is considered for the transverse impact scenario due to the position of the guide pins being along the x-axis of the blade root, indicated in figure 2.3d. Therefore, the z-component velocity will not result in an impact with the hub. The maximum allowable velocities were assessed to be $V_y^{allow} = 0.76m/s$ for sideways impact and $V_x^{allow} = 1.35m/s$ for head-on impact. The critical positional phase of the blade root mating should take no more than 10 minutes. Therefore, neither of these velocities should be exceeded within this period.

Numerical Model

3.1 General

The numerical model for global motion responses was provided by Yuna Zhao, which is comprised of a fully coupled method SIMO-RIFLEX-Aero simulation. It can account for blade aerodynamics, crane flexibility, detailed modeling of installation vessel motions, and wire coupling mechanics [19]. Both SIMO and RIFLEX codes are developed by SINTEF Ocean and have been an important tool for modeling wind turbine installation methods. SIMO models the blade and vessel as rigid bodies, while RIFLEX models the slender system such as the crane and lines.

3.2 Coupled Method

As mentioned, the numerical simulation consists of a fully coupled SIMO-RIFLEX-Aero method. The flow-chart of the coupled method can be seen in figure 3.1. TurbSim generates the wind field, which is the input to the Aero-code. From this, the aerodynamic loads are calculated and passed into SIMO. A dynamic link library (DLL) is implemented in the code such that Aero and SIMO are united. It allows both the programs to utilize the library simultaneously. Furthermore, SIMO generates the waves and calculates the motion responses. Then, the wave kinematics, along with the hydrodynamic and aerodynamic loads on the rigid bodies, are passed from SIMO to RIFLEX. RIFLEX calculates the structural responses of the system, and the rigid motions are directed back to SIMO. For the next time step, SIMO redirects the motion responses to Aero and RIFLEX, and the process starts over again.
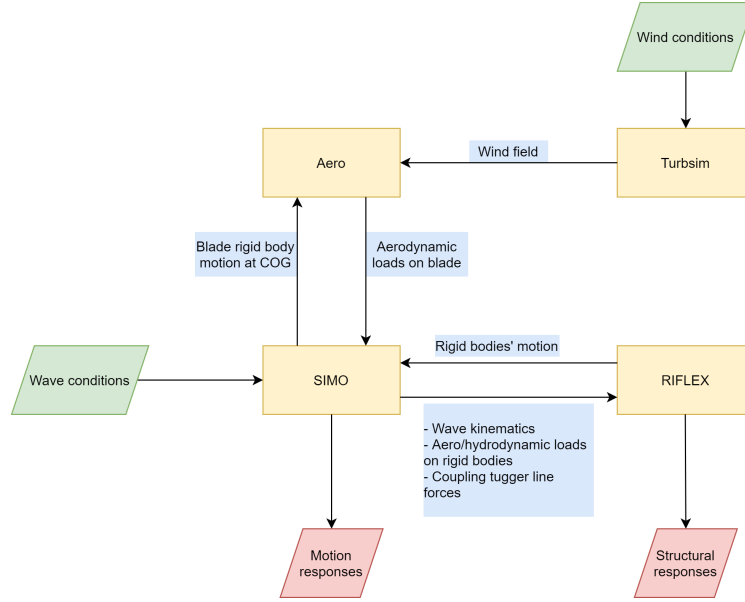
Figure 3.1: *Coupled simulation flowchart (based on figure from Zhao [19])*

3.3   Wind Field

The wind fields are generated using the open-source program TurbSim, which is provided by NREL [25]. The program generates a 3-dimensional field that covers the whole body of the blade. An input mean velocity at hub height is defined, which is used as reference to calculate the wind profiles at other heights. A power-law exponent is defined to account for the variations in wind speed across the vertical direction. The mean velocity at height z is calculated by:

$$\bar{u}(z) = \bar{u}(z_{ref})\left(\frac{z}{z_{ref}}\right)^{PLExp} \tag{3.1}$$
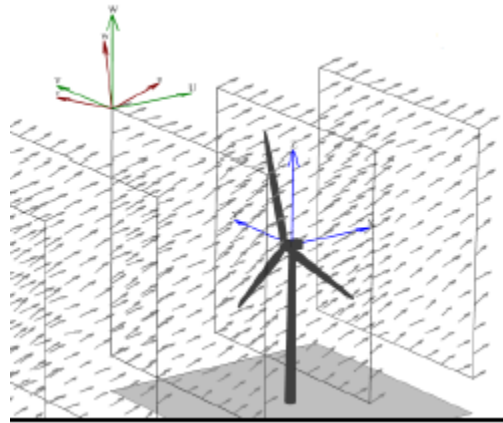
Figure 3.2: *Illustration of wind field in TurbSim*

Different horizontal flow angles are considered in this study, and TurbSim allows the user to rotate the wind from its alignment to the inertial reference frame. Figure 3.2 is an illustration of a wind field generated by TurbSim and its coordinate system. In this thesis, the wind field will only be generated around one blade. The positive x-direction is defined perpendicular to the leading edge of the blade.

Different turbulence models can be chosen which account for steady, turbulent, and gust wind. This study considers the IEC Kaimal spectrum, which comprises turbulent wind. The turbulence intensity (TI) is defined by the IEC categories A, B, and C, where C is the most turbulent. These correspond to expected turbulence intensity of 12%, 14%, and 16% at 15 m/s. Moreover, TurbSim scales the turbulence intensity to the wind velocity specified by the user. Thus, the spectra for each wind component K = u, v, w are given by:

$$S_K(f) = \frac{4\sigma_k^2 L_K / \bar{u}_{hub}}{\left(1 + 6f L_K / \bar{u}_{hub}\right)^{\frac{5}{3}}} \tag{3.2}$$

where f is the cyclic frequency, and L_K is an integral scale parameter. The relationship between the standard deviations are defined as:

$$\sigma_v = 0.8\sigma_w \tag{3.3}$$

$$\sigma_w = 0.5\sigma_u \tag{3.4}$$

The spectra is assumed to be invariant across the grid which means there will be small variation in the u-component standard deviation.

3.4   Aerodynamic Loads on Blade

Zhao developed the Aero-code to calculate the aerodynamic loads acting on the blade. This section is a reproduction of the notes on the aerodynamic loads in [19].

(a) *Local blade element coordinate system [19]*

(b) *Cross flow principle [19]*
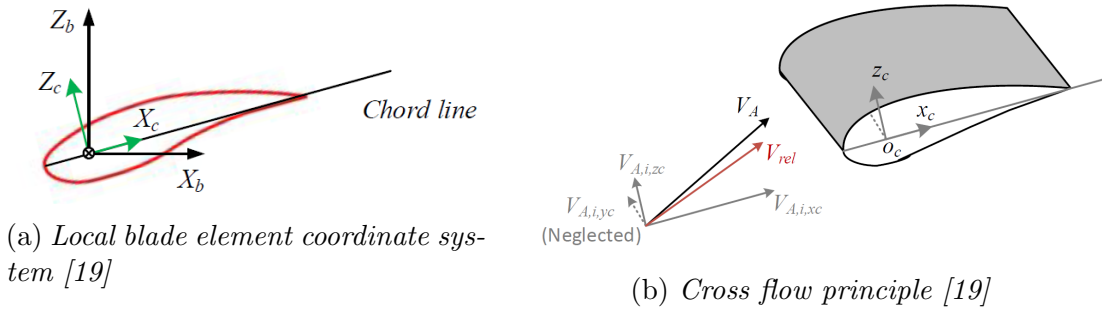
The blade is divided into several elements along the length of the blade. The aerodynamic loads are calculated for each elements in the local element coordinate system

as seen in figure 3.3a. The aerodynamic loads on each elements is calculated based on the cross-flow principle which decompose the fluid velocity to normal and parallel components to the chord line of the blade seen in figure 3.3b. Each element is considered as 2D-elements, which means the velocity component along y_c can be neglected. Then, the velocity vectors can be projected as:

$$\mathbf{V_{A,i}} = [V_{A,i,xc} \; 0 \; V_{A,i,zc}]^T \tag{3.5}$$

where $\mathbf{V_{A,i}}$ is the relative wind velocity for element i. This velocity is calculated in equation 3.6, which is based on the relative velocity between the global wind velocity at element i ($\mathbf{V_{WG,i}}$) and the element local velocity ($\mathbf{V_i}$). During blade operation, a third term, accounting for wake-induced velocity, is included in the calculations. However, this term is neglected as the blade is not designed to rotate during installation; hence; it does not create a significant wake.

$$\mathbf{V_{A,i}} = \mathbf{T_{GC,i}}(\mathbf{V_{WG,i}} - \mathbf{V_i}) \tag{3.6}$$

$\mathbf{T_{GC,i}}$ is the transformation matrix between global coordinates and element coordinates. Furthermore, when the velocities have been established, the angle of attack (α) can be determined. Based on the angle of attack, the lift and drag coefficients are determined from a look-up table defined for each element. The lift and drag forces are calculate based on these and the total aerodynamic force and moments are the sum of all elements forces acting on the blade COG in the global coordinate system. Note that dynamic stall effects are included in the code if the angle of attack exceeds a certain level. This effect will not be further evaluated.

Zhao did validate the blade model against the Horizontal Axis Wind turbine simulation Code 2nd generation (HAWC2), which is an aeroelastic code intendend for wind turbine responses in the time domain [19].
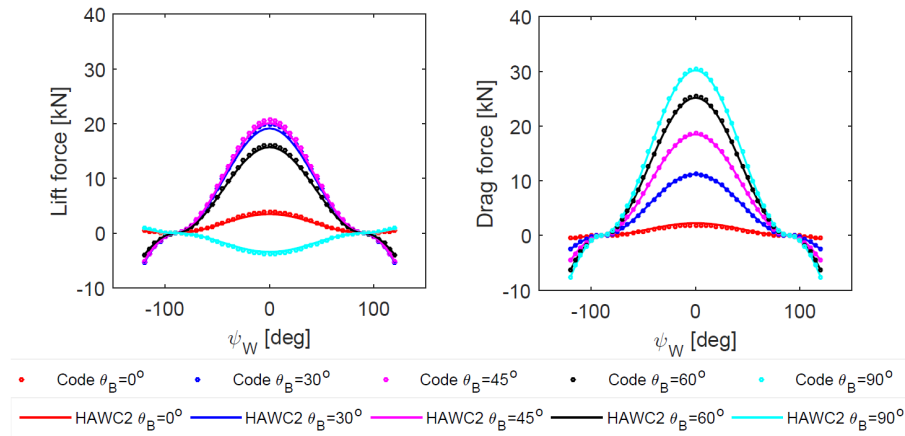
Figure 3.4: *Lift and drag forces for blade with varying pitch angle (θ_B) and wind yaw angle (ψ_W) [19]*

According to figure 3.4, one can see that the model predicts the aerodynamic loads accurately compared to HAWC2. The effects of varying pitch angle of blade and yaw

angle of wind can also be studied from the plots. 0° pitch angle result in the least lift and drag forces on the blade. The wind angle has great influence on the loads on the blade. Head on wind conditions induce the largest forces on the blade, and this blade heading should be avoided during installation.

3.5   Irregular Waves

The irregular waves are generated based on the Joint North Sea Wave Project spectrum, also known as JONSWAP spectrum which is described by:

$$S_\zeta^+(\omega) = \frac{\alpha g^2}{\omega^5} exp\left(-\beta\left(\frac{\omega_p}{\omega}\right)^4\right) \gamma^{exp\left(\frac{\left(\frac{\omega}{\omega_p}-1\right)^2}{2\sigma^2}\right)} \tag{3.7}$$

where α and σ are the spectral parameter, ω_p is the wave peak frequency, β is the form parameter, and γ is the peakedness parameter. To reduce the parameters of the functions, SIMO has included the following relation for α:

$$\alpha = \left(\frac{H_s\omega_p^2}{4g}\right)^2 \frac{1}{0.065\gamma^{0.803} + 0.135} \tag{3.8}$$

By using the default values; $\beta = 1.25$ and $\gamma = 1.0$, and the relation $\omega_p = \frac{2\pi}{\omega_p}$, the wave spectrum can be defined by the significant wave height and the spectral peak period.

3.6   Force Model on Floating Vessel

The rigid body motions of the vessel are solved for at each time step by solving the equation of motion, which is formulated by [26]:

$$\mathbf{M}\ddot{\mathbf{x}} + \mathbf{C}\dot{\mathbf{x}} + \mathbf{D_1}\dot{\mathbf{x}} + \mathbf{D_2}\mathbf{f}(\dot{\mathbf{x}}) + \mathbf{K}(\mathbf{x})\mathbf{x} = \mathbf{q}(t, \mathbf{x}, \dot{\mathbf{x}}) \tag{3.9}$$

The parameters will now be presented consequently. $\mathbf{M}$ is the frequency-dependent mass matrix which is described by the relation:

$$\mathbf{M}(\omega) = \mathbf{m} + \mathbf{A}(\omega) \tag{3.10}$$

where $\mathbf{m}$ is the body mass matrix and $\mathbf{A}$ is the frequency-dependent added mass term. The added mass consists of the added mass for infinite frequency, which is pre-calculated in SIMO, and a frequency-dependent term $\mathbf{a}(\omega)$, which will be further explained later in this section, to get:

$$\mathbf{A}(\omega) = \mathbf{A}_\infty + \mathbf{a}(\omega) \tag{3.11}$$

$\mathbf{C}$ is the frequency-dependent potential mass matrix and is similarly defined as for $\mathbf{A}$ with the damping for infinite frequency ($\mathbf{C}_\infty$) and a frequency dependent term $\mathbf{c}(\omega)$.

$$\mathbf{C}(\omega) = \mathbf{C}_\infty + \mathbf{c}(\omega) \tag{3.12}$$

The wave radiation of infinite frequency is approaching 0 in amplitude; therefore, $\mathbf{C}_\infty$ is presumed to be 0. The remaining radiation forces are the frequency-dependent-added mass and damping. The convolution theorem is applied to the equation of motion regarding only the frequency dependent coefficients and an inverse Fourier transform is applied to the function and the radiation matrices can be expressed by the pre-defined retardation function $\mathbf{h}(\tau)$:

$$\mathbf{a}(\omega) = -\frac{1}{\omega} \int_0^\infty \mathbf{h}(\tau) sin(\omega\tau) d\tau \tag{3.13}$$

$$\mathbf{c}(\omega) = -\int_0^\infty \mathbf{h}(\tau) sin(\omega\tau) d\tau \tag{3.14}$$

Going back to the equation of motion (3.9), D_1 is defined as the linear damping matrix, which is constant through time. D_2 is the quadratic damping matrix which is disregarded for the vessel. The hydrostatic stiffness term ($\mathbf{K}(\mathbf{x})$) is modelled as a linear stiffness model where the restoring force is expressed by $\mathbf{K}(\mathbf{x}\text{-}x_0)$ where x_0 is the stiffness reference position. $\mathbf{q}(t,\mathbf{x},\dot{\mathbf{x}})$ represents the exciting force vector and consists of the following terms:

$$\mathbf{q}(t, \mathbf{x}, \dot{\mathbf{x}}) = \mathbf{q}_{WI} + \mathbf{q}_{WA}^{(1)} + \mathbf{q}_{WA}^{(2)} + \mathbf{q}_{CU} + \mathbf{q}_{ext} \tag{3.15}$$

$\mathbf{q}_{WI}$ is the wind induced forces on the elevated hull and the force is calculated by:

$$\mathbf{q} = \mathbf{C}(\alpha)v^2 \tag{3.16}$$

where $\mathbf{C}$ is the wind force coefficient matrix, v is the relative wind speed between body and wind, and α is the relative velocity direction in the local coordinate system. The relative wind speed is calculated by use of the low frequency motions of the body. However, these motions are disregarded and the relative wind speed is taken as the original wind speed. Moving on in equation 3.15, $\mathbf{q}_{WA}^{(1)}$ and $\mathbf{q}_{WA}^{(1)}$ are the first- and second-order wave excitation forces. These are described by potential flow theory. The first first-order wave excitation force is described by:

$$q^{(1)}(t) = \frac{1}{2\pi} \int_{-\infty}^\infty h^{(1)} \zeta(t - \tau_1) d\tau_1 \tag{3.17}$$

where $h^{(1)}$ is the linear impulse response function which is assumed to be smooth, absolutely integrable and possess the following Fourier transforms [26]:

$$h^{(1)}(\tau) = \frac{1}{2\pi} \int_{-\infty}^{infty} H^{(1)}(\omega)e^{i\omega\tau} d\omega \tag{3.18}$$

$$H^{(1)}(\omega) = \int_{-\infty}^\infty h^{(1)}(\tau)e^{-i\omega\tau} d\tau \tag{3.19}$$

$H^{(1)}$ is the first-order transfer function, which has been defined by utilization of hydrodynamic simulation tools. The Newmark-Beta predictor-corrector method is used for the numerical integration. The only second-order wave excitation force included

in this study is the slowly-varying wave drift force. A simplified method is utilized
where the wave drift forces are pre-calculated for a number of headings before the
time domain simulation, and interpolate between these functions in the time domain.

The next term in equation 3.15 is $\mathbf{q}_{CU}$, which is the forces from the current. However,
no currents are applied to the model, and it will not be further investigated. The
last term in the equation consists of all the other forces that the model may contain.
In this instance, these mainly consist of the stationkeeping forces, which is provided
by the DP-system. The DP-system is simplified as linear springs in surge, sway, and
yaw. Furthermore, 70% of the critical damping of the vessel is applied to the same
DOFs. This is a fair assumption considering that a modern installation vessel are
able to achieve this kind of damping.

3.7 Coordinate System and Vessel Heading

The orientation of the crane is 90 degrees compared to the vessel heading, i.e the
operation takes place on the starboard side of the vessel.

(a) *View from y-direction*   (b) *View from x-direction*
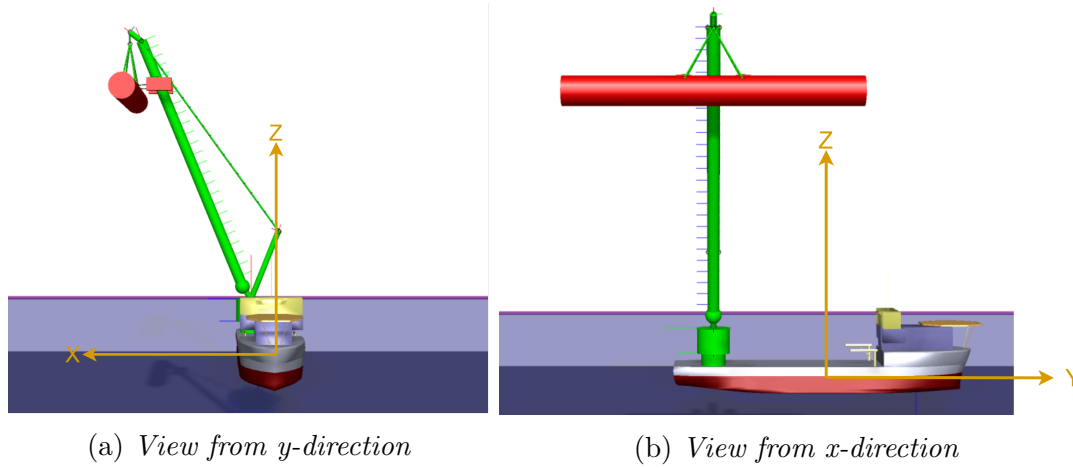
Figure 3.5: *Vessel and crane models*

The vessel and crane 3D graphics can be seen from figure 3.5. The blade is pro-
jected as a cylinder for illustration purposes. The vessel's heading is along positive
y-direction. Floating vessels are typically very sensitive to beam sea because of large
resonance roll motions of the vessel. During operation, beam sea should be avoided;
therefore, this condition can be disregarded. The sea conditions that will be con-
sidered in this section is in the range between head sea and bow sea. In the global
coordinate system in SIMA, the environment direction will therefore be between 225-
and 270 degrees. These environmental directions will be referred to as 45°/bow- and
0°/head sea respectively, and are denoted θ.
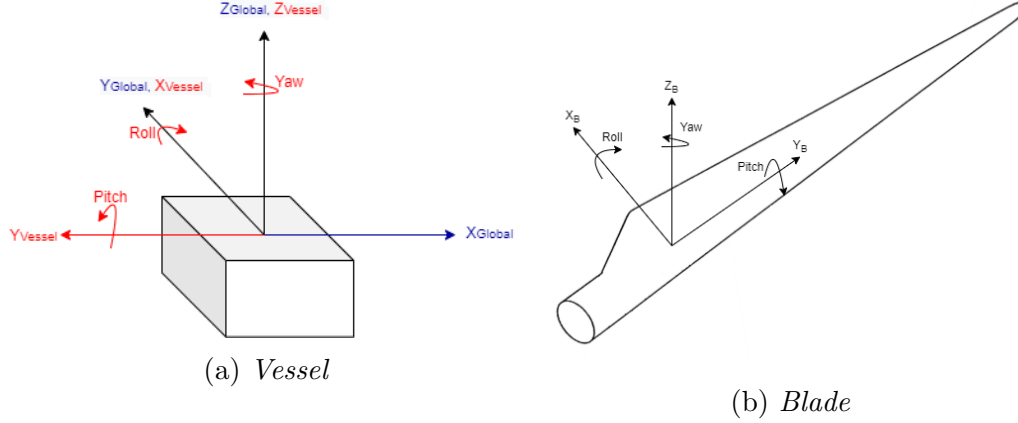
(a) *Vessel*

(b) *Blade*

Figure 3.6: *Local coordinate systems*

The origin of the global coordinate system is in the COG of the vessel. As mentioned, the vessel's coordinate system is flipped 90 degrees compared to the global coordinate system. The blade's coordinate system is directed in the same way as the global coordinate system and is located in the COG of the blade. It is important to emphasize that when referring to the motions of the bodies, the local coordinate system is utilized as a reference. For instance, the vessel's roll motion is not about the global x-axis, but the vessel's x-axis.

3.8   Local Motion

The motions obtained from SIMA are rigid body motions at the center of gravity of the body. However, there are other points of interest along the body of the blade. Blade root motion is of importance due to the response criteria set in section 2. This motion, or any motion along the body, can be found by:

$$\mathbf{s} = \eta_1 \mathbf{i} + \eta_2 \mathbf{j} + \eta_3 \mathbf{k} + \mathbf{w} \mathbf{X} \mathbf{r} \tag{3.20}$$

where x denotes the vector product and $\mathbf{w} = \eta_4 \mathbf{i} + \eta_5 \mathbf{j} + \eta_6 \mathbf{k}$ and $\mathbf{r} = x\mathbf{i} + y\mathbf{j} + z\mathbf{k}$. where x,y, and z are the local coordinates of the point of interest and η_{DOF} represents the rigid body motions in each degree of freedom.
This gives the following:

$$\mathbf{s} = (\eta_1 + z\eta_2 - y\eta_6)\mathbf{i} + (\eta_2 - z\eta_4 + x\eta_6)\mathbf{k} + (\eta_3 + y\eta_4 - x\eta_5)\mathbf{k} \tag{3.21}$$

The equation disregard the fact that there is some structural motion of the blade. This motion is assumed to be small compared to the rigid body motion and neglected for this thesis.

Global Response Analysis

This section focus on the responses of the blade in different environmental conditions. The wind and waves are generated in the time domain. The process is assumed to be stationary; therefore, the effect of lifting and moving around the blade is neglected. The main cases consider irregular waves, but some regular wave cases are investigated to identify the systems' natural periods and get the linear responses. All irregular waves cases examined consider a time series of 800 seconds where the first 200 seconds are removed to exclude transient effects. The time step utilized is 0.01 seconds to ensure convergence of the code; however, the sampling frequency is set to 20 Hz to reduce the size of the data sets.

4.1 Static Results

The static condition of the model was calculated and tabulated in table 4.1. One can see a difference in the initial- and equilibrium position of the blade. That is because the pretension in the tugger lines is applied by shortening the tugger line length. Therefore, the blade is out of position when initializing the simulation. The equilibrium position is then obtained for the blade. The tugger line tension was expected to be 80 kN, but a non-concerning discrepancy in the tension was identified. The lift wire tension should equalize the weight of the blade, yoke, and crane hook. The blade and yoke have a total mass of 88.67t, and the crane hook has a mass of 10t. Therefore, a lift wire tension of 981.1 kN seems reasonable.

Table 4.1: *Static results*

Blade initial position [m]	(49.26,-74.20, 119.59)
Blade eq. position [m]	(46.06,-74.20, 119.35)
Blade initial pitch angle [deg]	0.0
Blade eq. pitch angle [deg]	9.01
Tugger line tension [kN]	80,6
Lift wire tension [kN]	981.1

4.2   Regular Wave Cases

First-order transfer motion functions of the floating vessel were provided by the hydrodynamic software simulation tool HydroD. To verify that SIMA simulates accurate motions of the floating vessel, motions RAOs were computed from regular waves. SIMO generated 100 regular waves in the time domain, and the mean amplitude of the last 50 waves was measured to ensure transient effects were minimized. The numerical model was vastly sensitive to regular waves in the resonance domain. Therefore, small waves of heights 0.5m and 0.25m were utilized to ensure the code wasn't diverging.

4.2.1   Head Sea

(a) *Surge*   (b) *Sway*   (c) *Heave*
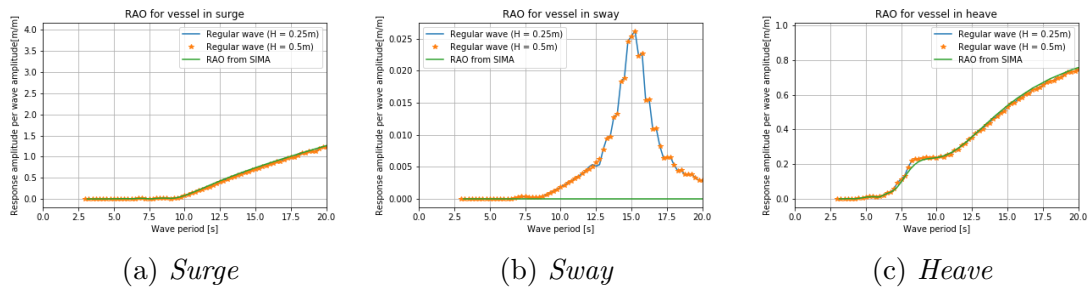
Figure 4.1: *Translation RAOs for floating vessel in head sea*

(a) *Roll*   (b) *Pitch*   (c) *Yaw*
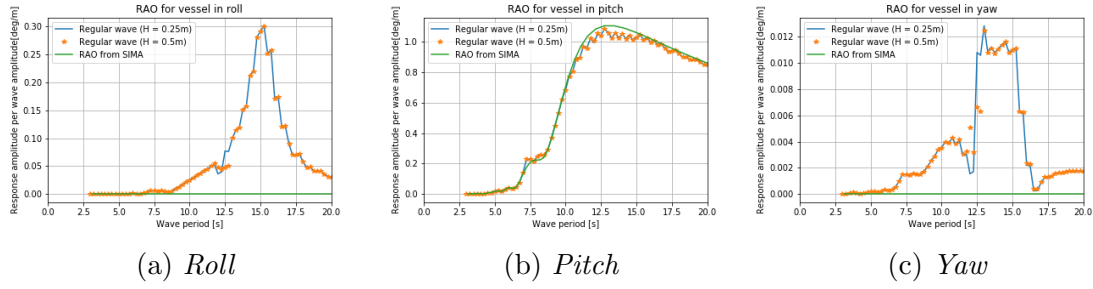
Figure 4.2: *Rotation RAOs for floating vessel in head sea*

The computed RAOs were plotted against the ones given in the model. Remark that the RAOs taken from the model are for the vessel only and do not include the crane. Therefore, some discrepancies in the RAOs are expected. For the degrees of freedom where high motions are expected, the calculated RAOs seem to be reasonably accurate compared to the predefined transfer functions in the model. On the other hand, for the RAOs where low motions are expected in head sea, the computed transfer function estimates higher motions compared to the ones given. One can see that the model RAOs are close to zero for sway, roll, and yaw. Zero motions for these degrees of freedom are expected for a symmetric body. However, the model becomes unsymmetrical due to the crane. Therefore, small amplitudes are obtained for these degrees of freedom.

(a) *Surge*   (b) *Sway*   (c) *Heave*
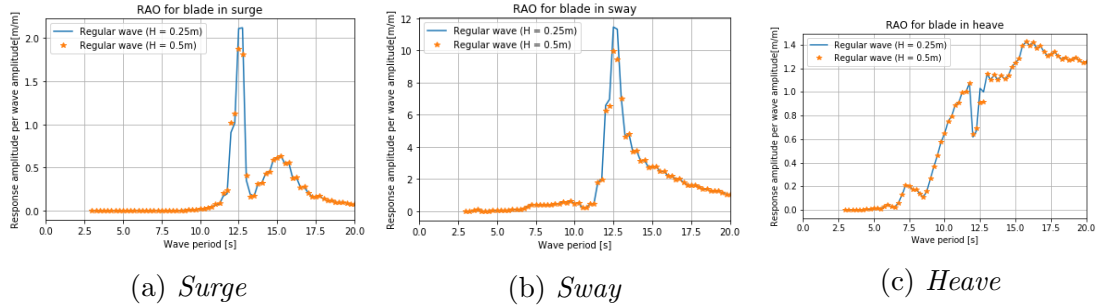
Figure 4.3: *Translation RAOs for blade in head sea*

(a) *Roll*   (b) *Pitch*   (c) *Yaw*
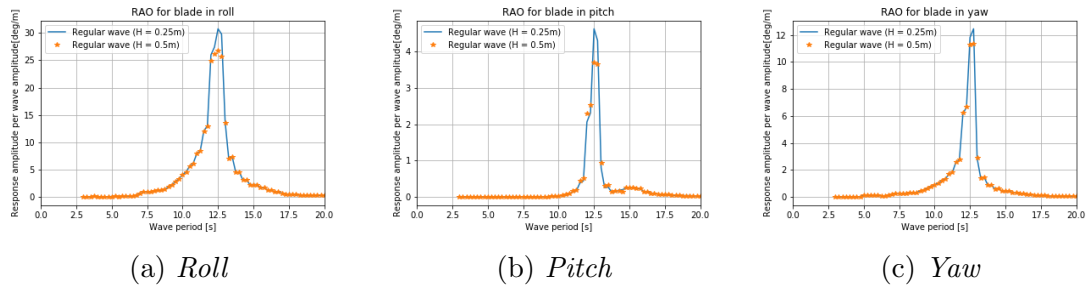
Figure 4.4: *Rotation RAOs for blade in head sea*

Furthermore, the transfer functions for the blade motions were constructed. As seen,

extreme motions are predicted for wave periods around 12 seconds. This is in the same region as where large vessel motions are expected. The causes of the motions may be slack in the blade's tugger lines or pendulum resonance motion and need to be further investigated.

(a) *All periods*   (b) *Snippet of first 10 periods*
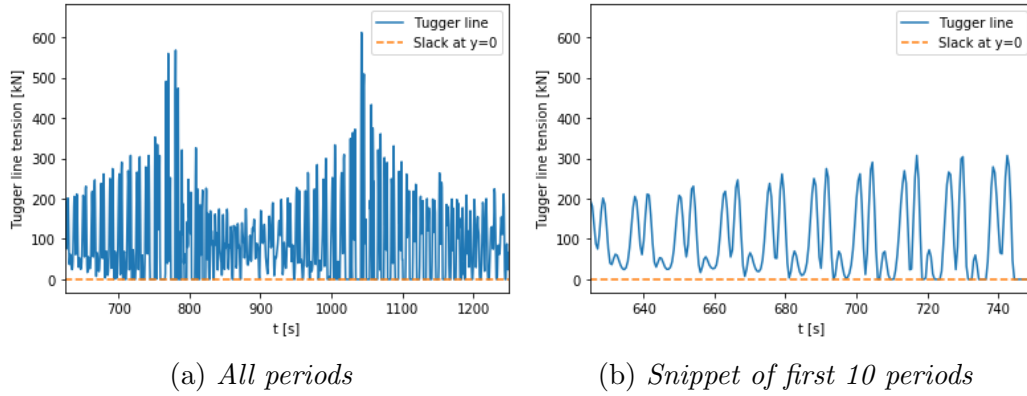
Figure 4.5: *Tugger line tension*

The tugger line tension was further investigated at the most critical period, at T = 12.5s. The tension for the first ten periods of the considered time series is illustrated in figure 4.5. One can see that slack in the line is achieved for most of the generated waves. When generating regular waves, cyclic motion is expected when considering a stable system. However, when the lines go slack, the subsequent event makes the system unstable. Then, transient effects from the previous wave affect the next one. Slack should be avoided at all costs during an operation. The operational criteria's chance of being fulfilled when slack in the lines occurs is slim to nothing.

4.2.2   Bow Sea

(a) *Surge*   (b) *Sway*   (c) *Heave*
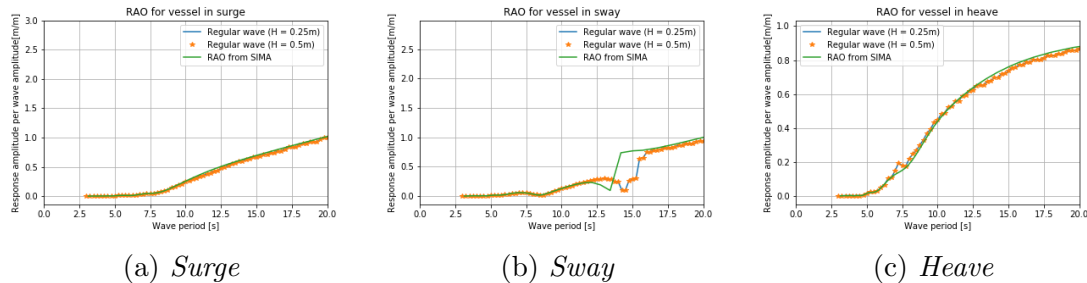
Figure 4.6: *Translation RAOs for floating vessel in bow sea*

(a) *Roll*   (b) *Pitch*   (c) *Yaw*
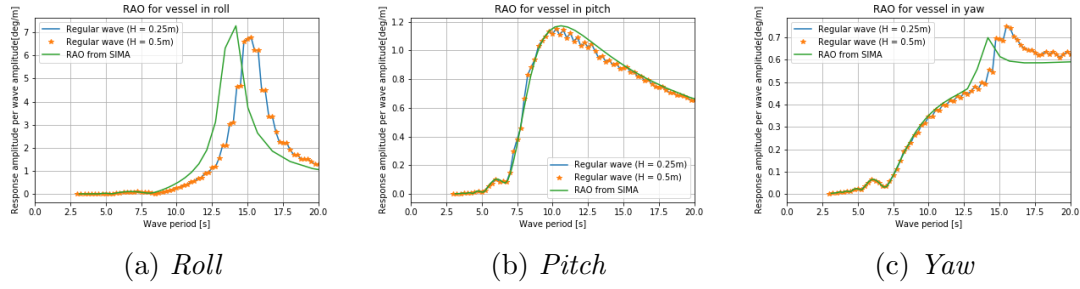
Figure 4.7: *Rotation RAOs for floating vessel in bow sea*

Similarly to as in head sea condition, the RAOs were constructed for bow sea condition. The RAOs show that the maximum amplitudes for the vessel in sway-, roll-, and yaw motion have shifted to higher wave periods when including the crane in the calculations. The restoring forces for sway- and yaw are typically due to the stationkeeping system, which are modeled as springs. The increased mass of the system leads to higher inertia forces which may typically increase the natural period of the system. The roll motion of the ship is shifted due to the mass being added at the starboard side of the vessel. Then, the radii of gyration increase while the transverse metacentric height decreases. These will both have an increased effect on the vessel's natural period estimated by:

$$T_{n4} = 2\pi \sqrt{\frac{Mr_{44}^2 + A_{44}}{\rho g V G \bar{M}_T}} \tag{4.1}$$

(a) *Surge*   (b) *Sway*   (c) *Heave*
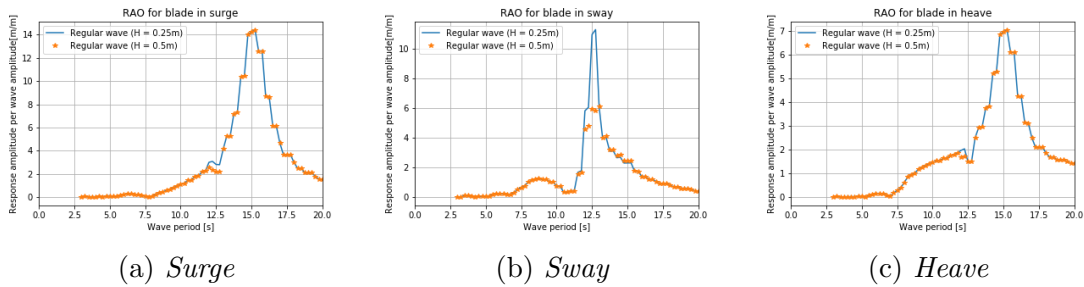
Figure 4.8: *Translation RAOs for blade in bow sea*

(a) *Roll*   (b) *Pitch*   (c) *Yaw*
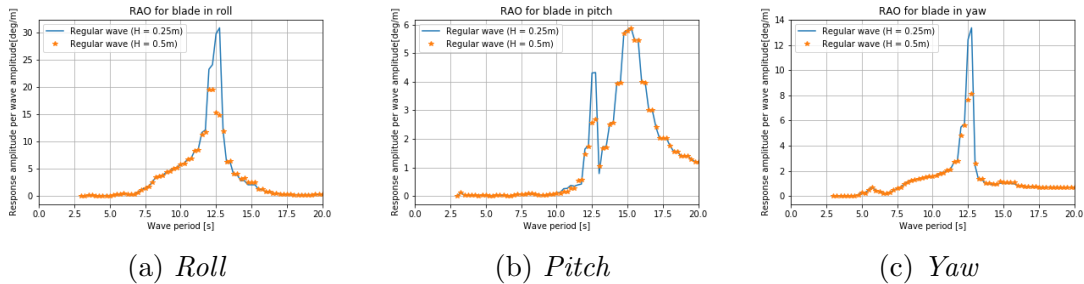
Figure 4.9: *Rotation RAOs for blade in bow sea*

Large amplitudes were obtained for all RAOs, mostly in the region between 12s and 15s. The tugger lines were checked for slack for all conditions, and the wave periods that resulted in slack in the tugger lines are tabulated in table 4.2. For these cases, one cannot expect the response-based criteria to be fulfilled.

Table 4.2: *Wave periods where there are slack in the tugger lines*

T_p [s]	12.0	12.25	12.5	12.75	13.0	14.75	15.0	15.25

4.3 Spectral Analysis

Spectral analysis is conducted to identify the motions of the installation system. The most significant results are presented in this section, but spectra for different degrees of freedoms of different bodies are located in appendix A. The following environmental conditions are considered in this section:

Table 4.3: *Environmental conditions considered for spectral analysis (Several values in one cell indicate that the conditions are plotted and inspected simultaneously)*

Environmental condition	H_s [m]	T_p [s]	U_{ref} [m/s]	θ [deg]	TI [%]
Short wave no wind	1.0	5	0	0	N/A
Short wave & wind	1.0	5	10	0	12
Long wave	1.0	12	10	0	12
Bow sea no wind	1.0	5	10	45	12
Bow sea & wind	1.0	5	10	45	12
Turbulent wind	0	0	10	0	12/14/16
Turbulent wind	0	0	10	45	12/14/16
Varying wind & bow sea	5	12	5/10	45	12

To get the spectral density of the response parameters, a fast Fourier transform (FFT) algorithm is applied to the time series to get the discrete Fourier transform (DFT) of the sequence. The Fourier analysis converts the signal to get representation of the time series in the frequency domain. Equation 4.2 expresses the Fourier transformation of u(t).

$$x(\omega) = \int_{-\infty}^{\infty} u(t)e^{-i\omega t}dt \tag{4.2}$$

Furthermore, the response spectrum is computed the same way as the wave elevation spectrum:

$$S_{xx}(w) = \frac{|x(w)|^2}{2\Delta\omega} \tag{4.3}$$

where x(ω) represents the Fourier transform of the sequence.

4.3.1   Short Wave
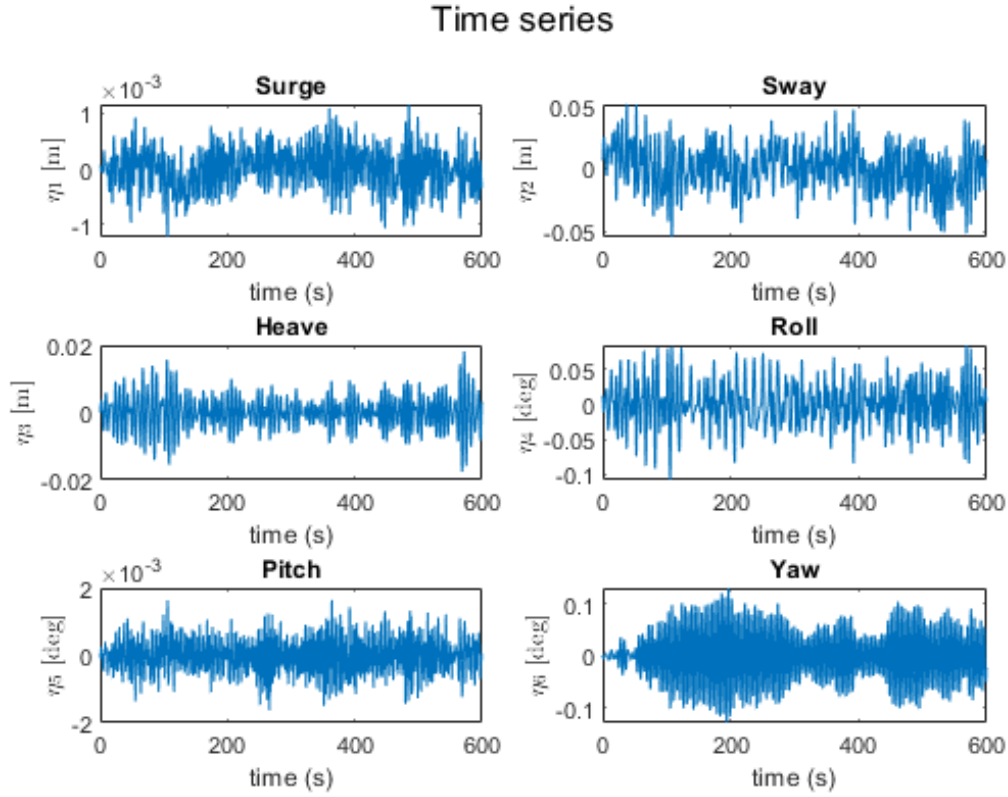
Figure 4.10: *Time series displacement of blade COG in 6 DOF*

Short waves are typically of limited height. To simulate short waves, the significant wave height was chosen to be 1 meter with 5 seconds peak period. Turbulent wind of IEC category C were generated along with the waves. 20 simulations were performed, and the smooth spectral density functions were constructed from the average spectrum of the simulations. The time series displacements of the blade for one simulation are illustrated in figure 4.10. Contributions from the study of Zhao have been utilized to identify some of the motions of the blade [19]. Moreover, spectral density of different cases has been studied to identify the motions of the blade. These can be found in appendix A.

(a) *Surge*   (b) *Sway*   (c) *Heave*

(d) *Roll*   (e) *Pitch*   (f) *Yaw*
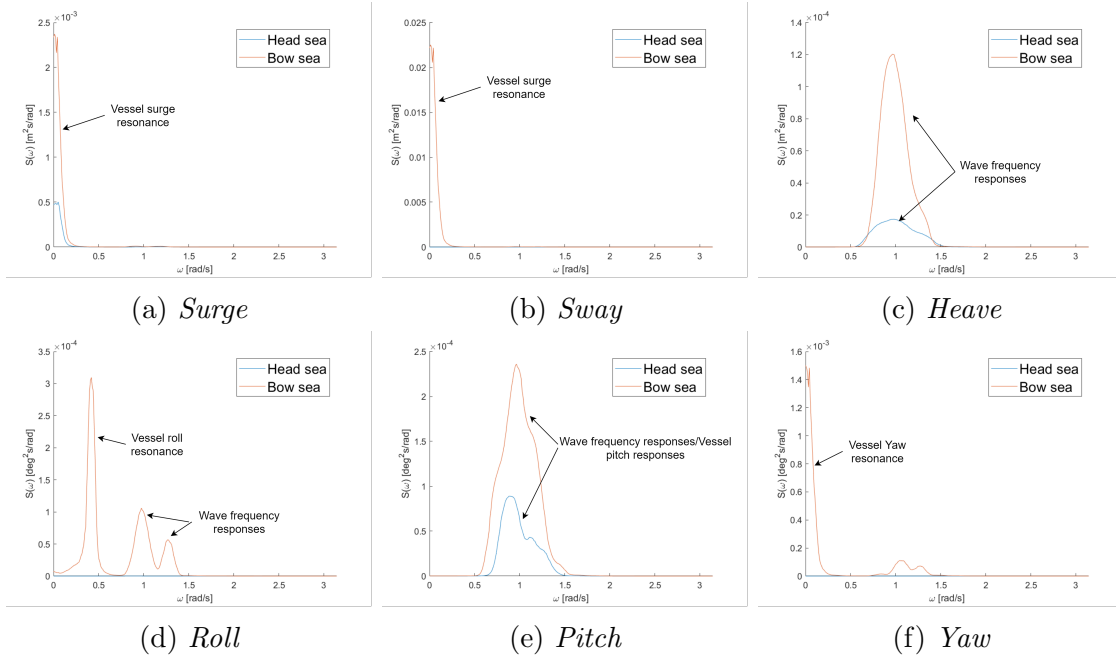
Figure 4.11: *Response spectra for vessel in short waves(H_s = 1m, T_p = 5s, θ = 0°/45°, U_{ref} = 10m/s, TI = 12%)*

First of all, the motions of the vessel were investigated for head and bow sea. One can see from figure 4.11 that the bow sea-state is the most influential of the vessel displacements for all degrees of freedom. The low-frequency motions of the DP-system are identified for surge, sway, and yaw. These are not very concerning since they vary slowly. Moreover, roll resonance is induced for bow sea only. Pitch resonance is achieved around 12.5s periods. In figure 4.11e, one can identify the wave frequency responses being shifted leftwards, which are contributions from vessel pitch resonance.

(a) *Roll*   (b) *Yaw*
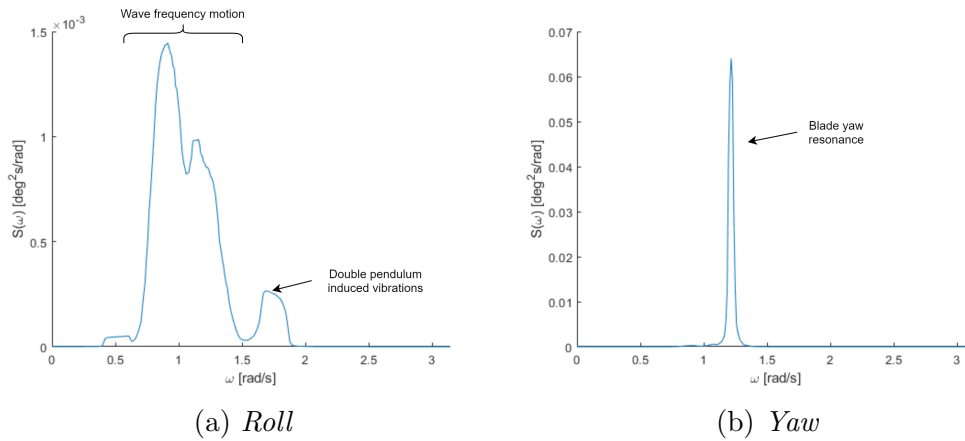
Figure 4.12: *Response spectra for blade COG in short waves (H_s = 1m, T_p = 5s, θ = 0°, U_{ref} = 0m/s)*

The spectra for the displacements of the blade were inspected without wind condi-

tions. The roll and yaw motions were the most significant. The blade roll resonance motions, also known as pendulum motions, were induced by the waves. Also, a contribution from double pendulum induced vibrations could be identified. Blade yaw resonance occurs in the same frequency region as the wave, leading to the blade's significant responses.

(a) *Roll*   (b) *Yaw*
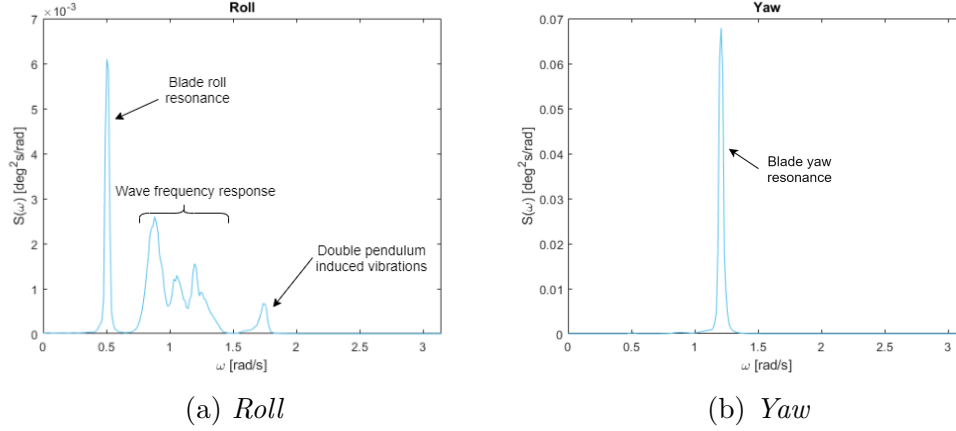
Figure 4.13: *Response spectra for blade COG in short waves and turbulent wind (H_s = 1m, T_p = 5s, θ = 0°, U_{ref} = 10m/s, TI = 12%)*

Turbulent wind was added to the simulations. The turbulent wind causes some roll motion to the blade, which occurs at 0.5 rad/s, and a minor contribution from this motion can be identified in figure 4.13a. Yaw motion of the blade is more or less unaffected by the wind and is found to be the most critical response for short waves in head sea. This motion is highly related to the behavior of the tugger lines.

(a) *X-component*

(b) *Y-component*
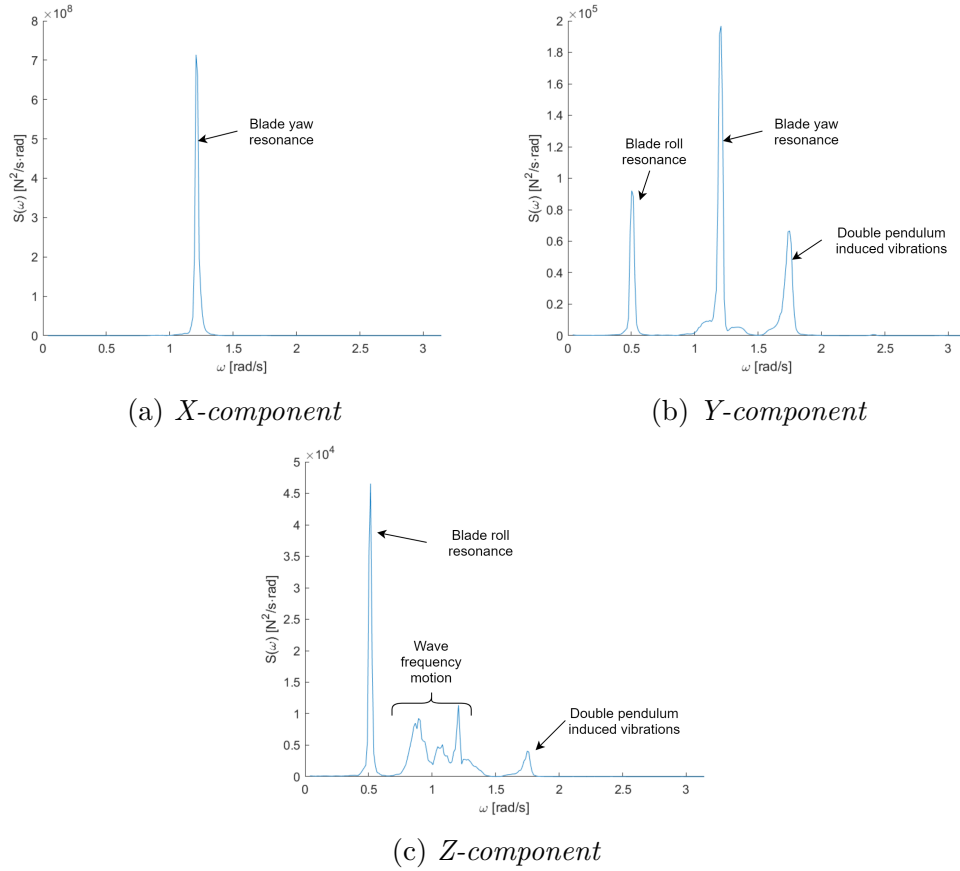
(c) *Z-component*

Figure 4.14: *Force response spectra for tugger line tension in short waves ($H_s = 1m$, $T_p = 5s$, $\theta = 0°$, $U_{ref} = 10m/s$, TI=12%)*

The component-wise force responses of one of the tugger lines are inspected in figure 4.14. One can see the x-component of the tension is significantly denser than the two others. This was expected since the tugger lines are mainly directed along the global x-axis. The peak located at 1.2 rad/s also emphasizes the correlation between the tugger lines and blade yaw motion. The y-component tension has contributions from roll-, and yaw resonance, along with double-pendulum-induced vibrations. Lastly, the z-component force is dictated by blade roll resonance. However, the two latter are insignificant compared to the x-component force.

(a) $U_{BR,x}$ (b) $U_{BR,y}$
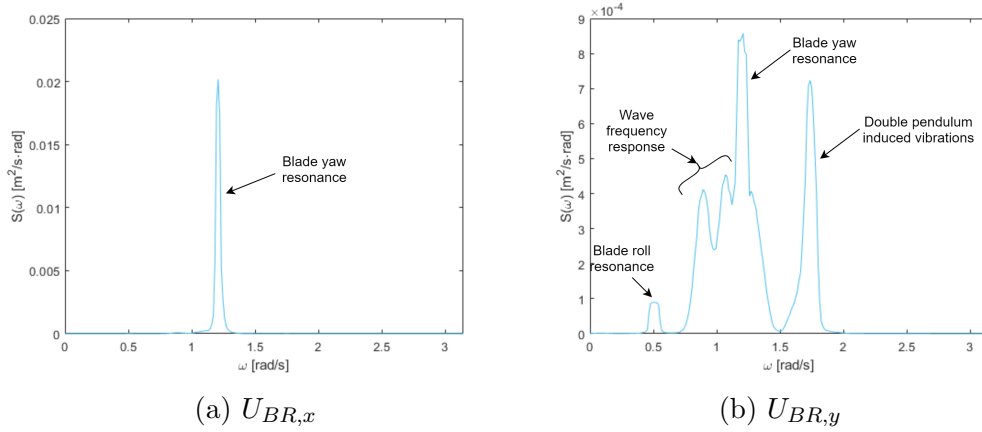
Figure 4.15: *Velocity spectra for blade root in short waves($H_s = 1m$, $T_p = 5s$, $\theta = 0°$, $U_{ref} = 10m/s$, $TI = 12\%$)*

The velocity spectra were studied for blade root motion. Blade yaw resonance governs the transverse motion of the blade. The radial blade motions are mainly affected by double pendulum induced vibrations and yaw resonance; however, the density of this spectra is considerably low. For short waves, the transverse motions of the blade root is the most critical motion given the response criteria. Nevertheless, the transverse motions are neither of great amplitude.

4.3.2   Long Wave

The long waves were simulated with significant wave height of 1 meter and peak period of 12 seconds. The same wind conditions as for short waves were generated. Likewise to short wave, the response spectra were constructed for the blade.

(a) *Surge*

(b) *Sway*

(c) *Roll*

(d) *Yaw*
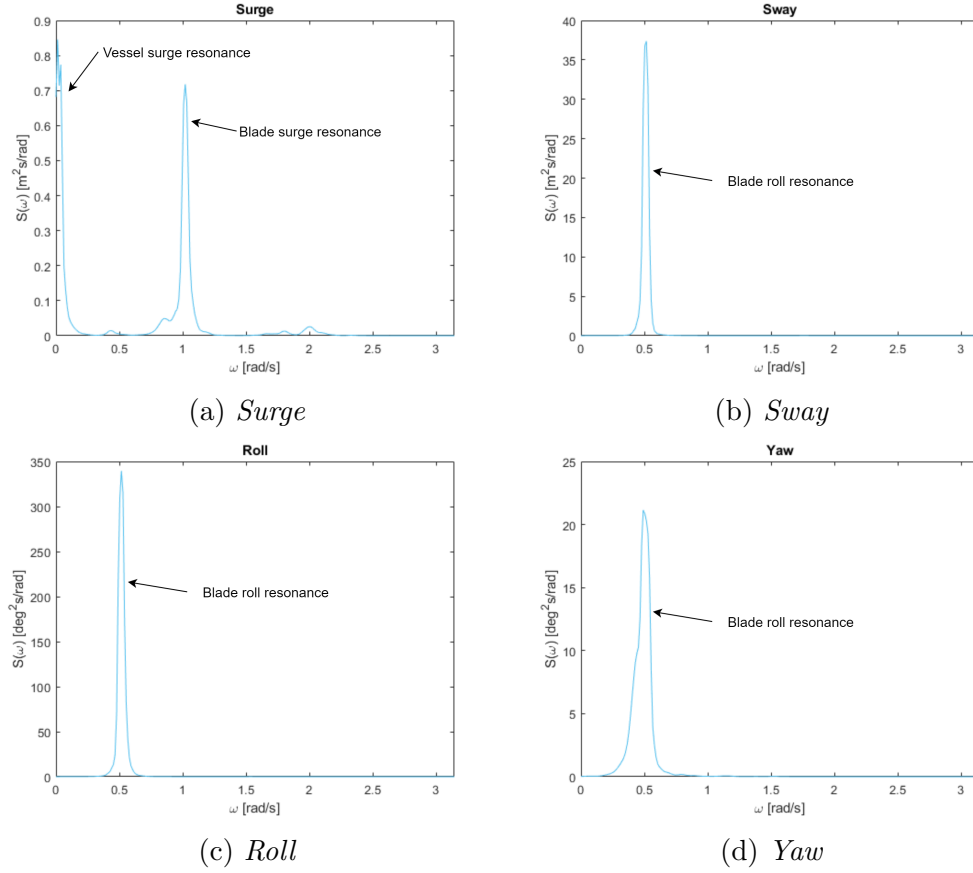
Figure 4.16: *Response spectra for blade COG in long wave ($H_s = 1m$, $T_p = 12s$, $\theta = 0°$, $U_{ref} = 10m/s$, $TI = 12\%$)*

Blade roll resonance dictate the motions of the blade as seen in figure 4.16. The resonance motion occur in the same frequency region as the wave frequency. The natural period of the vessel pitch resonance is also in this region. The results are substantial blade motions.

(a) $U_{BR,x}$

(b) $U_{BR,y}$
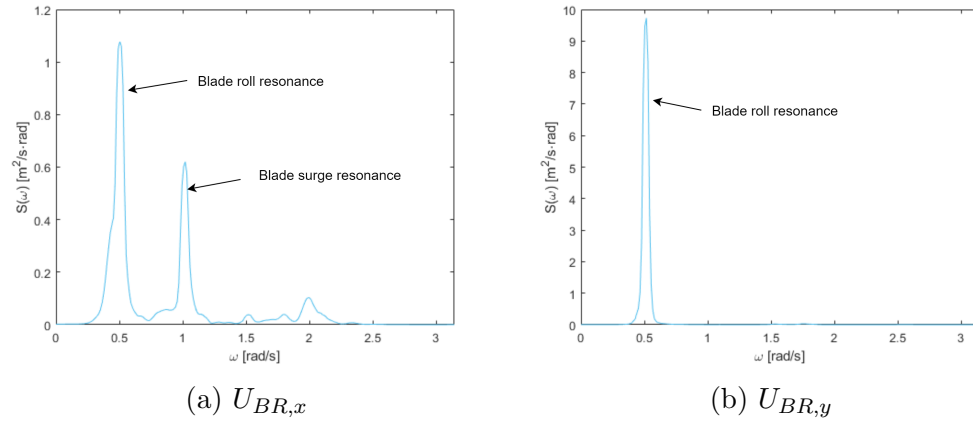
Figure 4.17: *Velocity spectra for blade root in long waves ($H_s = 1m$, $T_p = 12s$, $\theta = 0°$, $U_{ref} = 10m/s$, $TI = 12\%$)*

The roll resonance of the blade dominate the velocity spectra of the blade root as well. Contribution from blade surge resonance is identified for transverse velocities. In contrast to the short wave, the radial velocity of the blade is the most critical motion of the blade root. The functions are extensively denser than for short wave, and one cannot expect the operational limits to be satisfied in this kind of waves.
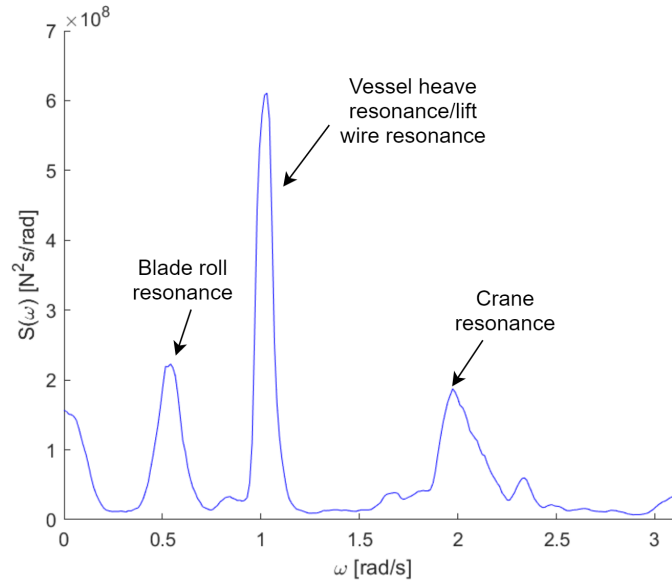
Figure 4.18: *Force spectra for lift wire tension in long waves (H_s = 1m, T_p = 12s, θ = 0°, U_{ref} = 10m/s, TI = 12%)*

The force spectra of the lift wire can be seen in figure 4.18. The vessel resonant heave motion induce increased tensions in the lift wire, and one can expect vertical responses of the blade. There are also some contributions from the structural motions of the crane, and blade roll resonance.

4.3.3   Bow Sea

In this case, the vessel was heading 45 degrees compared to the environmental condition. Only short waves are considered for this scenario, because the motions for long waves are expected to be too large in order to satisfy the response-based criteria.

(a) *Sway*   (b) *Roll*   (c) *Yaw*
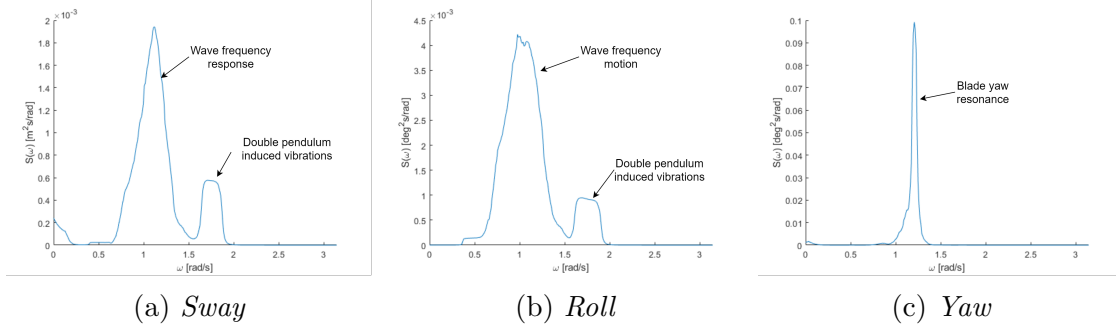
Figure 4.19: *Response spectra for blade COG in bow sea and short waves (H_s = 1m, T_p = 5s, θ = 45°, U_{ref} = 0m/s)*

Blade sway- and roll motions are mainly affected by the waves frequencies, but some contributions from the double pendulum vibrations are recognized. Nonetheless, blade yaw resonance is induced.

(a) *Roll*   (b) *Yaw*
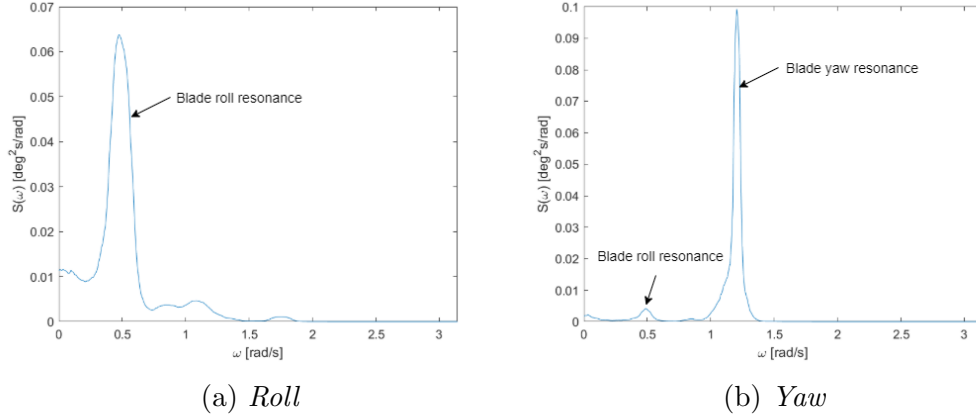
Figure 4.20: *Response spectra for blade COG in bow sea and short waves (H_s = 1m, T_p = 5s, θ = 45°, U_{ref} = 10m/s, TI=12%)*

The wind infect the roll motions of the blade, but do not contribute to increase yaw motion. More or less the same motions as for head sea are dictating the displacement pattern of the blade. Yaw is the most critical degree of freedom; however, the influence of roll motion of the blade has been amplified in this scenario. Also, there is some contribution from the low-frequency motions of the DP-system. The density of the functions have increased compared to head sea, which indicate that head sea is the more favourable sea-state.

(a) $U_{BR,x}$ (b) $U_{BR,y}$
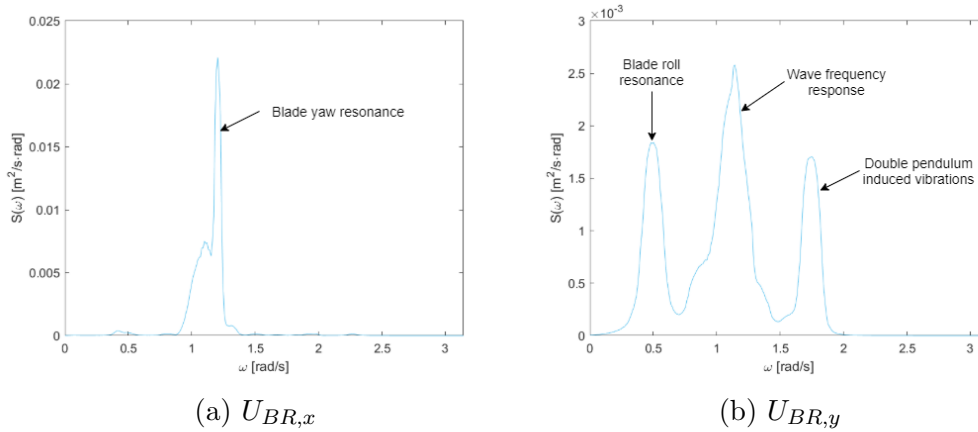
Figure 4.21: *Blade root velocity spectra $H_s = 1m$, $T_p = 5s$, $\theta = 0°$, $U_{ref} = 10m/s$*

There is a clear dominance from the blade yaw resonance response for the transverse velocity component; however, the in-line velocities are mainly following three different motion paths. The transverse velocity is the critical component at this sea-state, but for longer waves, the in-line velocity will amplify as the contribution towards blade roll resonance increases.

4.3.4   Turbulent Wind

(a) *Sway*   (b) *Roll*   (c) *Yaw*
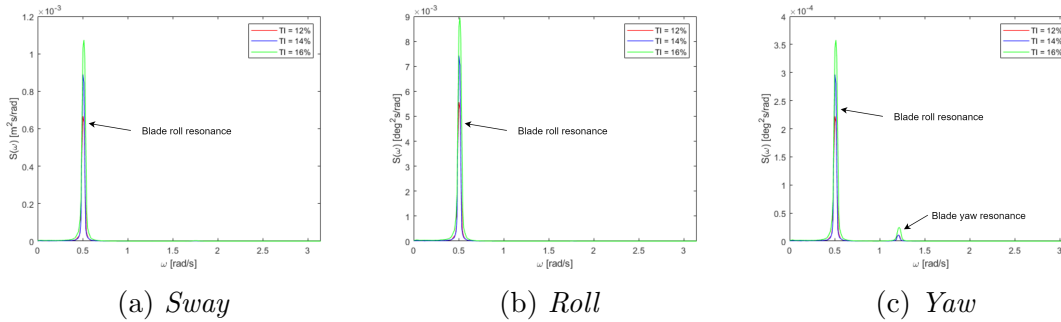
Figure 4.22: *Spectral density functions for turbulent wind for $U_{ref} = 10m/s$, $\theta = 0°$*

The impact of the turbulent wind was further investigated. Turbulent wind with different TI according to IEC class A, B, and C were simulated. One can see that blade roll resonance dominate the spectra. The TI doesn't seem to affect the motion path, but the response amplitudes. Increasing TI lead to increasing peakedness of the spectral density functions which lead to greater resonance motion.

(a) *Sway*   (b) *Roll*   (c) *Yaw*
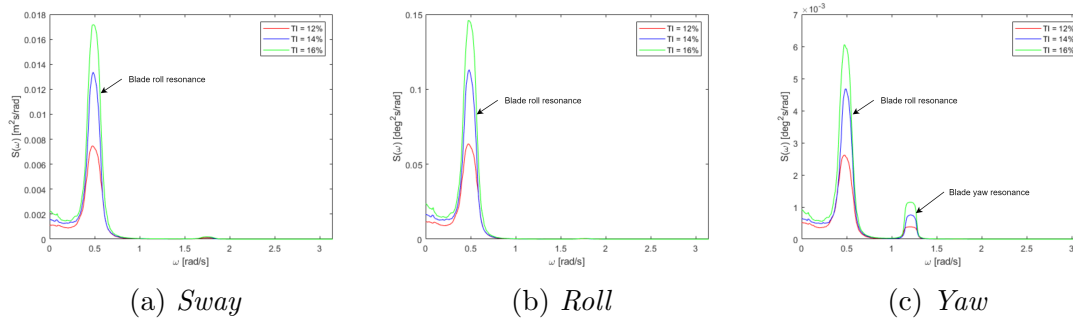
Figure 4.23: *Spectral density functions for turbulent wind for $U_w = 10m/s$ for 45 degrees heading*

Turbulent wind were also simulated from 45 degrees heading. In this scenario, a larger area of the blade is affected by the wind and one can expect greater motion amplitudes. Once again, the blade roll pendulum motion govern the behaviour of the blade.

(a) *Roll*   (b) *Yaw*
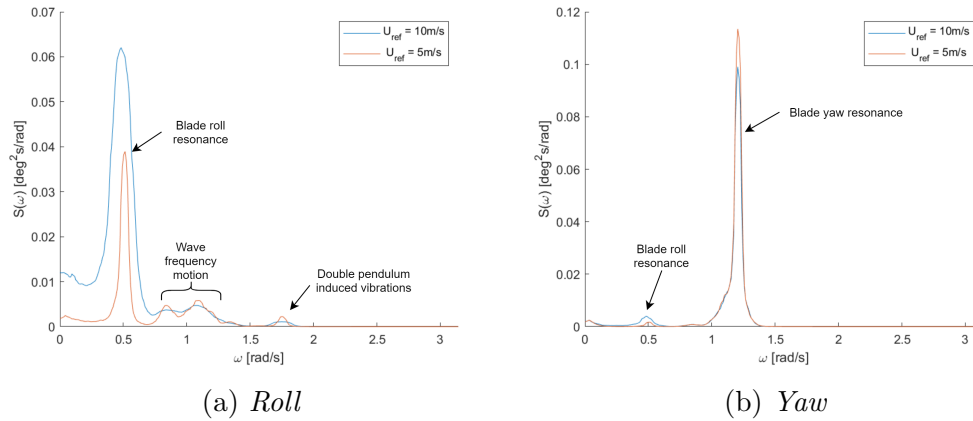
Figure 4.24: *Response spectra for $H_s = 1m$, $T_p = 5s$, $\theta = 0°$*

Even though the combination of wind and wave has already been investigated, the implications of varying wind speed are yet to be explored. One would think that the blade motions increase for higher wind speeds; however, another behavior was detected for bow sea. The blade yaw resonance motion is more significant for a reference wind speed of 5m/s than for 10m/s, as seen in figure 4.24b. It seems like the wind has a damping effect on the yaw resonance motion. When the blade is out of equilibrium position in yaw, more area of the blade is affected by the wind for positive rotation. Upon which the blade rotates towards the motion amplitude in the positive direction, the wind will have a greater effect and decrease the response amplitude. When the blade rotates in the opposite direction, less area of the blade is caught by the wind, and the wind will not push the blade out of position to the degree that it damps positive yaw motion. Therefore, the overall response amplitude in yaw may be decreased when wind act upon the blade from a 45-degree direction. On the other hand, increasing wind amplifies the blade roll resonance motion. When

the peak periods increase, the blade roll motion will be more significant, and it will be the critical motion. Then, the wind will have an overall negative effect on the operation.

4.4 Short-Term Sea State Approach

The short-term sea state approach considers a homogeneous and stationary process where the sea states are in a statistical sense characterized by the wave spectrum. After analyzing the spectral density functions, an idea of the behavior of the blade has been established. It was demonstrated that head sea is the most favorable condition and the vessel should try to maintain that heading throughout the operation. For this heading, sea-states of H_s from 0.5 m to 2 m and T_p from 5 s to 14 s in the wind with reference wind speed of 5 or 10 m/s were simulated. If the vessel cannot keep this favorable heading for the operation, it is beneficial to know the limits of other headings. For bow sea, i.e., 45 degrees heading, the same wind and wave conditions were simulated.
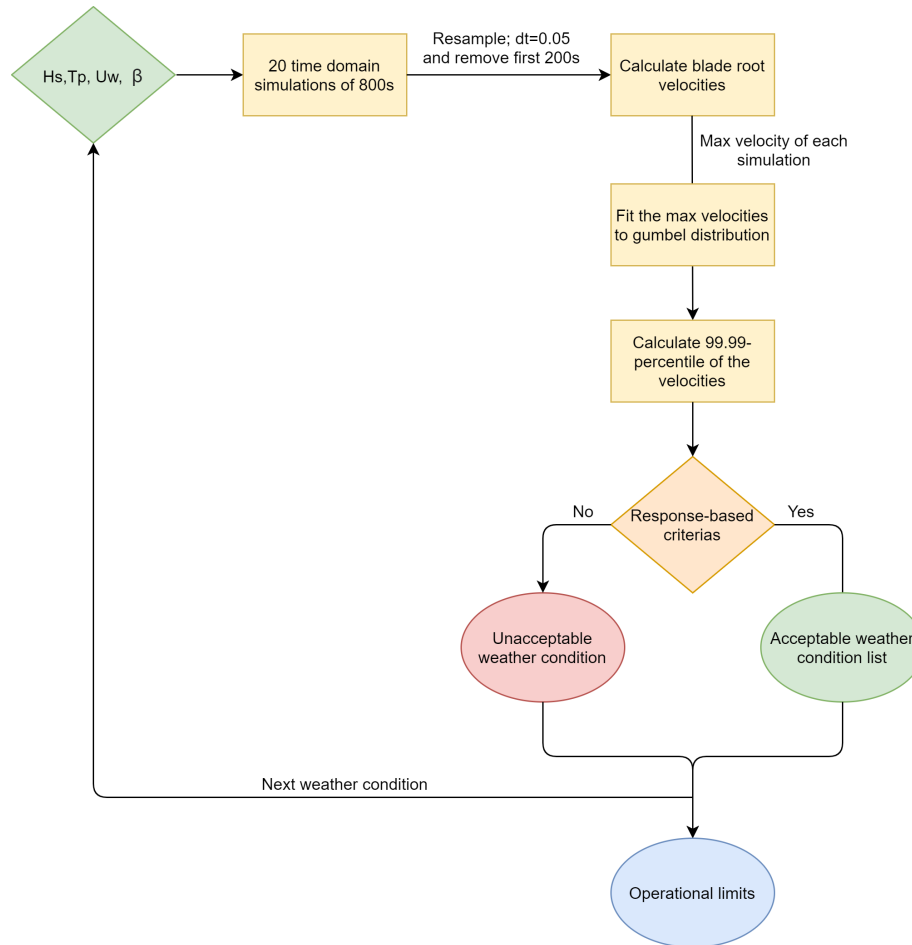
Figure 4.25: *Flow chart of short-term seas state approach*

The process of how the operational limits are derived are summarized in figure 4.25.

20 simulations were performed for each environmental condition. The blade root velocities were further calculated and fitted to the gumbel distribution. Moreover, the $10^{-4} - velocity$ were computed and a check was performed to see if the velocities satisfied the response-based criteria; $U_{BR,x} = 0.76m/s$ and $U_{BR,y} = 1.35$. The max allowable wave heights for each peak period, vessel heading and reference wind speeds were collected to set the operational limits.

4.4.1 Distribution Function

The velocities need to be fit to a extreme value distribution function. The aim was to fit the maximum velocities from each simulation of each sea-state to the Gumbel distribution given by:

$$F_x(x) = exp\Big(-exp\Big(-\frac{x-\alpha}{\beta}\Big)\Big) \tag{4.4}$$

where α and β are parameters of the linear regression line from ordering the maximum values from the analysis in increasing order. The Gumbel distribution is often reasonably accurate when looking at a variable as the largest out of a number of underlying variables. 20-40 simulations are recommended for the data-set to be of sufficient size in order to fit the distribution function. To keep the computational time to the minimum, 20 simulations where chosen; however, to ensure that the data is adequate, the sampled data were fitted to a probability paper. If the sampled data follows a straight line, the Gumbel assumption is to a certain extent supported. Probability paper were made for blade root- and leading edge velocities for $T_p = 5s$, $H_s = 1m$ and $U_w = 10m/s$ where Z can be estimated from equation 4.5.

$$Z = -ln(-ln(\hat{F}_x)) \tag{4.5}$$

where

$$\hat{F}_x = \frac{k}{n+1} \tag{4.6}$$

where k is the index of each simulation and n is the total number of runs.

(a) $U_{BR,x}$ (b) $U_{BR,y}$
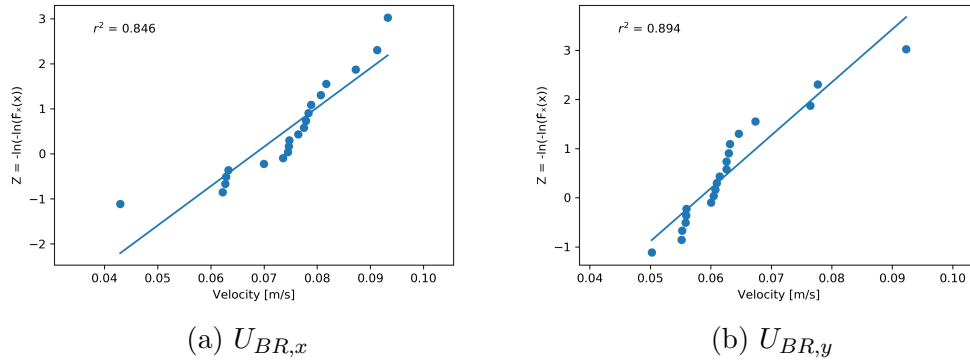
Figure 4.26: *Probability paper for blade root velocities*

The data seem to follow the straight line to some extent for both impact scenarios. However, there are some uncertainty to the fitted model. To get a clearer image of the goodness of the distribution function, a $\chi^2 - test$ was performed. The null hypothesis of the test can be formulated such that the null hypothesis data is taken from the recently constructed CDF. From this fitted model, classes of width (δ_i) is defined such that the probability (p) are the same for each class. This is conveniently done by utilizing the q-percentiles and divide into 5 classes where class 1 consists of the velocities below the 0.2-percentile, class 2 include the velocities between 0.2- and 0.4 percentiles, and so on. 40 new simulations were performed with different random seeds for winds and waves. Furthermore, the maximum blade root velocities were sampled from the simulations. The newly collected maximum velocities are grouped in the classes from the fitted model, to calculate the χ^2-value:

$$\chi^2 = \sum_{k=1}^{m} \frac{(o_k - np)^2}{np} \tag{4.7}$$

where m is the class size, o_k is the number of observed velocities in each class, and np is the expected number of observations given by $np = 40/5 = 8$. The calculated χ^2-value is compared to the χ^2-distribution, where the values of the distribution can be found in tables. The value of interest is the 0.05-significance value of 4 degrees of freedom ($\chi^2_{4,1-0.05}$). The calculated values from the 40 observations for transverse- and in-line velocities were less than $\chi^2_{4,1-0.05}$ and the model cannot be rejected with a significance level of 0.05. Therefore, it seems to be sufficient to do 20 simulations for each environmental condition.

Although the χ^2-test can be performed for each environmental condition, the process will be time-consuming. On the other hand, it is more convenient to keep track of the r^2 parameter for each environmental condition. The statistical measure represents the proportion of the variance for a dependent variable that's formulated by the variables in a regression model. For instance, when $r^2 = 0.846$, this portion of the observed variation, can be explained by the model's input. The observed r^2-values for this scenario were rather low compared to the other simulated conditions. The fact that this condition satisfied the χ^2-test, indicate that the fitted models with higher r^2-values are satisfactory as well. The r^2-values for each environmental condition are tabulated in appendix B.

(a) $U_{BR,x}$ (b) $U_{BR,y}$
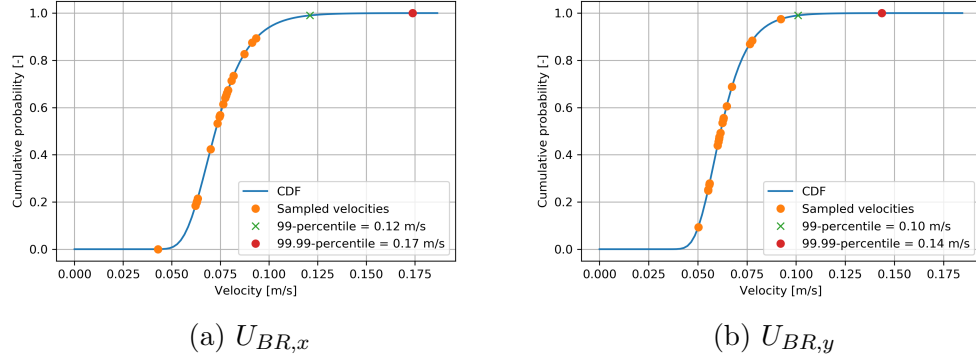
Figure 4.27: *Cumulative distribution functions for blade root velocities*

Furthermore, the sampled velocities were fitted to the distribution function given in equation 4.4. The target safety level was earlier set to a failure probability of 10^{-4} which is the corresponding 99.99 percentile of the cumulative distribution function (CDF). Then, equation 4.8 was solved for each load condition to obtain the 10^{-4} safety level velocities of radial and transverse blade root motion.

$$F_{(U_{BR,x}/U_{BR,x})_{10min}|H_sT_pU_w\beta_{ref}}\big((u_{BR,x}/u_{BR,x})|h,t,u_w,\theta\big) = exp\Big(-exp\Big(-\frac{x-\alpha}{\theta}\Big)\Big) = 1-10^{-4}$$
(4.8)

Figure 4.27 presents the CDF for the case of $T_p = 5s$, $H_s = 1m$ and $U_{ref} = 10m/s$ and the 99.99-percentile of the velocities were obtained. The next step is to evaluate whether the velocities satisfy the response based criteria and if the load case can be included in the safe operational domain. Both response-based criteria have to be satisfied in order to include the environmental case in the safe domain In the scenario of the presented case, both response-based criteria are fulfilled and the operation are assumed to be safely performed for this environmental condition.

4.4.2 Operational Limits

4 different environmental cases were considered with varying peak period and significant wave height to estimate the operational limits. These cases are listed below:

Table 4.4: *Environmental Cases*

EC	T_p [s]			H_s [m]			U_w [m/s]	Env. dir. [deg]
	Start	Stop	Incr.	Start	Stop	Incr.		
EC1	5	14	1	0.5	2.0	0.5	5	0
EC2	5	14	1	0.5	2.0	0.5	10	0
EC3	5	14	1	0.5	2.0	0.5	5	45
EC4	5	14	1	0.5	2.0	0.5	10	45

The operational limits were derived by the aforementioned probabilistic method. These limits are presented in figure 4.28. The lines indicate the greatest wave height for each period where the response-based criteria is accepted. The safe operational domain is considered as the area underneath these lines.
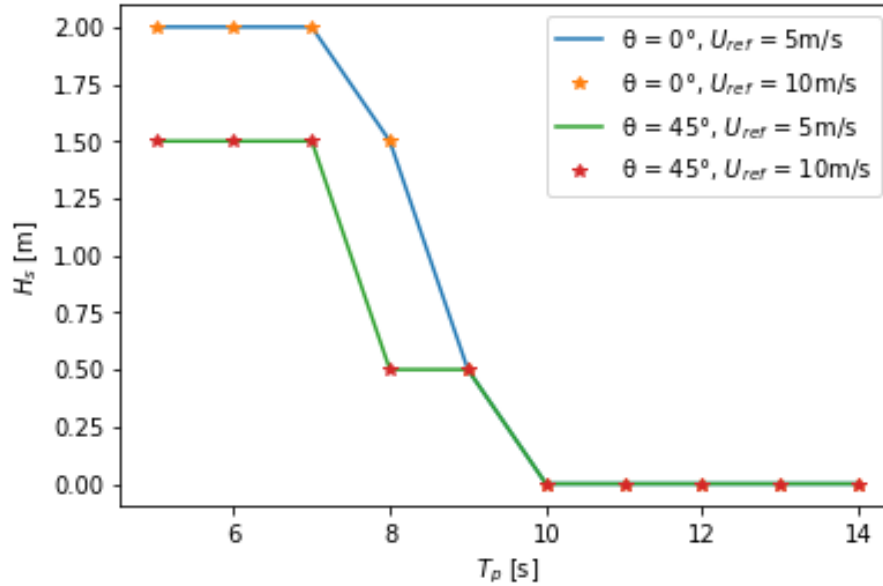
Figure 4.28: *Operational limits for the different environmental conditions*

One can see in the figure that the lines for the two different headings overlap. In other terms, the operational limits are identical for the different reference wind speeds. However, it cannot be presumed that the wind doesn't significantly affect the installation system. The influence of wind was manifested through spectral analysis. Tables that show if the response-based criteria are accepted for every sea-state in the given environmental case can be found in appendix B. They also indicate if only one of the criteria is accepted. For bow sea, there are some sea-states in which only the in-line criterion is accepted. There are more sea-states where this criterion is accepted for $U_{ref} = 10$m/s than for $U_{ref} = 5$m/s, which supports the theory of the wind damping the yaw motions of the blade.

Figure 4.29: *Map of different sites in Europe*

Metocean weather data was obtained for site 14 which is located just of the West Coast of Norway in the North Sea, which is marked in figure 4.29. The data contains sampled weather parameters for 1 hour sea-states from 2001 to 2011. The limiting weather parameters defined in this thesis were sampled to compare to the operational limits derived in this section. 1 hour should be sufficient for installation of a single blade, which means each data point can be weight up against the operational limits. Since the summer months (June, July, August) are usually the most gentle when considering the weather, the data from these months will be selected for evaluation. The spectral peak period, significant wave height, and wind speed were sampled. The wind speed given in the dataset was for a height of 10m above sea surface. To get the same reference wind speed, at 119m above the sea surface, as defined in TurbSim, U_{ref} was back-derived from equation 3.1.
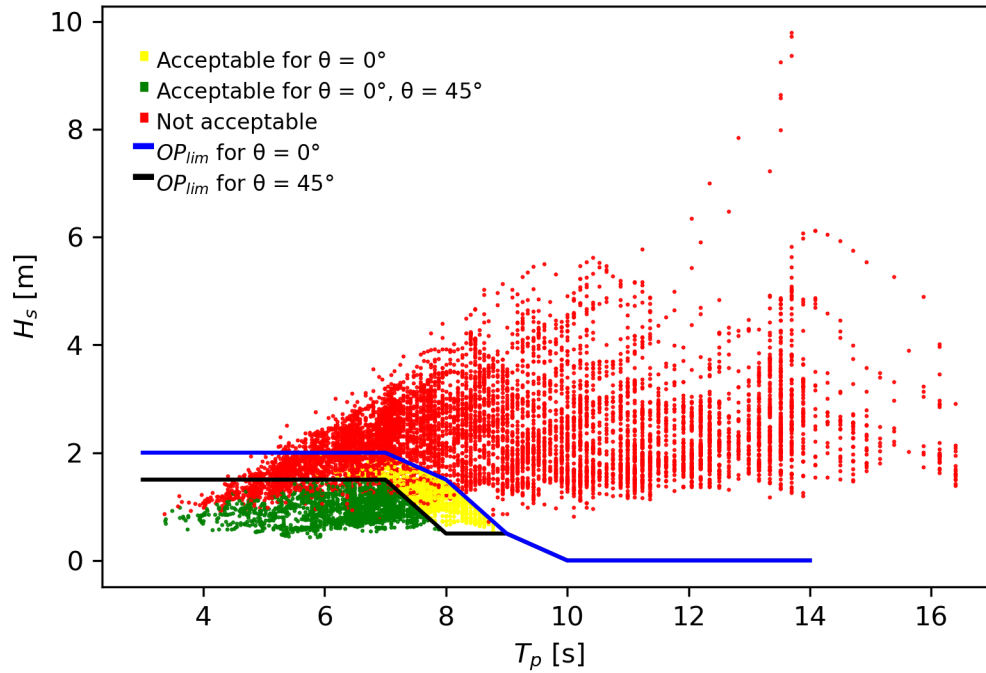
Figure 4.30: *Operational limits compared to metocean data for summer months*

Figure 4.30 presents the sampled weather data for the summer months compared to the operational limits as a function of significant wave height and peak period. The yellow dots represent acceptable sea-states for head sea. Furthermore, the green beads portray the acceptable sea states for both head- and bow sea. At last, the red dots are for unacceptable sea-states. For a sea-state to be considered acceptable, it has to be inside the safe domain, which is the area underneath the operational limit curves. Also, they have to include wind velocities less than 10m/s. Note that wind speeds above 10m/s and wave heights above 2m were not analyzed. This study did not consider peak periods smaller than 5s; however, wave conditions with $Tp < 5s$ are considered acceptable, in light of these waves being of reduced size. As indicated by the figure, most environmental conditions were accepted for neither headings. 3180 environmental-states were acceptable for the favorable heading, head sea. Given the total amount of sea-states as 22080, only 14.4% of the cases were acceptable.

Chapter 5

Discussion

The study includes a fair amount of assumptions. First of all, neglecting the motions of the hub is on the non-conservative side. The responses are likely to move with a different frequency than the blade, which would lead to more significant relative motions between the two bodies within the simulation time. Although the motions of the hub should be remarkably smaller than the blade, including these would improve the precision of the analysis. Secondly, the structural motions of the blade were not included when calculating the local velocity at the blade root. During the operational phase of the turbine, when the blade tip is moving in over a hundred km/h, one can expect significant structural displacements of the blade. However, this is not the case for installation when the motions are of an inferior size. Also, the structural response of the blade root is of a far lesser scale than the blade tip due to the increased structural integrity of this area. Thirdly, this thesis disregarded the transient effects of the installation. The blade root mating phase is executed with high precision at a slow pace during the critical phase. Therefore, the velocities caused by the transient motions of the crane and lift wire are inconsiderable. All these assumptions are non-conservative, but not of significant scale. On the other hand, the response-based criteria had a conservative approach due to direct impact was considered, which did not account for energy dissipation from the surrounding structure. Further investigation on the conservatism of the approach has to be included in order to use the approach for real-time installation. However, this study serves the purpose of examining the feasibility of the installation method.

The statistical uncertainty of a model is always challenging to interpret. A χ^2 goodness of fit test was conducted for one of the cases and it did not reject the null hypothesis of the fitted distribution representing the data, with a significance of 0.05. Even though the result is a good indication of a well-fitting model, one cannot assume that all cases would satisfy this test. Therefore, the study monitored the r-squared values. Most of these values were higher than the r^2 values for the case which was tested. The lowest value obtained was 0.62, which is not of sufficient size to discard the probabilistic model. To reduce the uncertainty of the results, more simulations could have been performed. However, more computational effort would

have been required. Consequently, it was decided that the the probabilistic model was accurate to the extent of the intended study, and 20 simulations were adequate.

The spectral analysis identified the motions of the installation system. In most cases, the governing responses and loads were revealed; however, some environmental cases were more challenging to interpret due to loads and responses acting in the same frequency area. For instance, the yaw spectras revealed blade yaw resonance for short waves, but it was not clear how much effect this response had on the roll motions of the blade, due to the waves acting with similar frequency. Nonetheless, the blade roll responses were rather low for this condition, and not significant compared to the yaw motions. The yaw responses governed the transverse velocities of the blade root even in long waves when roll motion dominated the displacements path. This is mostly explained by the blade root being located far away from the COG in x-direction of the blade, which makes it sensitive to yaw responses. The in-line velocities had contributions from different responses, including wave frequency responses, blade roll resonance, and double pendulum induced vibrations. One can argue that these were not of significant size, but when acting all together, the motion can become notable. Nevertheless, the blade roll resonance dictated the velocities when it approached a substantial amplitude.

Both winds and waves had an significant impact on the blade responses. For long waves it was clear that waves induced large motions, and the winds were insignificant in comparison. On the other hand, when short waves and turbulent winds were simulated, both loads had consequential effects. Winds caused blade roll resonance, while waves induced blade yaw resonance. The yaw motions were the densest which indicate that the waves are the most influential. However, one can argue that the waves had significant effect due to proximity between the peak frequency of the wave and the resonance frequency of yaw, and would not be as influential if the short wave was analyzed for peak period of 4 or 6 seconds. There is some weight to this argument if the 4 seconds case would be analyzed, due to the responses of the vessel being most influential for longer wave periods. Then, there is a possibility that the winds would be the critical parameter. On the other hand, if the 6 seconds case would be examined, the vessel motions would amplify and the blade will most likely experience larger responses. In summary, the waves will be dominant for most cases environmental cases.

The operational limits suggest that the blade installation is safe to execute for short waves of limited heights. The North Sea is exposed to rough weather conditions, and one cannot expect to get many weather windows within the operational limits for the winter months. On the other hand, the weather is more gentle in the summer, making the installation more feasible during the summer months. However, historical data was investigated for a specific site in the North Sea during the summer months, which resulted in only 14.4% of the 1-hour sea-states being acceptable for the favourable heading. Hence, the installation vessel would most likely spend most of the time offshore waiting for available weather windows. Therefore,it would not

be cost-efficient to perform blade installation at this specific site with the specific vessel. On the other hand, wind and wave conditions may be more favourable at other sites in the North Sea where the waves are expected to be shorter. This should be further investigated.

In retrospect, typical wind and wave conditions at different sites in the North Sea should have been inspected before deciding on the environmental conditions being investigated. As seen in figure 4.30, there are many unacceptable cases inside the acceptable wave domain due to the magnitude of the wind speed. If higher wind speeds were considered in addition to the already considered cases, more acceptable cases could have been identified. Also, waves of greater significant wave height could have been inspected. For waves with peak periods; 5s-7s, none cases resulted inside the unacceptable domain for head sea. Consequently, taller waves could have been explored to potentially recognize a larger safe domain. Nevertheless, even though all these cases would be accepted, there would still be a great amount of time where the vessel would be waiting on weather.

Chapter 6

Conclusion and Further Work

6.1   Conclusion

The spectral analysis revealed that blade pendulum/roll- and yaw resonance governed the motions of the blade. These occur at different frequencies; 0.5 rad/s for roll and 1.2 rad/s for yaw. Yaw resonance were mainly induced by the short waves, while the winds could have great contribution towards roll resonance. Moreover, it was concluded that waves was the most critical parameter. The vessel roll- and pitch motions had significant impact on the blade motions. The natural frequencies of these motions are in the same region as the natural frequency of the blade roll motion. When waves with similar frequencies, e.g. long waves, were generated, these motions were substantially amplified. Furthermore, it was discovered that the wind may have an damping effect of the blade yaw motion, when it was approaching from 45°.

The study derived the operational limits for the blade installation by use of a monohull vessel. The probabilistic model of the underlying data was considered to be sufficient. Head sea was identified as the most favourable vessel heading. Even for the most favourable heading, low operational limits were obtained. Only 14.4% of the 1-hour sea-states investigated for site 14 in the North Sea resulted in satisfying the operational limits. Even though there was a limited amount of sea-states investigated, the study concluded that it would not be cost-efficient to conduct the installation and new methods have to be applied to utilize a monohull vessel for blade installation.

6.2   Further Work

Further studies could look into mitigations effects of the installation system. The blade yaw and roll resonance motions governed the motions of the blades, and one should look into how these can be reduced. The tugger line pre-tension can easily be increased to restrict the yaw motion of the blade. A more comprehensive study is to implement an active tension control to the tugger lines, which would have a more significant effect on the yaw motion. However, these do not contribute significantly to minimalizing the roll motion of the blade since the z-component of the tugger lines is very small. One could look at the lifting arrangement to design against blade roll motion. The lifting yoke and slings are not designed for the utilization of a floating vessel. The result is blade roll resonance motion in the same region as the roll resonance of the vessel. Therefore, another design for the lifting arrangement should be considered for floating vessels.

Installation vessels aim to reduce the motions of the vessel, and one could look at the possibilities to damp these motions. The most advanced installation vessels are equipped with high-class DP systems. These systems allow for high precision station-keeping and damping of motions in the different degrees of freedom. The DP system of the numerical model is simplified as linear springs with 70% of critical damping in surge, sway, and yaw. The numerical model could include a more comprehensive DP system, which increase the damping of the system. Furthermore, anti-roll devices such as anti-roll tanks and bilge keels may be introduced.

The thesis required a substantial amount of computational effort. Many of the simulations are unnecessary because it is inevitable for the environmental condition to satisfy the response-based criteria. For instance, if the response-based criteria for a certain peak period is not satisfied for $H_s = 1$m, it will neither be satisfied for $H_s = 2$m. One could develop an algorithm to prevent these simulations from being performed. In that way, the lesser computational effort is required to derive the operational limit, allowing more time to analyze different environmental cases.

Bibliography

[1] I. E. Agency. *World Energy Outlook 2020*. 2020. DOI: `https://doi.org/ https://doi.org/10.1787/557a761b-en`. URL: `https://www.oecd-ilibrary.org/content/publication/557a761b-en`.

[2] *DNV GL Energy Transition Outlook Executive Summary*. DNV GL, 2020.

[3] *Offshore Wind in Europe - Key trends and statistics 2019*. Feb. 2020. URL: `https://windeurope.org/wp-content/uploads/files/about-wind/statistics/WindEurope-Annual-Offshore-Statistics-2019.pdf`.

[4] *World Energy Investment 2020*. 2020. URL: `https://www.iea.org/reports/world-energy-investment-2020/key-findings#abstract`. Accessed: 13. October 2020.

[5] *Colossal Six Months for Offshore Wind Support Renewable Energy Investment in First Half of 2020*. July 2020. URL: `https://about.bnef.com/blog/colossal-six-months-for-offshore-wind-support-renewable-energy-investment-in-first-half-of-2020/`.

[6] "Floating Offshore Wind Energy - A Policy Bluefrint for Europe". In: (2018). URL: `https://windeurope.org/wp-content/uploads/files/policy/position-papers/Floating-offshore-wind-energy-a-policy-blueprint-for-Europe.pdf`.

[7] T. Stehly and P. Beiter. "2018 Cost of Wind Energy Review". In: (2020). URL: `https://www.nrel.gov/docs/fy20osti/74598.pdf`.

[8] J. Jonkman, S. Butterfield, W. Musial, and G. Scott. "Definition of a 5-MW Reference Wind Turbine for Offshore System Development". In: (Feb. 2009). DOI: `10.2172/947422`.

[9] e. a. Christian Bak. "Description of the DTU 10 MW Reference Wind Turbine". In: (July 2013).

[10] E. Gaertner, J. Rinker, L. Sethuraman, F. Zahle, B. Anderson, G. Barter, N. Abbas, F. Meng, P. Bortolotti, W. Skrzypinski, G. Scott, R. Feil, H. Bredmose, K. Dykes, M. Shields, C. Allen, and A. Viselli. "Definition of the IEA Wind 15-Megawatt Offshore Reference Wind Turbine". In: (Mar. 2020).

[11] *Offshore Wind Turbines Foundation Types*. URL: `http://www.windfarmbop.com/offshore-wind-turbines-foundation-types/`. Accessed: 14. October 2020.

[12] *Pacific Osprey*. URL: `https://www.offshorewind.biz/vessels/pacific-osprey/`. Accessed: 29. November 2020.

[13] *Pacific Osprey*. URL: `http://www.shipspotting.com/gallery/photo.php?lid=2706682`. Accessed: 29. November 2020.

[14] *Ulstein J103 vessel design*. URL: `https://ulstein.com/vessel-design/j103`. Accessed: 29. November 2020.

[15] *Aegir*. URL: `https://hmc.heerema.com/fleet/aegir/`. Accessed: 4. December 2020.

[16] "Heerema's DP3 Vessel Aegir Installs First Offshore Wind Turbine". In: (Sept. 2018). URL: `https://hmc.heerema.com/news-media/news/heeremas-dp3-vessel-aegir-installs-first-offshore-wind-turbine/`.

[17] *Aegir*. URL: `https://ulstein.com/references/aegir`. Accessed: 4. December 2020.

[18] *Balder*. URL: `https://hmc.heerema.com/fleet/balder/`. Accessed: 4. December 2020.

[19] Y. Zhao. "Numerical Modeling and Dynamic Analysis of Offshore Wind Turbine Blade Installation". PhD thesis. Trondheim, NO, Nov. 2019.

[20] Y. Zhao. "Assessment of marine operations for offshore wind turbine installation with emphasis on response-based operational limits". PhD thesis. Trondheim, NO, Dec. 2016.

[21] A. S. Verma. "Modelling, Analysis and Response-based Operability Assessment of Offshore Wind Turbine Blade Installation with Emphasis on Impact Damages". PhD thesis. Trondheim, NO, June 2019.

[22] *Marine Operations, General*. Oct. 2011. URL: `https://rules.dnvgl.com/docs/pdf/DNV/codes/docs/2011-10/Os-H101.pdf`.

[23] M. Johannessen. "Concept Study and Design of Floating Offshore Wind Turbine Support Structure". In: (2018).

[24] *DESIGN AND MANUFACTURE OF WIND TURBINE BLADES, OFFSHORE AND ONSHORE WIND TURBINES*. 2010. URL: `https://rules.dnvgl.com/docs/pdf/DNV/codes/docs/2010-11/DS-J102.pdf`.

[25] B. Jonkman and J. M.L. Buhl. *TurbSim User Guide*. NREL, Sept. 2006.

[26] S. P. Team. *SIMO 4.10.3 User Guide*. SINTEF Ocean, 2017.

Appendices

Appendix A

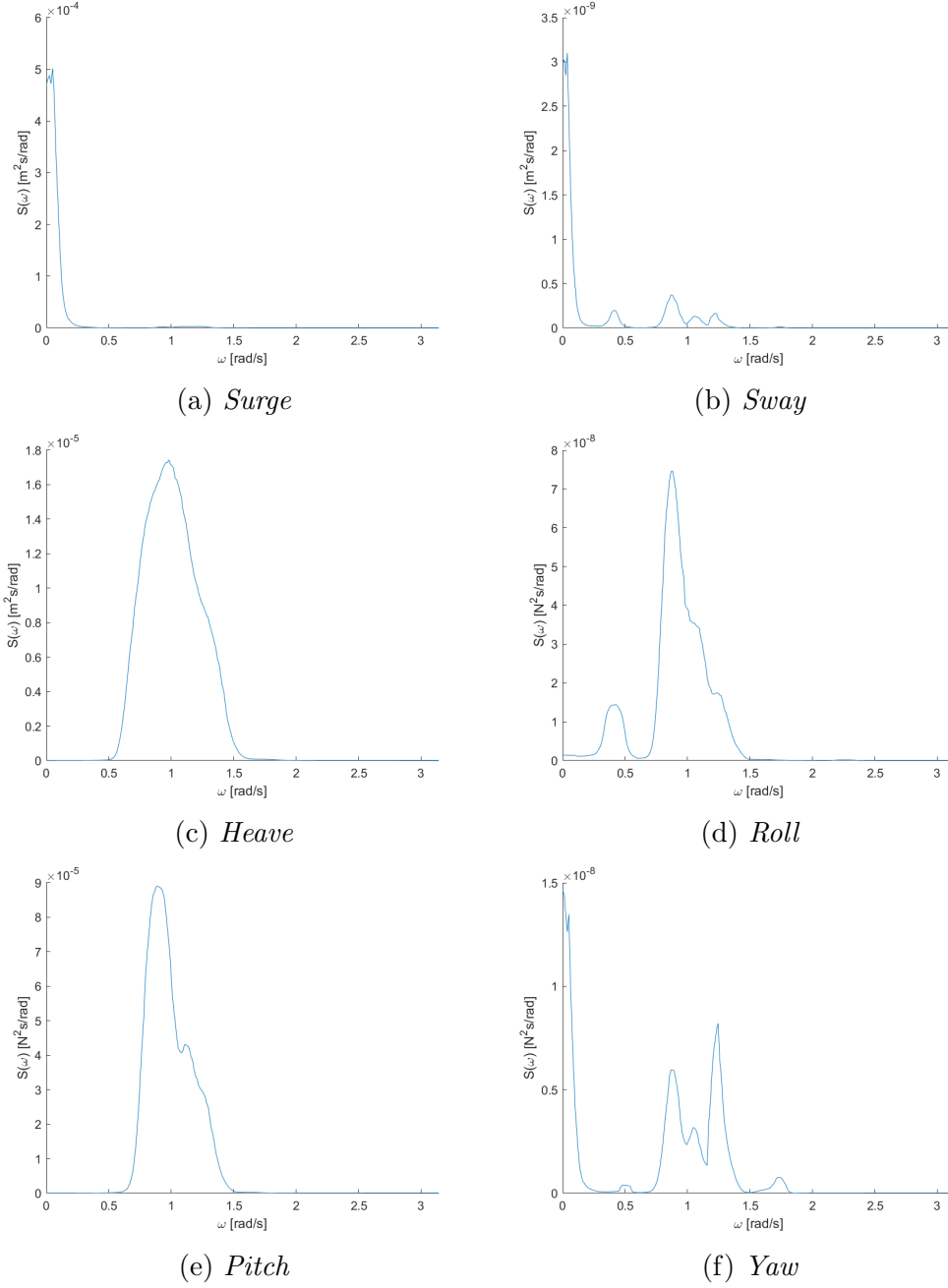# Spectral Analysis

A.1 Head Sea

(a) *Surge*

(b) *Sway*

(c) *Heave*

(d) *Roll*

(e) *Pitch*

(f) *Yaw*

Figure A.1: *Response spectra for vessel in short waves (H_s = 1m, T_p = 5s, θ = 0°, U_{ref} = 10m/s, TI = 12%)*

(a) *Surge*

(b) *Sway*

(c) *Heave*

(d) *Roll*

(e) *Pitch*

(f) *Yaw*
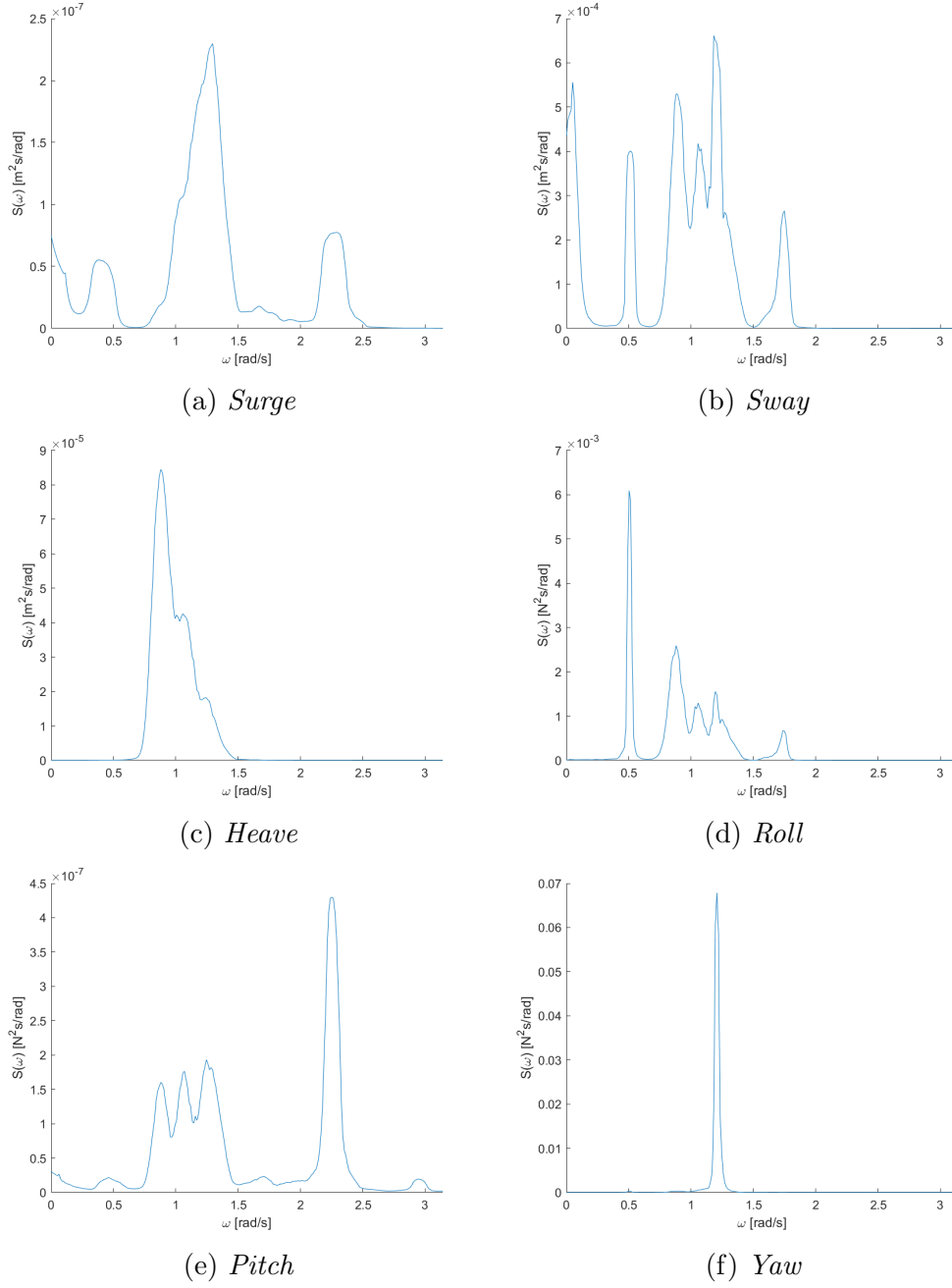
Figure A.2: *Response spectra for blade in short waves ($H_s = 1m$, $T_p = 5s$, $\theta = 0°$, $U_{ref} = 10m/s$, $TI = 12\%$)*
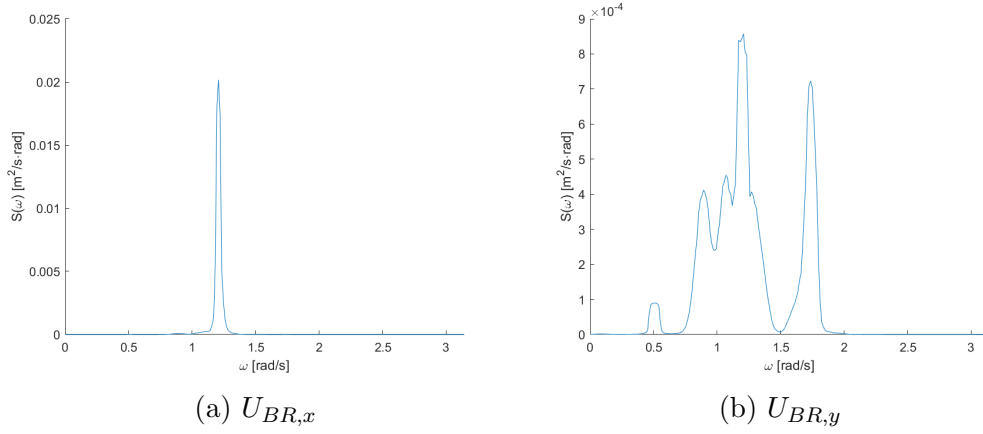
(a) $U_{BR,x}$

(b) $U_{BR,y}$

Figure A.3: *Response spectra for blade root in short waves ($H_s = 1m$, $T_p = 5s$, $\theta = 0°$, $U_{ref} = 10m/s$, $TI = 12\%$)*
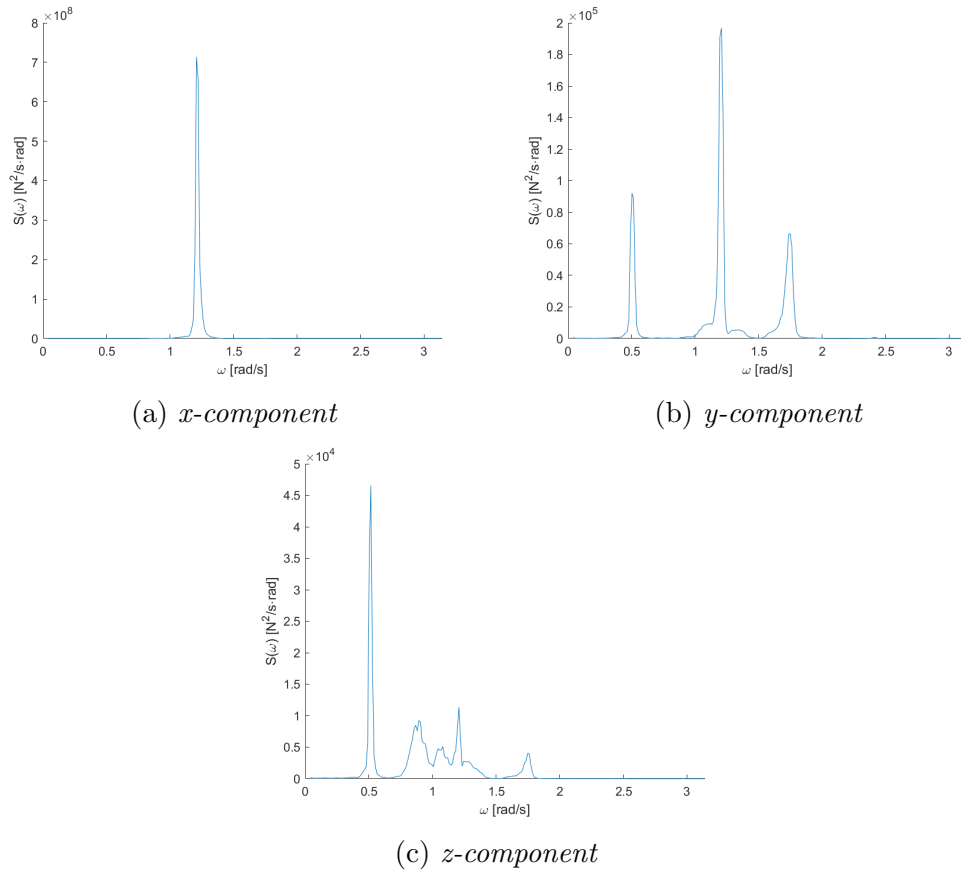

(a) *x-component*

(b) *y-component*

(c) *z-component*

Figure A.4: *Force response spectra for tugger line in short waves ($H_s = 1m$, $T_p = 5s$, $\theta = 0°$, $U_{ref} = 10m/s$, $TI = 12\%$)*

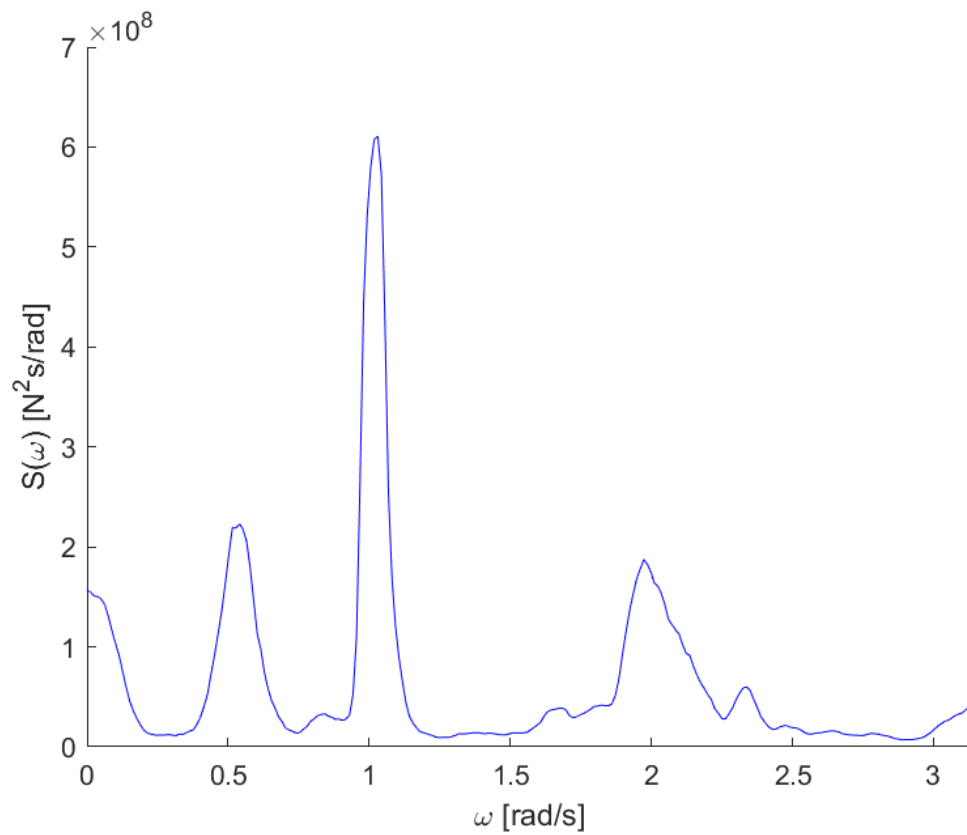Figure A.5: *Force spectra for lift wire in short waves (H_s = 1m, T_p = 5s, θ = 0°, U_{ref} = 10m/s, TI = 12%)*

(a) *Surge*

(b) *Sway*

(c) *Heave*

(d) *Roll*

(e) *Pitch*

(f) *Yaw*
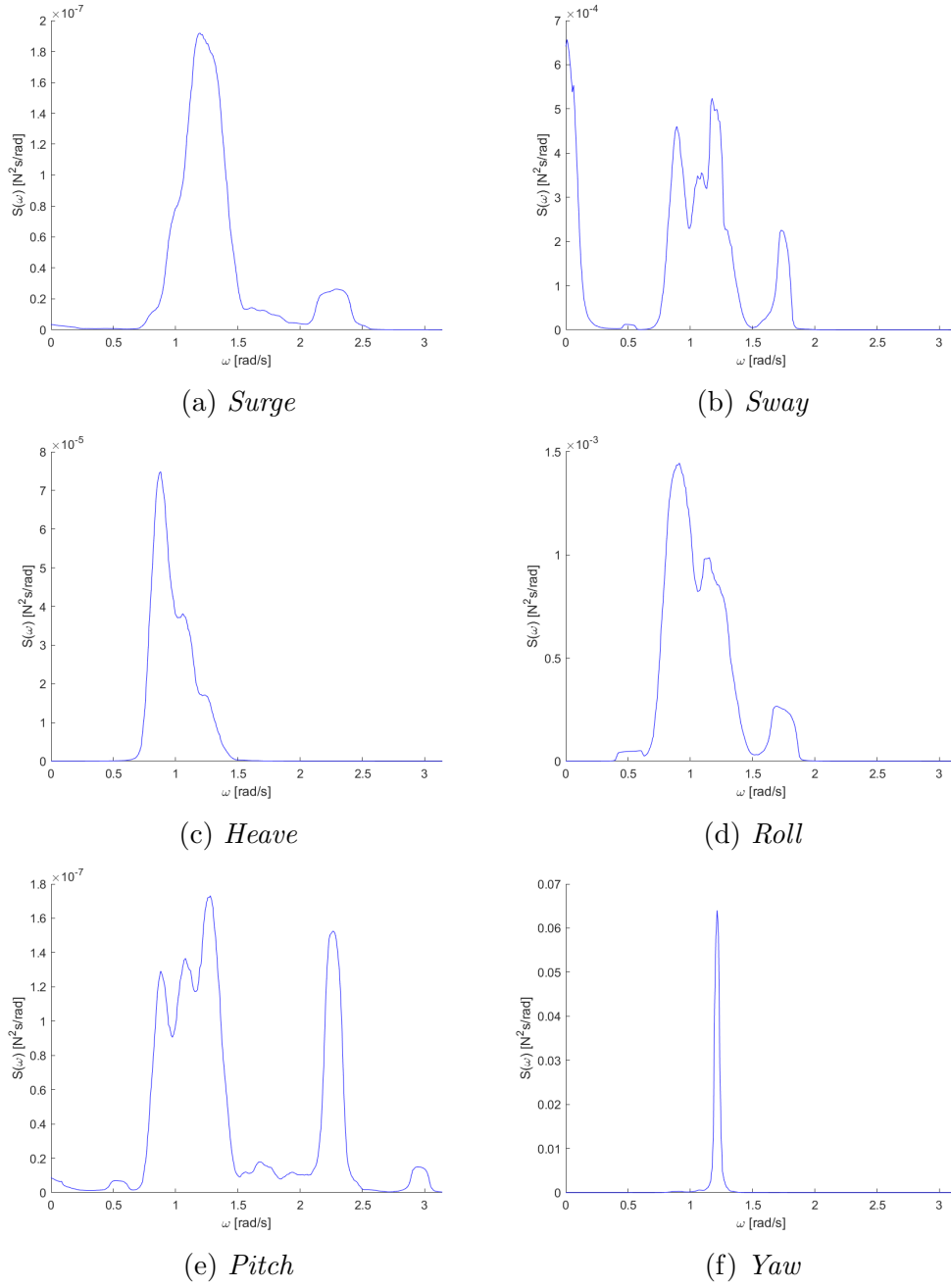
Figure A.6: *Response spectra for blade in short waves ($H_s = 1m$, $T_p = 5s$, $\theta = 0°$, $U_{ref} = 0m/s$, $TI = N/A$)*

A.2   Long Wave

(a) *Surge*

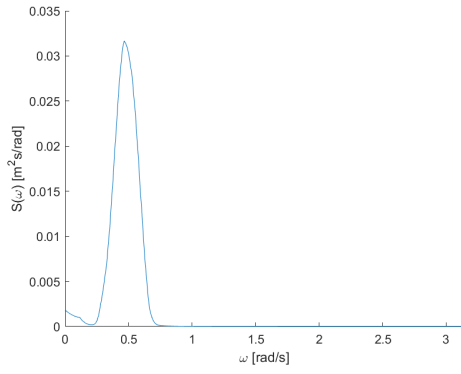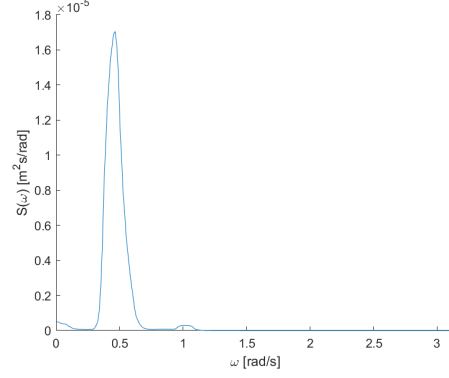(b) *Sway*

(c) *Heave*

(d) *Roll*

(e) *Pitch*

(f) *Yaw*

Figure A.7: *Response spectra for vessel in long waves ($H_s = 1m$, $T_p = 12s$, $\theta = 0°$, $U_{ref} = 10m/s$, TI = 12%)*
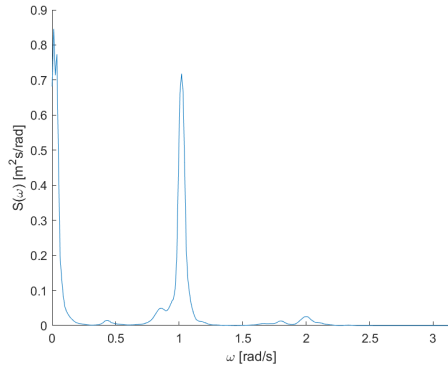
(a) *Surge*
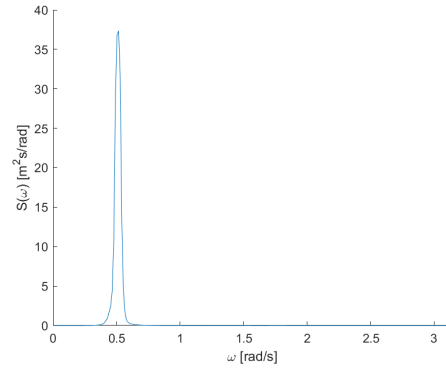
(b) *Sway*

(c) *Heave*
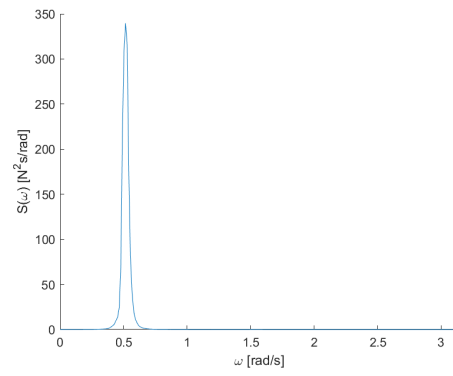
(d) *Roll*
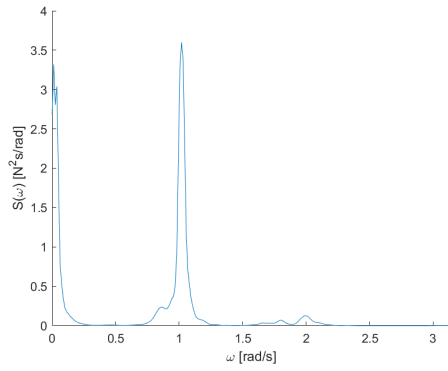
(e) *Pitch*
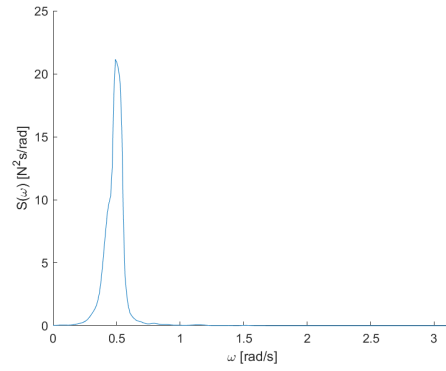
(f) *Yaw*

Figure A.8: *Response spectra for blade in long waves ($H_s = 1m$, $T_p = 12s$, $\theta = 0°$, $U_{ref} = 10m/s$, $TI = 12\%$)*

(a) $U_{BR,x}$ (b) $U_{BR,y}$
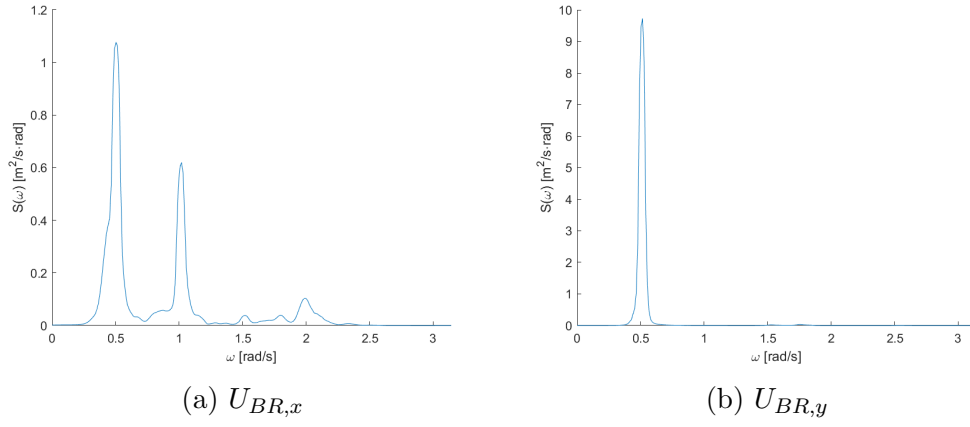
Figure A.9: *Response spectra for blade root in long waves ($H_s = 1m$, $T_p = 12s$, $\theta = 0°$, $U_{ref} = 10m/s$, $TI = 12\%$)*
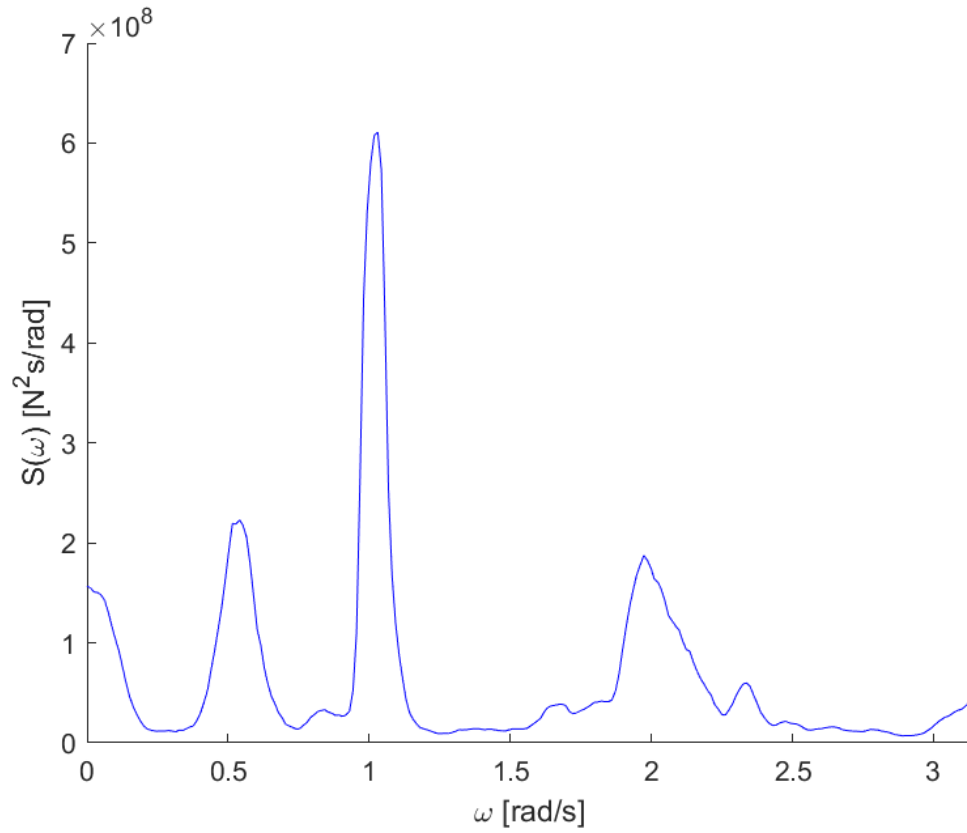
Figure A.10: *Force spectra for lift wire tension in long waves ($H_s = 1m$, $T_p = 12s$, $\theta = 0°$, $U_{ref} = 10m/s$, $TI = 12\%$)*
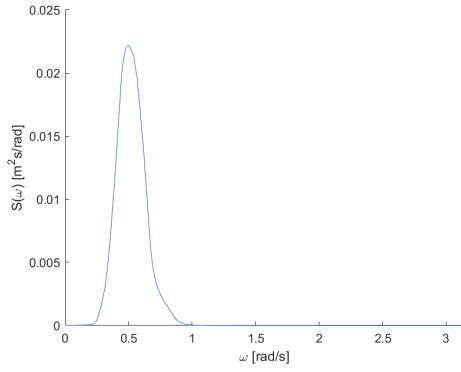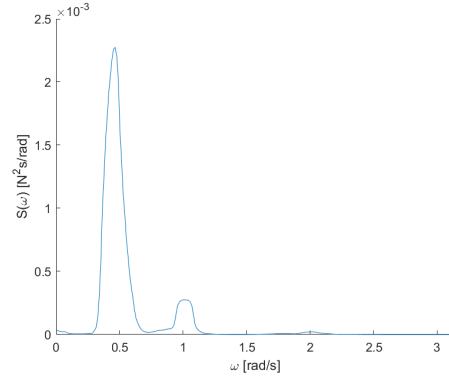
A.3   Bow Sea

(a) *Surge*

(b) *Sway*

(c) *Heave*

(d) *Roll*

(e) *Pitch*

(f) *Yaw*
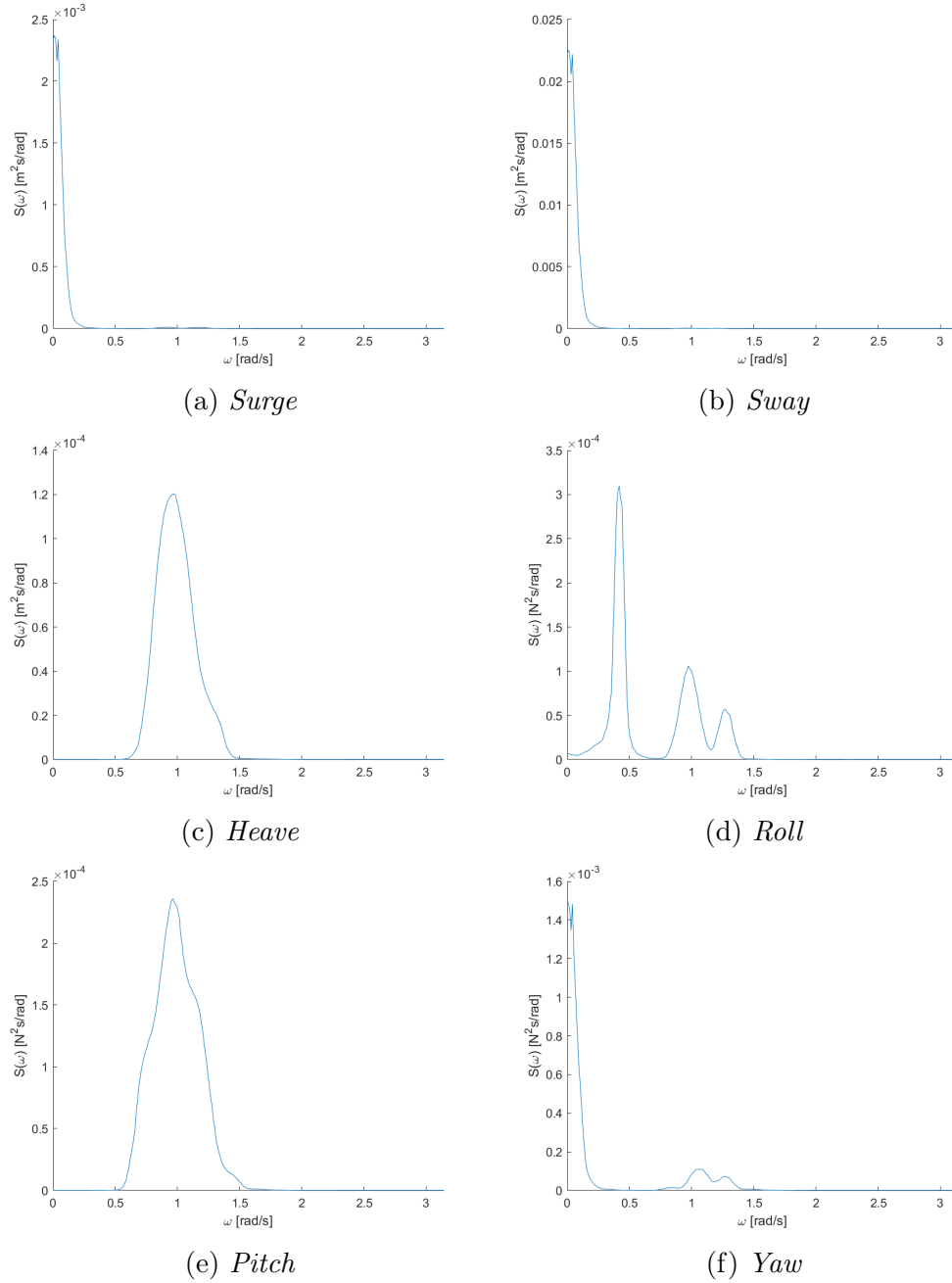
Figure A.11: *Response spectra for vessel in short waves ($H_s = 1m$, $T_p = 5s$, $\theta = 45°$, $U_{ref} = 10m/s$, $TI = 12\%$)*
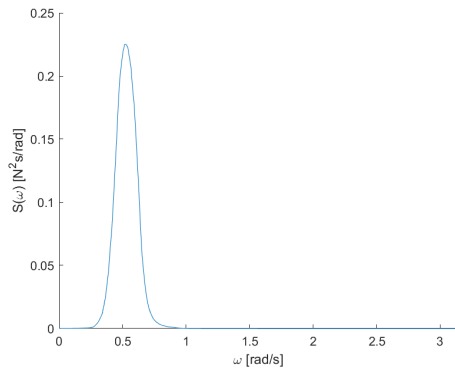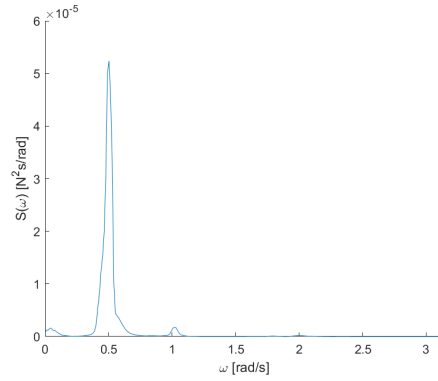
(a) *Surge*

(b) *Sway*

(c) *Heave*
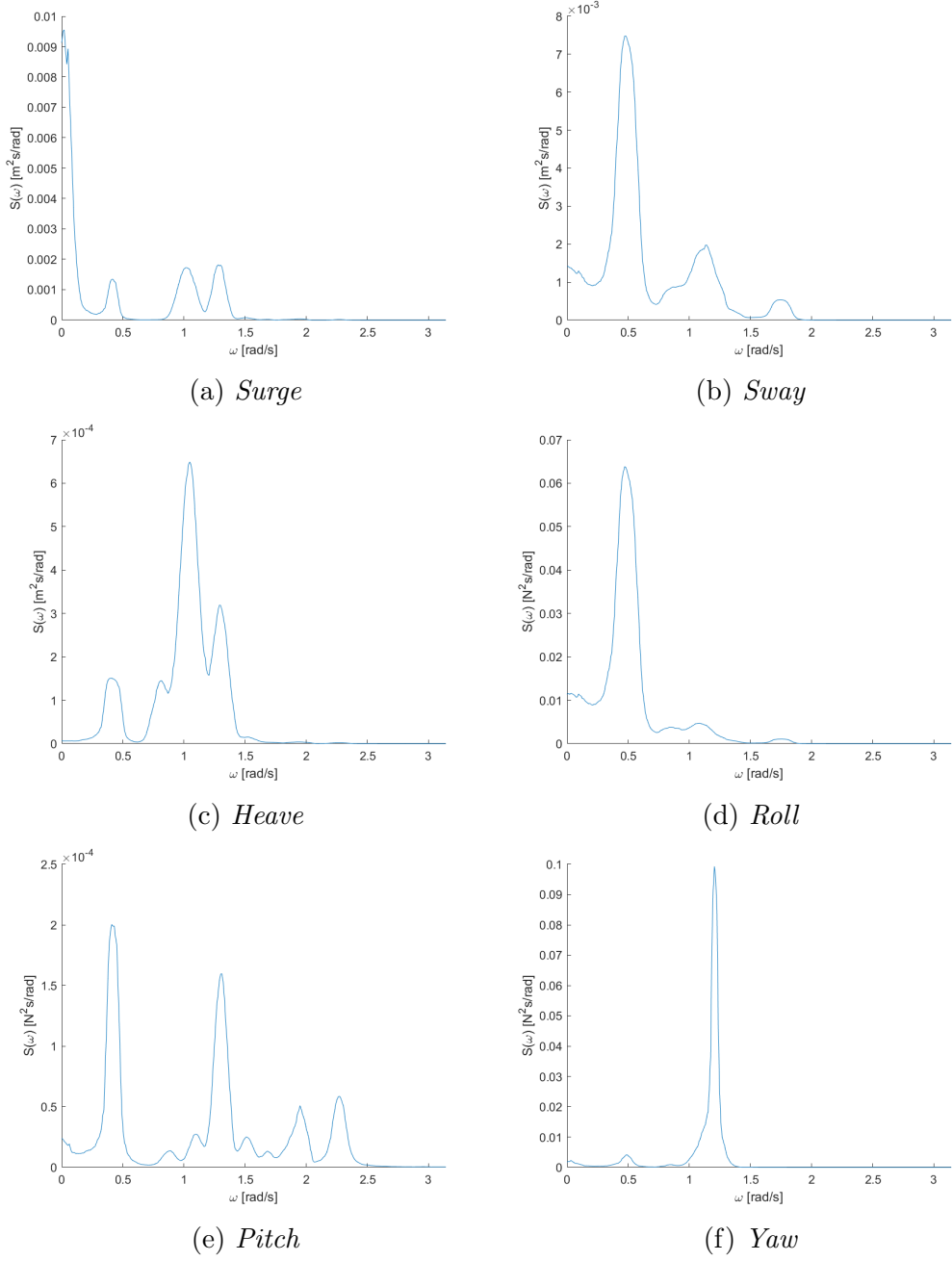
(d) *Roll*

(e) *Pitch*

(f) *Yaw*

Figure A.12: *Response spectra for blade in short waves ($H_s = 1m$, $T_p = 5s$, $\theta = 45°$, $U_{ref} = 10m/s$, $TI = 12\%$)*

(a) $U_{BR,x}$

(b) $U_{BR,y}$
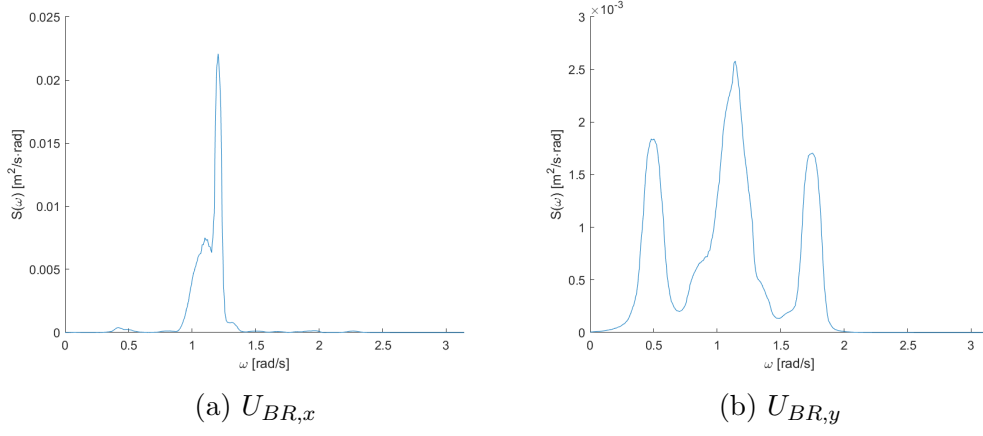
Figure A.13: *Velocity spectra for blade root in short waves (H_s = 1m, T_p = 5s, θ = 45°, U_{ref} = 10m/s, TI = 12%)*
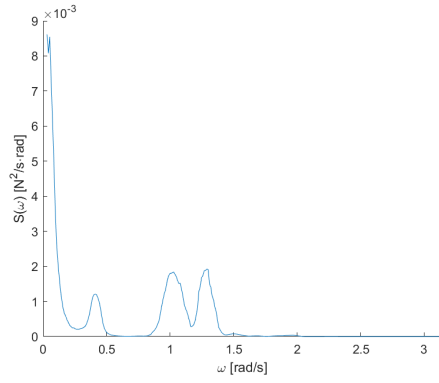
(a) *Surge*
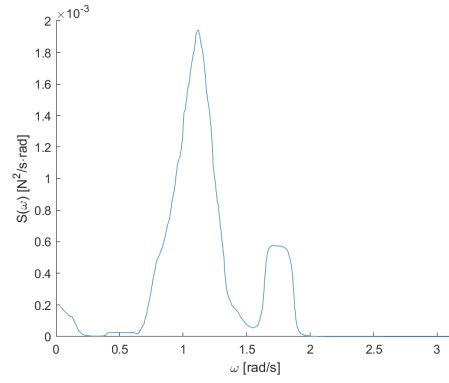
(b) *Sway*
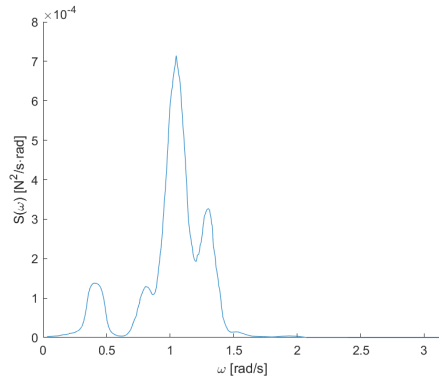
(c) *Heave*
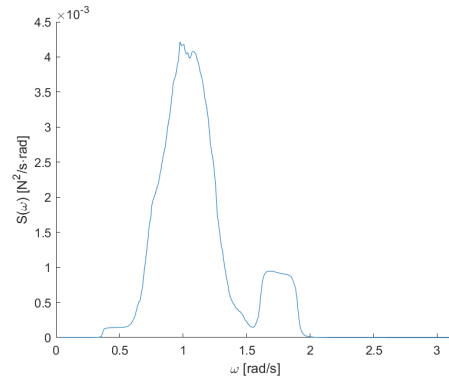
(d) *Roll*
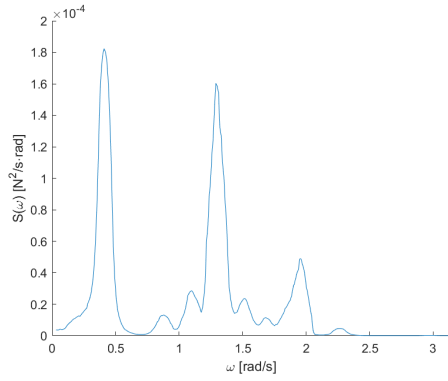
(e) *Pitch*
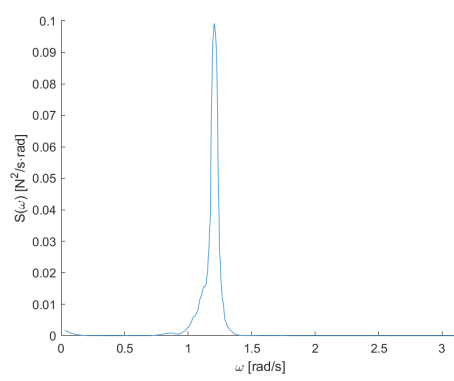
(f) *Yaw*

Figure A.14: *Response spectra for blade in short waves ($H_s = 1m$, $T_p = 5s$, $\theta = 45°$, $U_{ref} = 0m/s$, $TI = N/A\%$)*

(a) *Surge*

(b) *Sway*
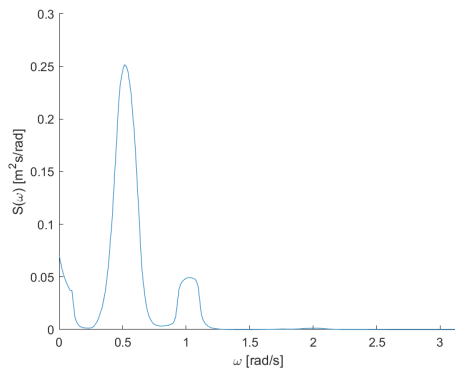
(c) *Heave*
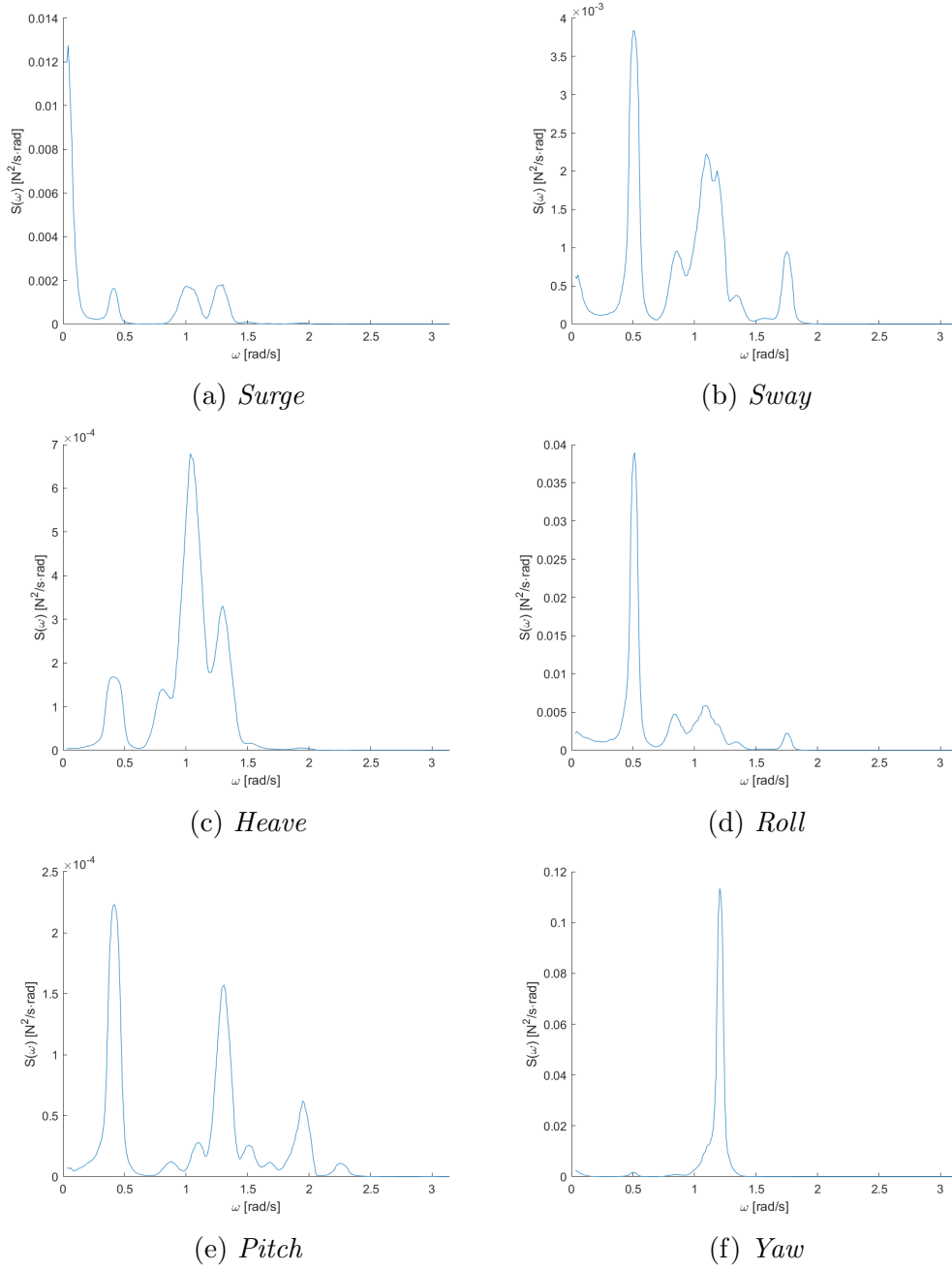
(d) *Roll*

(e) *Pitch*

(f) *Yaw*

Figure A.15: *Response spectra for blade in short waves (H_s = 1m, T_p = 5s, θ = 45°, U_{ref} = 5m/s, TI = 12%)*

A.4   Turbulent Wind


(a) *Surge*

(b) *Sway*

(c) *Heave*
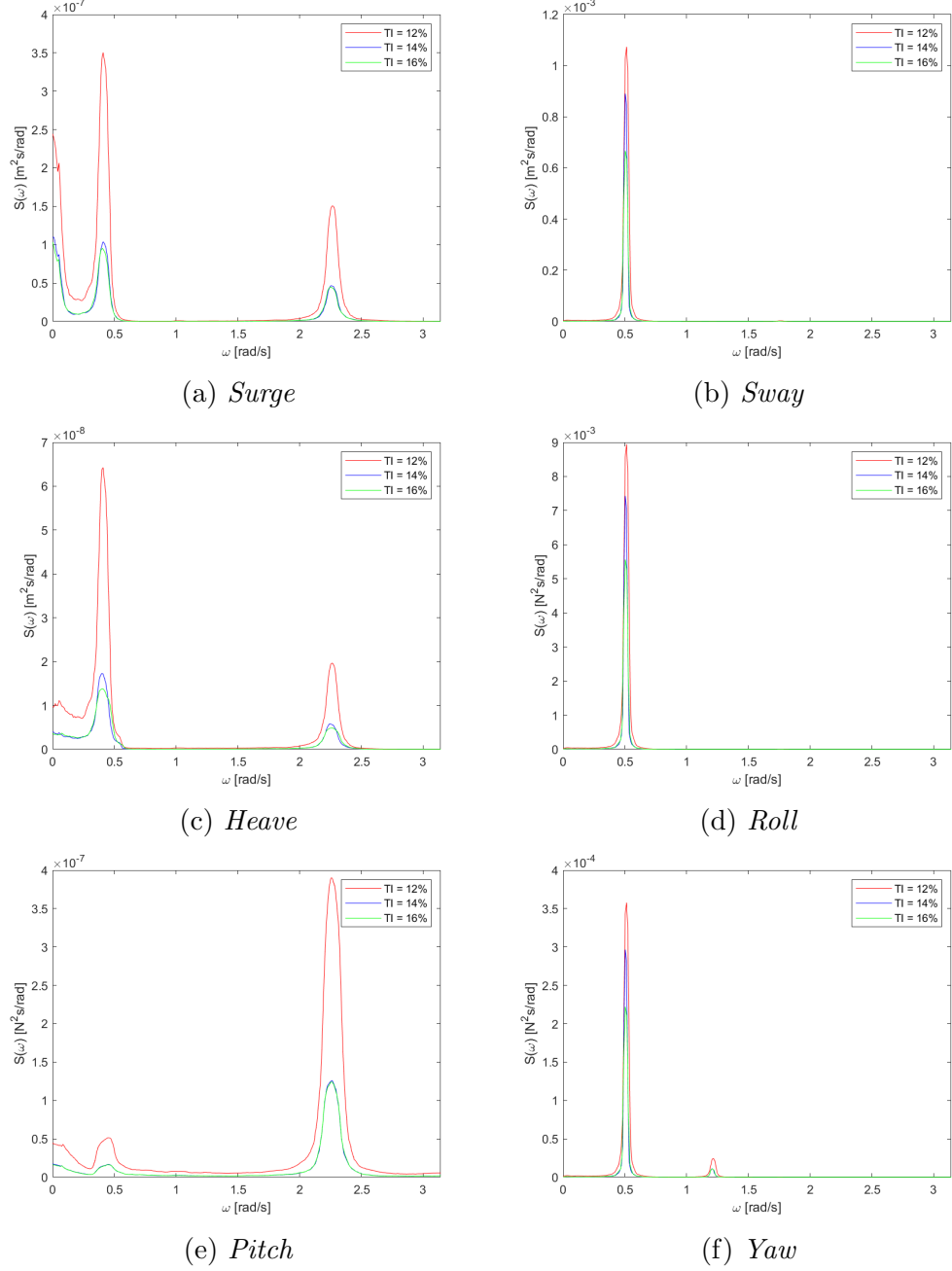
(d) *Roll*

(e) *Pitch*

(f) *Yaw*

Figure A.16: *Response spectra for blade in turbulent wind ($H_s = 0m$, $T_p = 0s$, $\theta = 0°$, $U_{ref} = 10m/s$, TI = 12%/14%/16%)*
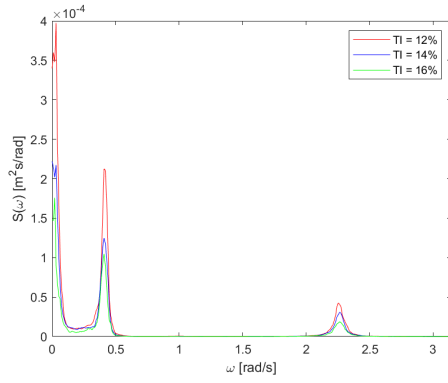
(a) *Surge*
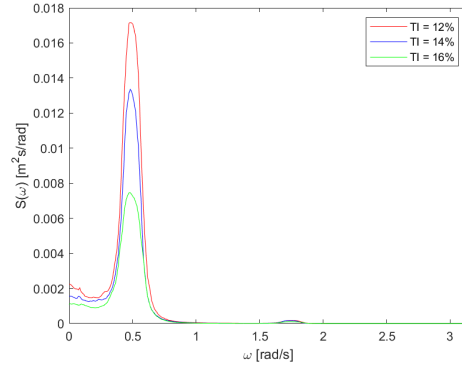
(b) *Sway*
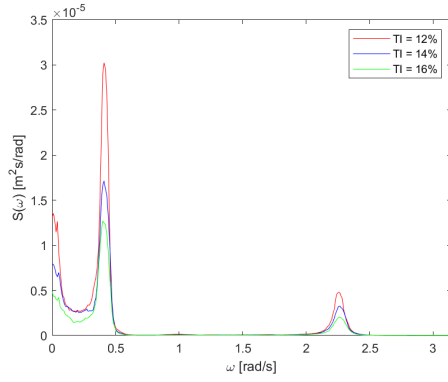
(c) *Heave*
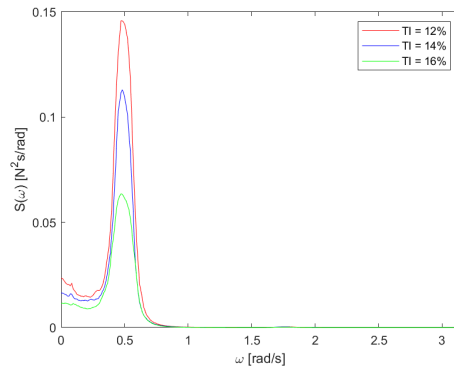
(d) *Roll*
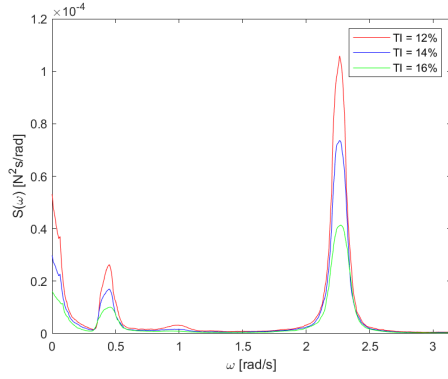
(e) *Pitch*
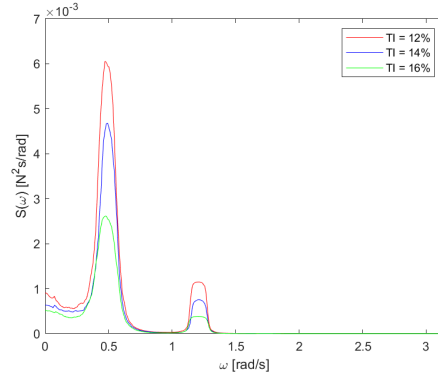
(f) *Yaw*

Figure A.17: *Response spectra for blade in turbulent wind ($H_s = 0m$, $T_p = 0s$, $\theta = 45°$, $U_{ref} = 10m/s$, $TI = 12\%/14\%/16\%$)*

Appendix **B**

Operational Limits Results

B.1 Response-Based Criteria

The following tables show whether or not the response-based criteria are accepted for each sea-state for the individual environmental case. Each cell represents a given sea state where the row defines H_s, and the column describes T_p. Green values mean that both criteria are accepted, yellow indicates that only the criterion listed in that specific cell is accepted, and red illustrates the unacceptable conditions.

Table B.1: *Response-based criteria for $U_{ref} = 10m/s$ and $\theta = 0°$*

H_s [m] \ T_p[s]	5	6	7	8	9	10	11	12	13	14
2.0	Y	Y	Y	N	N	N	N	N	N	N
1.5	Y	Y	Y	Y	N	N	N	N	N	N
1.0	Y	Y	Y	Y	N	N	N	N	N	N
0.5	Y	Y	Y	Y	Y	N	N	N	N	N

Table B.2: *Response-based criteria for $U_{ref} = 5m/s$ and $\theta = 0°$*

H_s [m] \ T_p[s]	5	6	7	8	9	10	11	12	13	14
2.0	Y	Y	Y	N	N	N	N	N	N	N
1.5	Y	Y	Y	Y	N	N	N	N	N	N
1.0	Y	Y	Y	Y	N	N	N	N	N	N
0.5	Y	Y	Y	Y	Y	N	N	N	N	N

Table B.3: *Response-based criteria for for $U_{ref} = 5m/s$ and $\theta = 45°$*

H_s [m] \ T_p[s]	5	6	7	8	9	10	11	12	13	14
2.0	$U_{BR,y}$	$U_{BR,y}$	N	N	N	N	N	N	N	N
1.5	Y	Y	Y	N	N	N	N	N	N	N
1.0	Y	Y	Y	$U_{BR,y}$	N	N	N	N	N	N
0.5	Y	Y	Y	Y	Y	$U_{BR,y}$	N	N	N	N

Table B.4: *Response-based criteria for $U_{ref} = 10m/s$ and $\theta = 45°$*

H_s [m] \ $T_p[s]$	5	6	7	8	9	10	11	12	13	14
2.0	$U_{BR,y}$	$U_{BR,y}$	$U_{BR,y}$	N	N	N	N	N	N	N
1.5	Y	Y	Y	N	N	N	N	N	N	N
1.0	Y	Y	Y	$U_{BR,y}$	$U_{BR,y}$	$U_{BR,y}$	N	N	N	N
0.5	Y	Y	Y	Y	Y	$U_{BR,y}$	$U_{BR,y}$	$U_{BR,y}$	N	$U_{BR,y}$

B.2   In-line and Transverse Velocities of Blade Root

The following tables present the 99.99-percentile velocities for the blade's in-line and transverse velocities for each environmental case. Each cell represents a given sea state where the row defines H_s, and the column describes T_p. The units of each cell are m/s.

Table B.5: $U_{BR,x}$ for $U_{ref} = 5m/s$ and $\theta = 0°$

H_s [m] \ T_p [s]	5	6	7	8	9	10	11	12	13	14
2.0	0.34	0.34	0.37	0.99	3.94	12.87	18.83	19.99	22.35	17.58
1.5	0.29	0.27	0.32	0.75	3.95	5.88	16.19	20.52	20.36	21.26
1.0	0.16	0.15	0.19	0.54	1.46	3.61	11.41	10.42	16.06	6.87
0.5	0.10	0.07	0.09	0.21	0.65	1.38	2.33	3.34	3.94	2.80

Table B.6: $U_{BR,y}$ for $U_{ref} = 5m/s$ and $\theta = 0°$

H_s [m] \ T_p [s]	5	6	7	8	9	10	11	12	13	14
2.0	0.25	0.42	0.80	1.68	3.35	4.09	9.51	7.55	6.73	5.18
1.5	0.18	0.33	0.46	1.24	3.12	3.65	6.68	7.63	6.33	5.25
1.0	0.13	0.19	0.36	0.92	1.96	2.97	4.02	4.01	4.98	4.68
0.5	0.06	0.11	0.19	0.40	0.96	1.85	2.49	2.84	3.44	2.86

Table B.7: $U_{BR,x}$ for $U_{ref} = 10m/s$ and $\theta = 0°$

H_s [m] \ T_p [s]	5	6	7	8	9	10	11	12	13	14
2.0	0.37	0.30	0.41	0.97	3.34	12.38	20.77	18.61	22.96	22.13
1.5	0.30	0.24	0.32	0.66	3.44	5.28	14.67	16.39	18.78	18.14
1.0	0.17	0.12	0.18	0.48	1.66	2.66	5.81	14.22	13.85	4.59
0.5	0.11	0.07	0.09	0.25	0.53	1.35	2.21	3.59	2.92	2.17

Table B.8: $U_{BR,y}$ for $U_{ref} = 10m/s$ and $\theta = 0°$

H_s [m] \ $T_p[s]$	5	6	7	8	9	10	11	12	13	14
2.0	0.26	0.37	0.82	1.45	3.07	5.23	6.94	8.92	7.73	7.02
1.5	0.17	0.29	0.45	1.11	3.02	3.62	6.21	7.28	4.52	5.82
1.0	0.14	0.24	0.39	0.77	1.78	2.71	3.58	6.10	5.29	3.54
0.5	0.07	0.11	0.17	0.44	0.90	1.74	2.30	3.27	2.58	2.74

Table B.9: $U_{BR,x}$ for $U_{ref} = 5m/s$ and $\theta = 45°$

H_s [m] \ $T_p[s]$	5	6	7	8	9	10	11	12	13	14
2.0	1.10	0.85	0.99	2.04	7.30	13.06	21.99	29.58	28.56	29.20
1.5	0.58	0.59	0.64	1.23	3.73	8.23	19.24	18.03	22.45	18.26
1.0	0.40	0.43	0.55	0.92	1.66	2.33	4.43	7.86	6.54	8.53
0.5	0.19	0.16	0.25	0.43	0.72	1.10	1.78	1.97	2.17	2.94

Table B.10: $U_{BR,y}$ for $U_{ref} = 5m/s$ and $\theta = 45°$

H_s [m] \ $T_p[s]$	5	6	7	8	9	10	11	12	13	14
2.0	0.46	0.74	1.42	1.93	2.71	6.83	8.91	9.67	10.19	8.14
1.5	0.34	0.59	0.92	1.42	2.28	3.47	7.16	8.46	6.87	6.13
1.0	0.23	0.42	0.59	0.97	1.48	1.68	2.37	3.87	3.56	3.86
0.5	0.14	0.20	0.31	0.43	0.57	0.90	1.42	1.64	2.22	1.57

Table B.11: $U_{BR,x}$ for $U_{ref} = 10m/s$ and $\theta = 45°$

H_s [m] \ $T_p[s]$	5	6	7	8	9	10	11	12	13	14
2.0	0.99	0.90	1.10	1.46	7.98	9.22	16.69	17.28	30.18	35.24
1.5	0.73	0.67	0.64	1.36	2.58	2.86	9.02	11.62	21.10	23.21
1.0	0.41	0.47	0.45	0.91	1.29	1.94	3.30	3.99	6.15	6.19
0.5	0.20	0.21	0.27	0.50	0.68	0.93	1.16	1.90	2.29	3.03

Table B.12: $U_{BR,y}$ for $U_{ref} = 10m/s$ and $\theta = 45°$

H_s [m] \ $T_p[s]$	5	6	7	8	9	10	11	12	13	14
2.0	0.41	0.74	1.32	1.88	3.29	5.66	6.83	7.27	7.13	8.11
1.5	0.36	0.54	0.89	1.57	1.79	2.07	3.83	4.30	5.53	6.67
1.0	0.26	0.53	0.66	1.10	1.31	1.32	1.45	2.23	2.88	2.40
0.5	0.19	0.22	0.32	0.54	0.62	0.55	0.72	0.98	1.43	1.09

B.3 r^2-values

The rest of the tables present the r^2-value of the fitted distribution function of the given velocity component of the blade root for each environmental case. Each cell represents a given sea state where the row defines H_s, and the column describes T_p. The units of each cell are dimensionless.

Table B.13: r^2 for $U_{BR,x}$ for $U_{ref} = 5m/s$ and $\theta = 0°$

H_s [m] \ T_p[s]	5	6	7	8	9	10	11	12	13	14
2.0	0.93	0.98	0.89	0.96	0.94	0.89	0.67	0.71	0.89	0.73
1.5	0.98	0.98	0.97	0.95	0.90	0.98	0.84	0.73	0.83	0.90
1.0	0.93	0.91	0.94	0.96	0.95	0.98	0.74	0.85	0.79	0.94
0.5	0.96	0.88	0.97	0.94	0.90	0.97	0.95	0.97	0.96	0.89

Table B.14: r^2 for $U_{BR,y}$ for $U_{ref} = 5m/s$ and $\theta = 0°$

H_s [m] \ T_p[s]	5	6	7	8	9	10	11	12	13	14
2.0	0.96	0.97	0.94	0.98	0.90	0.96	0.97	0.89	0.95	0.95
1.5	0.96	0.97	0.96	0.98	0.97	0.98	0.86	0.98	0.90	0.93
1.0	0.96	0.93	0.97	0.98	0.94	0.99	0.95	0.89	0.98	0.99
0.5	0.97	0.98	0.99	0.88	0.88	0.99	0.92	0.94	0.92	0.98

Table B.15: r^2 for $U_{BR,x}$ for $U_{ref} = 10m/s$ and $\theta = 0°$

H_s [m] \ T_p[s]	5	6	7	8	9	10	11	12	13	14
2.0	0.97	0.98	0.96	0.98	0.97	0.90	0.87	0.89	0.77	0.89
1.5	0.90	0.99	0.95	0.98	0.96	0.97	0.88	0.75	0.83	0.89
1.0	0.85	0.96	0.98	0.92	0.96	0.95	0.95	0.91	0.86	0.97
0.5	0.96	0.96	0.99	0.97	0.97	0.96	0.97	0.96	0.97	0.98

Table B.16: r^2 for $U_{BR,y}$ for $U_{ref} = 10m/s$ and $\theta = 0°$

H_s [m] \ $T_p[s]$	5	6	7	8	9	10	11	12	13	14
2.0	0.98	0.96	0.95	0.94	0.99	0.96	0.95	0.95	0.96	0.93
1.5	0.92	0.98	0.96	0.91	0.98	0.97	0.92	0.98	0.96	0.97
1.0	0.89	0.98	0.95	0.96	0.94	0.96	0.94	0.94	0.97	0.94
0.5	0.95	0.96	0.71	0.97	0.96	0.95	0.97	0.98	0.97	0.96

Table B.17: r^2 for $U_{BR,x}$ for $U_{ref} = 5m/s$ and $\theta = 45°$

H_s [m] \ $T_p[s]$	5	6	7	8	9	10	11	12	13	14
2.0	0.95	0.96	0.97	0.97	0.79	0.98	0.97	0.89	0.94	0.94
1.5	0.92	0.96	0.97	0.98	0.85	0.70	0.91	0.88	0.98	0.93
1.0	0.93	0.98	0.96	0.97	0.96	0.91	0.98	0.77	0.95	0.94
0.5	0.96	0.93	0.98	0.93	0.96	0.99	0.91	0.95	0.98	0.93

Table B.18: r^2 for $U_{BR,y}$ for $U_{ref} = 5m/s$ and $\theta = 45°$

H_s [m] \ $T_p[s]$	5	6	7	8	9	10	11	12	13	14
2.0	0.95	0.96	0.97	0.96	0.96	0.95	0.98	0.96	0.96	0.95
1.5	0.98	0.86	0.94	0.91	0.95	0.86	0.84	0.97	0.93	0.97
1.0	0.93	0.97	0.99	0.96	0.99	0.96	0.94	0.97	0.96	0.97
0.5	0.98	0.90	0.94	0.98	0.96	0.97	0.97	0.98	0.96	0.97

Table B.19: r^2 for $U_{BR,x}$ for $U_{ref} = 10m/s$ and $\theta = 45°$

H_s [m] \ $T_p[s]$	5	6	7	8	9	10	11	12	13	14
2.0	0.96	0.96	0.95	0.96	0.81	0.88	0.97	0.97	0.94	0.97
1.5	0.96	0.96	0.97	0.95	0.94	0.96	0.90	0.89	0.96	0.97
1.0	0.92	0.99	0.96	0.95	0.96	0.97	0.94	0.97	0.98	0.93
0.5	0.96	0.99	0.97	0.89	0.94	0.95	0.97	0.90	0.89	0.98

Table B.20: r^2 for $U_{BR,y}$ for $U_{ref} = 10m/s$ and $\theta = 45°$

H_s [m] \ $T_p[s]$	5	6	7	8	9	10	11	12	13	14
2.0	0.95	0.89	0.96	0.96	0.93	0.62	0.89	0.98	0.97	0.98
1.5	0.91	0.93	0.95	0.98	0.95	0.90	0.83	0.95	0.98	0.96
1.0	0.96	0.96	0.96	0.99	0.97	0.96	0.97	0.97	0.95	0.99
0.5	0.93	0.97	0.91	0.93	0.90	0.98	0.96	0.88	0.96	0.93